pH in the *trans*-Golgi network/early endosome of *Arabidopsis thaliana*: Suppliers and consumers

Dissertation

zur Erlangung der Doktorwürde

der Naturwissenschaftlich-Mathematischen Gesamtfakultät

der Ruprecht - Karls - Universität Heidelberg

vorgelegt von

MSc. Stefan Andreas Scholl

aus Speyer

Heidelberg

2017

INAUGURAL - DISSERTATION

zur Erlangung der Doktorwürde

der Naturwissenschaftlich-Mathematischen Gesamtfakultät

der Ruprecht - Karls - Universität Heidelberg

vorgelegt von

MSc. Stefan Andreas Scholl

aus Speyer

Tag der mündlichen Prüfung: 14.07.2017

pH in the *trans*-Golgi network/early endosome of *Arabidopsis thaliana*: Suppliers and consumers

Gutachter: Prof. Dr. Karin Schumacher

Prof. Dr. Alexis Maizel

Table of contents

List of abbreviations

All element abbreviations follow IUPAC nomenclature

Amino acid abbreviations follow standard single letter code

%	percent
°C	degree Celsius
µE m^{-2} s^{-1}	micro Einstein per square meter per second
µg	micro gram
µl	micro litre
µM	micro molar
µm	micrometre(s)
6x OP	6x Operator-Promoter
aa	amino acid
amiR	artificial micro RNA
ATP	adenosine-triphosphate
AU	Airy unit
BCECF	2',7'-bis(2-carboxyethyl)-5(6)-carboxyfluorescein
BFA	Brefeldin A
bp	base pair(s)
BSA	bovine serum albumin
CCV	clathrin-coated vesicle
cDNA	complementary DNA
CDS	coding sequence
CHO	Chinese hamster ovary
CLSM	confocal laser scanning microscopy
Col-0	Columbia-0
cm	centimetre(s)
ConcA	Concanamycin A
CSC	cellulose synthase complex
Dex	dexamethasone
DMSO	dimethylsulfoxid

DNA	deoxyribonucleic acid
E.coli	*Escherichia coli*
e.g.	*exempli gratia*/ for example
eGFP	enhanced monomeric green fluorescent protein
ER	Endoplasmic Reticulum
F	filial generation
FM 4-64	(N-(3-triethylammoniumpropyl)-4-(6-(4-(diethylamino) phenyl) hexatrienyl) pyridinium dibromide)
FRET	Förster/Fluorescence resonance energy transfer
FRET-FLIM	FRET-Fluorescence lifetime imaging
gDNA	genomic DNA
h	hour(s)
HG	homogalactuoran
i.e.	*id est*/ that is
kb	kilobases
l	litre(s)
M	molar
min	minute(s)
ml	millilitre(s)
mM	millimolar
mRFP	monomeric red fluorescent protein
MS	Murashige & Skroog
MVB/LE	multivesicular body/late endosome
ng	nanogram
nM	nanomolar
nm	nanometre(s)
ORF	open reading frame
PBS	phosphate-buffered saline
PCR	polymerase chain reaction
PEG	polyethylene glycol
pH	potential of hydrogen/ *pondus hydrogenii*

PI3K	phosphatidylinositol 3-kinase
pKa	acid dissociation constant
PP_i	pyrophosphate
RNA	ribonucleic acid
RNAi	RNA interference
ROI	region of interest
r_p	Pearsons` correlation coefficient
r_s	Spearmans` correlation coefficient
rpm	rounds per minute
RT	room temperature (22°C)
RT-PCR	reverse transcription PCR
SD	standard deviation
SE	standard error
sec	second(s)
SNARE	soluble N-ethylmaleimidine sensitive factor attachment receptor
SV	secretory vesicle
T-DNA	transfer DNA
TGN/EE	*trans*-Golgi network/ early endosome
TM-score	template modeling score
Tobacco BY2	Tobacco bright-yellow 2
V-ATPase	vacuolar-type proton ATPase
V-PPase, VHP	H^+- pyrophosphatase
WT	wild type

Contribution to this work

The author declares that this work was written independently only with the sources indicated and not by services of a third party. Where the work of others has been quoted or reproduced, the source is always given. This work was not presented to a university as part of an examination or degree. Apart from the author and the supervisor following persons contributed to this work as indicated:

Macro generation for automated evaluation of pH measurements	Dr. Melanie Krebs
Cloning of tonoplast retargeting constructs Establishment of protoplasting protocol	Franziska Lesche
Cloning of UBQ10$_{Pro}$:SYP122-pHusion	Lotte Bald
Support with transmission electron microscopy	Dr. Stefan Hillmer and Stefanie Gold
Generation and characterisation of amiR-*vha-a1* lines	Dr. Anne Kriegel

Parts of this work have been published in:

Luo, Y.*, Scholl S.*, Doering, A.*, Zhang, Y., Irani, N.G., Di Rubbo, S., Neumetzler, L., Krishnamoorthy, P. Van Houtte, I., Mylle, E., Bischoff, V., Vernhettes, S., Winne, J., Friml, J., Stierhoff, Y.-D., Schumacher, K., Persson, S., and Russinova E. (2015). V-ATPase activity in the TGN/EE is required for exocytosis and recycling in Arabidopsis. Nat. Plants **1**: 15094.

* = equal contribution

Summary

The *trans*-Golgi network (TGN)/ early endosome (EE) is the main sorting station for proteins travelling along the secretory- or endocytic route. Acidification by the TGN/EE-localised vacuolar-type proton (H^+)-ATPase (V-ATPase) is essential for functional protein trafficking as well as compartment structure. Inhibition of this V-ATPase ceases protein trafficking through the TGN/EE and inhibits cell elongation. To sustain TGN/EE functions, luminal pH has to be kept on a homeostatic level. A mechanism to maintain V-ATPase-mediated acidification is to balance the bulk positive charges in the TGN/EE lumen accumulated by H^+ pumping via parallel anion import. However, previous measurements of V-ATPase-dependent acidification in the TGN/EE were mainly done in transient expression systems and used sensors suited for rather alkaline pH conditions. Furthermore, TGN/EE-localised anion transporter from the ClC-family which have been proposed to serve in luminal charge balance are largely uncharacterised. For that purpose, *in vivo* TGN/EE pH measurements using the genetically encoded pH sensor pHusion linked to the TGN/EE resident protein SYP61 were established. We determined that the steady state pH of 5,6 in the TGN/EE in Arabidopsis roots is controlled by the combined activity of the V-ATPase and H^+-coupled antiporters. Moreover the role of ClCd and ClCf in supporting the TGN/EE-localised V-ATPase in acidification was investigated. Whereas knock-out of both TGN/EE-localised ClCs caused male gametophyte lethality, we identified via inducible knock-downs an essential role of both transporters in cell elongation. However, neither TGN/EE pH nor TGN/EE-mediated trafficking was altered upon reduced reduction of *ClCf* in the *clcd* background. Curiously, *trans*-Golgi pH was more acidic than WT due to a partial mislocalisation of the TGN/EE-localised V-ATPases to the Golgi stack. Finally, a computational modelling approach suggested that ClCd functions as Cl^-/H^+ antiporter whereas clear predictions on ClCf functions could not been made. We established a method to measure V-ATPase-mediated TGN/EE acidification *in vivo* in *Arabidopsis thaliana*. Furthermore, we showed that the TGN/EE is acidified by the V-ATPase and co-determined by TGN/EE-localised transporters. Besides V-ATPase activity, anion import in the TGN/EE mediated by two ClC members ClCd and ClCf is essential for cell elongation. By that we revealed a previously unknown role of luminal anion homeostasis in the TGN/EE.

Zusammenfassung

Das "*trans*-Golgi network (TGN)/ early endosome (EE)" ist das zentrale Verteiler-Kompartiment für Proteine, die über den sekretorischen und endozytischen Weg transportiert werden. Alle Transportfunktionen des TGN/EEs sowie dessen Struktur, sind abhängig von der Aktivität einer V-Typ H^+-ATPase (V-ATPase). Inhibierung dieser Protonenpumpe blockiert alle Proteintransportwege durch das TGN/EE und hemmt, als eine direkte Folge, die Zellelongation. Um eine korrekte Funktion des TGN/EEs zu gewährleisten ist es notwendig, dass der luminale pH Wert des TGN/EEs konstant gehalten wird. Ein Mechanismus hierfür ist ein Ladungsausgleich der positiven H^+ Ionen, die durch die V-ATPase zur luminalen Ansäuerung importiert werden, durch parallelen Anionen-Einstrom. Bisherige Messungen der V-ATPase-abhängigen Ansäuerung des TGN/EE Lumens wurden hauptsächlich in transienten Expressionssystemen durchgeführt, unter der Verwendung von pH Sensoren die in alkalischen Bedingungen funktional sind. Darüber hinaus wurden Anionen Transporter aus der ClC-Familie, die als Kandidaten zum Import von Gegenionen vorgeschlagen wurden, bisher nur marginal charakterisiert. Aus diesem Grund wurde in einem Teil dieser Arbeit eine Methode etabliert, um den pH Wert des TGN/EE von *Arabidopsis thaliana, in vivo* zu messen. Für die spezifische Messung im TGN/EE wurde der genetisch-kodierte pH Sensor pHusion mit dem TGN/EE lokalisierten Protein SYP61 gekoppelt. Mit dieser Methode konnte in Wurzeln von *Arabidopsis thaliana* ein pH Wert von 5,6 im TGN/EE gemessen werden, der zum Einen von der V-ATPase und zum Anderen von H^+ gekoppelten K^+ Antiporter der NHX-Klasse bestimmt wird. Desweiteren wurden zwei TGN/EE lokalisierte, potenzielle Anionen/H^+ - Transporter aus der ClC-Familie, ClCd und ClCf, untersucht und deren Rolle im Ladungsausgleich des TGN/EE Lumen charakterisiert. Ein gentischer knock-out von ClCd und ClCf ist letal für den männlichen Gametophyten sodass durch eine induzierbare, artifizielle micro RNA gegen *ClCf* im *clcd* Hintergrund gezeigt werden konnte, dass ClCd und ClCf eine essentielle Rolle in der Zellelongation besitzen. Eine Veränderung des TGN/EE pH konnte hingegen nicht festgestellt werden und der intrazellulärer Transport ausgehend vom TGN/EE war in induzierten knock-downs von *ClCf* in *clcd* ebenfalls nicht beeinträchtigt. Interessanterweise wurde eine Ansäuerung der *trans*-Golgi Zisterne gemessen, die durch teilweise Misslokalisation der TGN/EE-lokaliseren V-ATPase zur *trans*-Golgi Seite bedingt wurde. Schließlich wurde über computerbasiertes Modelling eine Funktion von ClCd als Cl^-/H^+ Antiporter vorgeschlagen. Die Funktion von ClCf und das durch ClCf transportierte Anion konnte nicht zweifelsfrei bestimmt werden. Durch *in vivo* TGN/EE pH Messungen wurde gezeigt, dass der TGN/EE pH durch die V-

ATPase generiert und durch TGN/EE-lokalisierte Transporter beeinflusst wird. Desweiteren ist neben Protonenimport durch die V-ATPase, Anionenimport in das TGN/EE durch die zwei ClC Transporter ClCd und ClCf essentiell für die Zellelongation, womit eine bisher unbekannte, physiologische Rolle von Anionen/Chlorid im TGN/EE identifiziert wurde.

.

1. Introduction

Due to their sessile lifestyle, plants have to adapt to environmental changes such as nutrient availability, light intensity and biotic/abiotic stresses as efficiently as possible (Viotti et al., 2010). Thereby external signals are transmitted to the cell interior to adjust the entire cellular metabolism to new conditions. A key process in transmission is the dynamic regulation of density and composition of plasma membrane-localised receptors, transporters and other proteins through the secretory and endocytic pathway (Reyes et al., 2011). As a matter of course, these responses involve not only re-arrangement and turnover of proteins but also massive *de novo* protein synthesis and targeted protein sorting. An eukaryotic cell features specialised compartments in protein synthesis, distribution and degradation (Contento and Bassham, 2012). Thereby, luminal pH is a crucial condition. Nearly all biochemical reactions, enzyme activities as well as protein structures and receptor-ligand interactions are pH dependent (Casey et al., 2010). Furthermore, proton gradients drive secondary-active transport processes across membranes. Establishment and maintenance of distinct pH conditions determines unique functions of individual organelles and is hence an essential feature of compartimentalisation (Casey et al., 2010; Schumacher, 2014). Active import of protons (H^+) into endomembrane lumina is required to generate these high H^+ concentrations and H^+ gradients relative to the cytosol. Therefore proton pumps catalyse energy-driven H^+ accumulation in membrane-enclosed compartments. The major proton pump in eukaryotes represents the vacuolar-type H^+-ATPase (V-ATPase).

1.1. Vacuolar-type proton (H^+)-ATPases - structure and function

V-ATPases are electrogenic proton pumps that drive H^+ import from the cytosol into endomembrane lumina upon ATP hydrolysis (Schumacher and Krebs, 2010). They are divided into a membrane integral subcomplex (V_O) consisting of the subunits VHA-a, -c, c´´, -d, -e and a peripheral, cytosolic V_1 subcomplex composed of VHA-A, -B, -C, -D, -E, -F, -G and –H subunits (Nakanishi-Matsui et al., 2010; Schumacher, 2014) (Figure 1 A). To pump H^+ into lumina, cytoplasmic ATP is hydrolysed in the interstices of VHA-A and VHA-B of V_1, which effects rotation of the central stalk composed of the subunits VHA-D, VHA–d, -E and –F (Nakanishi-Matsui et al., 2010). Rotational energy is conducted to subcomplex V_O where VHA-a forms a pore together with -c and -c´´ subunits which bind and translocate H^+ across the membrane. Remaining subunits of the V_O complex provide membrane anchoring and are linked to V_1 by three peripheral stalks formed by VHA-E and VHA-G preventing co-rotation of the entire V_O

subcomplex (Nakanishi-Matsui et al., 2010; Schumacher and Krebs, 2010). Based on rotational structures of the V-ATPase from *Saccharomyces cerevisiae* obtained via cryo-EM, a ATP/H^+ coupling ratio of 3:10 was recently determined (Zhao et al., 2015).

In *Arabidopsis thaliana*, a V-ATPase complex consist of 13 subunits that are encoded by in total 28 genes (Schumacher and Krebs, 2010). In the plant cell, V-ATPases are located at two subcellular sites: At the vacuolar membrane (tonoplast) and at the *trans*-Golgi network (TGN)/ early endosome (EE). Localisation is determined by three isoforms of the VHA-a subunit in the V_O subcomplex which are incorporated during ER-assembly (Neubert et al., 2008). V-ATPases containing isoforms VHA-a2 and VHA-a3 localise to the tonoplast together with a second proton pump, the vacuolar H^+-pyrophosphatase (V-PPase) (Dettmer et al., 2006; Maeshima, 2001). V-ATPases that incorporated VHA-a1 reside at the TGN/EE (Dettmer et al., 2006) (Figure 1 B).

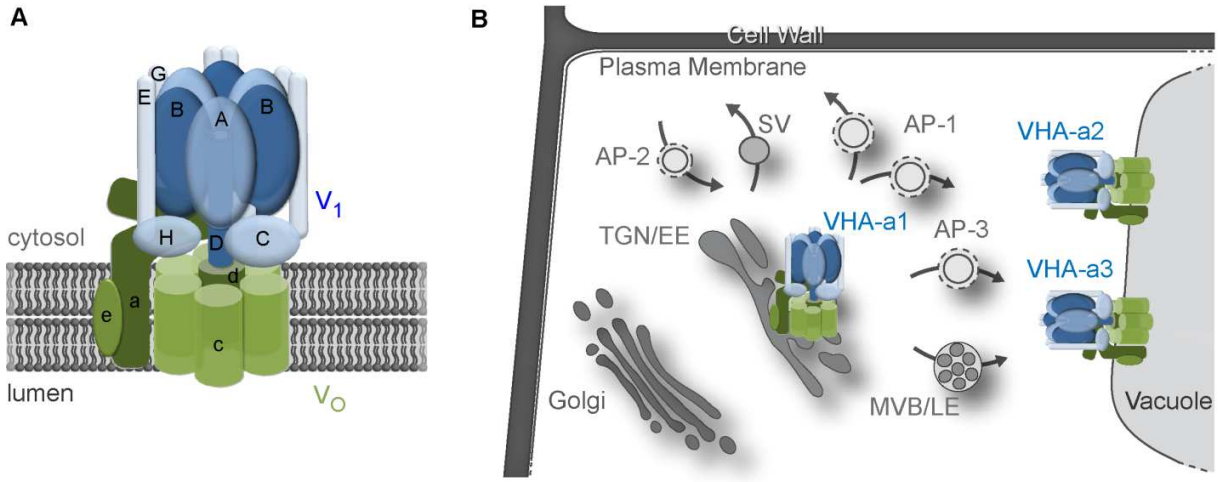

Figure 1: Structure and intracellular localisation of V-ATPases in *Arabidopsis thaliana*. (A) Structure and subunit composition of a V-ATPase complex. Subunits of the cytosolic V_1 subcomplex (blue) are depicted in capital letters, V_O components (green) are indicated in small letters. **(B)** Subcellular localisation of V-ATPases is dependent on VHA-a isoforms. VHA-a1-containing V-ATPases localise to the TGN/EE whereas V-ATPases that incorporated VHA-a2 and VHA-a3 localise to the tonoplast. Figures adapted and modified according to Schumacher and Krebs, 2010.

An indispensable role of the V-ATPase in plant development was demonstrated by Dettmer et al., 2005. A strong reduction of the subunit VHA-A common to all V-ATPase isoforms caused complete male gametophyte and partial female gametophyte lethality. Furthermore, cup-shaped Golgi stacks with swollen cisternae were detected in *vha-A* pollen. Similarly, a lack of the VHA-E1 subunit led to a disrupted Golgi organisation and cell wall defects altogether causing embryo lethality (Strompen et al., 2005). However, vacuolar morphology was unaltered in both mutants (Dettmer et al., 2005; Strompen et al., 2005; Schumacher and Krebs, 2010). A viable mutant

with a reduction in total V-ATPase activity is *det3 (de-etiolated 3;* Schumacher et al., 1999). *det3* has diminished total V-ATPase activity by 60% due to a weak allele of the V-ATPase mutual VHA-C subunit. Mutant plants display drastically reduced cell elongation, sensitivity to the plant hormone brassinosteroid and reduced cellulose content (Schumacher et al., 1999; Brüx et al., 2008). By generation of Arabidopsis mutants with affected single or multiple V-ATPase isoforms, insights into roles of the individual V-ATPases were possible. Plants lacking both tonoplastic V-ATPases containing VHA-a2 and VHA-a3 (*vha-a2 vha-a3*; Krebs et al., 2010) display a more alkaline vacuolar pH due to reduced H^+ import. Linked to this, the reduced H^+ gradient across the tonoplast causes that mutant plants accumulate less ions and nutrients in their vacuoles (Krebs et al., 2010). Above all, plants lacking both tonoplast V-ATPases and an active V-PPase (*fugu5-1*; Ferjani et al., 2011) are viable (Kriegel et al., 2015). In contrast, homozygous knock-out mutants against VHA-a1-containing V-ATPases could not be recovered so far (Brüx et al., 2008) proposing that the TGN/EE-localised V-ATPase is essential. An RNAi-mediated knock-down of VHA-a1 led to disrupted Golgi morphology and reduced cell expansion (Brüx et al., 2008). Thus, V-ATPase activity seems to be crucial for a functional TGN/EE which is the pivotal point of the endocytic and secretory pathway respectively.

1.2. The *trans*-Golgi network/early endosome – junction of secretory and endocytic pathway

The *trans*-Golgi network/early endosome (TGN/EE) represents the main sorting station for proteins coming from the secretory pathway as well as the endocytic pathway (Reyes et al., 2011). Here, proteins that are newly synthesised in the ER-Golgi system are distributed via extensive vesicle trafficking to the plasma membrane or the vacuole. Furthermore, the plant TGN also acts as an early endosome (Dettmer et al., 2006). It was shown by the rapid co-localisation of VHA-a1-GFP with the endocytic tracer FM 4-64 (Geldner et al., 2007) that the TGN/EE is the first compartment reached by endocytic cargo after intake from the plasma membrane. After endocytosis, proteins can either be cycled back to the plasma membrane or transported to the vacuole for degradation. The role as central hub for secretory and endocytic cargo was illustrated by Viotti et al. in 2010. An inducible, secreted GFP and the endocytosed proportions of the plasma-membrane localised boron exporter BOR1 (REQUIRES HIGH BORON1; Takano et al., 2002) co-localised at the TGN/EE labelled by VHA-a1. Identically, newly synthesised and endocytosed proteins of the plasma membrane brassinosteroid receptor BRI1 (BRASSINOSTEROID INSENSITIVE1; Friedrichsen et al., 2000) were located at the TGN/EE via immunogold labelling confirming that both secretory and endocytic pathway indeed

pass through the identical compartment. Similar observations were made in Tobacco BY-2 cells were the TGN-localised SCAMP1 (SECRETORY CARRIER MEMBRANE PROTEIN1) rapidly co-localised with FM 4-64 suggesting that in plants the TGN and EE represent the same compartment (Lam et al., 2007).

Structurally, the TGN/EE originates from the *trans*-Golgi stack via cistenal maturation (Kang et al., 2011) and appears as a tubular-vesicular cluster which was originally termed partially coated reticulum (Staehelin and Moore, 1995). The TGN/EE acts as an independent organelle that is transiently Golgi-associated and capable to undergo homotypic fusions (Viotti et al., 2010). It is hypothesised that Golgi- associated TGN/EEs predominantly exchange cargo with the Golgi stack whereas free TGN/EEs take up endocytosed cargo and function mainly in secretion and trafficking (Viotti et al., 2010; Reyes et al., 2011; Kang et al., 2011).

To sort and mediate transport of cargo to the different subcellular destinations the TGN/EE employs several proteins and effectors providing specificity in vesicular transport. Important regulators are RAB-GTPases which are determinants of membrane identity and membrane targeting (reviewed in: Woollard and Moore, 2008), and SNARE proteins (soluble N-ethylmaleimidine sensitive factor attachment receptor) as specific membrane fusion mediators (see: Grefen and Blatt, 2008 for review). In total, plants contain more RAB-GTPases and SNAREs involved in post-Golgi trafficking pathways that animals or yeast (Uemura, 2016). Moreover, several trafficking pathways emerge from the TGN/EE: Cargo destined for the vacuolar membrane (tonoplast) and lumen exits the TGN/EE via multivesicular bodies/late endosomes (MVB/LE) which directly mature from the TGN/EE and later on fuse with the tonoplast (Scheuring et al., 2011). Furthermore, two clathrin-coated vesicle (CCV) routes exist that depend on different ADAPTOR PROTEIN (AP) complexes responsible for mediation between cargo protein recognition and clathrin vesicle coat formation (Robinson, 2004). CCVs containing AP-3 complexes transport membrane integral proteins to the vacuolar membrane (tonoplast) (Feraru et al., 2010; Wolfenstetter et al., 2012). CCVs depending on AP-1 complexes appear to act not only in TGN-to-tonoplast trafficking (Wang et al., 2014) but also protein transport to the plasma membrane (Park et al., 2013; Teh et al., 2013) as well as cycling of endocytosed proteins (Wang et al., 2013; Robinson and Pimpl, 2014). Lastly, Boutté et al. verified the presence of secretory vesicle clusters (SVs) at the TGN/EE responsible for TGN/EE-to-plasma membrane trafficking of *de novo* synthesised proteins (Boutté et al., 2013) (Figure 1 B). Previously, mutants of the transmembrane protein ECHIDNA (ECH) were discovered to be defective in secretion but not endocytosis showing that both trafficking pathways are separate

(Gendre et al., 2011). The same publication proposed that TGN/EEs and Golgi stacks are less associated upon ECH loss. Furthermore, the TGN/EE receives endocytosed proteins that are internalised and transported via AP-2 dependent CCVs (Di Rubbo et al., 2013). Imported proteins are then either cycled back to the plasma membrane or transported to the vacuole via MVB/LEs for degradation and turnover (Künzl et al., 2016).

1.3. V-ATPase activity in the TGN/EE is essential

The importance of V-ATPase activity for TGN/EE function has been shown by either application of the macroloid antibiotic Concanamycin A (ConcA), a specific V-ATPase inhibitor (Huss et al., 2002), or inducible RNAi-mediated knock-down directed against VHA-a1 (Brüx et al., 2008). Upon V-ATPase inhibition via both approaches, TGN/EEs inflate and cluster and form together with a cup-shaped Golgi stack TGN-Golgi hybrid compartments. Furthermore it was shown that ConcA-mediated V-ATPase inhibition also reduces MVB/LE numbers (Scheuring et al., 2011). ConcA induces not only morphological changes but also effect a complete block of trafficking out of the TGN/EE, since transport of newly synthesised as well as endocytosed proteins is inhibited (Viotti et al., 2010). In the same publication it was shown that also cell wall matrix components such as xyloglucans accumulate in the TGN/EE lumen upon ConcA treatment. Consistent with these observations, induced RNAi knock-down approaches illustrated that seedlings with reduced levels of VHA-a1 display inhibited cell expansion and smaller hypocotyls of around 20 % compared to WT plants (Brüx et al., 2008). Since cell elongation in *vha-a2 vha-a3* mutants was only marginally affected experiments showed that the TGN/EE-localised V-ATPase is limiting for cell expansion (Brüx et al., 2008; Krebs et al., 2010; Schumacher and Krebs, 2010). All findings illustrate an essential role of the TGN/EE-localised V-ATPase in cell elongation and trafficking of proteins as well as cell wall matrix components.

In animal cells it is established that the V-ATPase is responsible for acidification of all secretory pathway organelles which become increasingly acidified along the secretory route from pH 7,4 in the ER down to pH 5,2 in secretory granules (for review see e.g. Paroutis et al., 2004; Casey et al., 2010). In plants, pH values of organelles in the secretory pathway are largely unknown and V-ATPase-mediated acidification has so far only been confirmed for the plant vacuole (Krebs et al., 2010; Kriegel et al., 2015). Available data concerning V-ATPase activity at the TGN/EE, which is represented by acidification to a large extend, has so far been measured mainly in transient expressing systems only (Martinière et al., 2013a; Shen et al., 2013).

1.4. pH measurements in the TGN/EE

Luminal pH represents one basic compartment condition which influences enzymatic activities as well as protein structure, the binding of ligands to their intracellular receptors and ultimately drives transport processes across membranes in form of the proton motive force (Casey et al., 2010). Since inhibition of the TGN/EE-localised V-ATPase causes compartment functions to cease, pH seems to be a crucial determinant. But how can pH be specifically determined in the TGN/EE? In animal cells measurements were performed by antibody-linked pH-sensitive probes targeting TGN/EE resident proteins during their brief transit the plasma membrane, for instance TGN38 (Demaurex et al., 1998; Paroutis et al., 2004). Another approach by Wu et al. generated avidin-chimeras with proteins or signal sequences localised to different compartments (Wu et al., 2001). By addition of membrane-permeable biotin linked to a pH probe, selective targeting of the pH indicator was achieved. Lastly, by tagging organelle-resident proteins or signal peptides with genetically-encoded pH sensors, specific targeting to the compartment of interest can be performed which allows *in vivo* measurements in a spacial and temporal manner.

An *in vivo* pH measurement approach in Tobacco and *Arabidopsis thaliana* by Martinière et al. in 2013 employed the genetically encoded pH sensor pHluorin linked to the TGN/EE- and MVB/LE-localised VACUOLAR SORTING RECEPTOR 4 (VSR4). pH was measured in areas co-localising with the TGN/EE resident SNARE protein SYP61 (SYNTAXIN Of PLANTS 61) and resulted in pH of 6,4 in Tobacco leaves and pH of 6,1 in *Arabidopsis thaliana* roots. Shen et al., 2013 reported of a TGN/EE pH of 6,2 in Arabidopsis protoplasts using the plant-solubility-modified PRpHluorin. Both approaches employed the pH sensor pHluorin which is a GFP derivate containing 9 point mutations compared to the original *Aquorea victoria* GFP making the sensor ratiometric (Miesenböck et al., 1998). However, pHluorin and derivates have a pK_a of 6,2 and therefore lose resolution in the acidic. The ratiometric PtGFP from *Ptilosarcus gurneyi* has an improved stability at low pH but is with an pK_a of 7,2 suited for rather alkaline pH (Schulte et al., 2006). However, PtGFP has so far only been used in cytoplasmic measurements in Arabidopsis (Schulte et al., 2006). Since the V-ATPase is located at the TGN/EE, pH of this compartment should be fairly acidic which favours the application of pH sensors with low pK_a values. Such pH sensors are for instance the FRET-based pHlameleon 5 (pKa = 5; Esposito et al., 2008) and the eGFP-mRFP tandem pHusion with a of pK_a = 5,8 (Gjetting et al., 2012). Whereas pHlameleon 5 has not been used *in planta* so far, a secreted pHusion variant was recently applied to monitor auxin-induced alkalisation of the apoplast (cell wall) in hypocotyls (Fendrych et al., 2016). Since a low apoplastic pH of 5,5 to 5,2 was determined close to the root

using a surface electrode (Staal et al., 2011), pHusion seems a suitable pH sensor for acidic conditions *in vivo*. pHusion would therefore be also a good candidate sensor to monitor TGN/EE pH.

1.5. The TGN/EE-localised V-ATPase contributes to vacuolar acidification

Recently, an Arabidopsis mutant has been generated which lacks all vacuolar proton pumps, both tonoplast V-ATPases and an active V-PPase (*fugu5-1*; Ferjani et al., 2011) (Kriegel et al., 2015). Plants display severely stunted growth and ion deficiency symptoms which can be linked to a diminished proton motive force across the tonoplast (Krebs et al., 2010). Still, mutants are viable by having a functional V-ATPase at the TGN/EE. Despite lacking all vacuolar proton pumps, vacuoles are still acidified to approximately pH 6,6 (WT = pH 5,8). Inhibition of the V-ATPase by ConcA effected an alkalisation of the vacuolar pH to cytoplasmic values of pH 7,2 - 7,4 in WT and in *vha-a2 vha-a3 fugu5-1* which only have the TGN/EE-localised V-ATPase left as ConcA target (Kriegel et al., 2015). Since relocalisation of VHA-a1 to the tonoplast and a contribution of the plasma membrane-localised V-ATPase to vacuolar pH was excluded (Kriegel et al., 2015) an additional role of the TGN/EE-localised V-ATPase in vacuolar acidification was revealed. The TGN/EE is connected to the vacuole via three TGN-to-vacuole trafficking pathways involving MVB/LE and CCVs dependent on the adaptor protein complex AP-3 and AP-1 (Figure 1 B). So far, it is unknown whether H^+ are transported via one or several of the trafficking pathways from TGN/EE to the vacuole.

Furthermore, a communication between the vacuolar and the TGN/EE-localised V-ATPase pool has been proposed. An artificial micro RNA (amiR)-mediated knock-down of VHA-a1 at the TGN/EE led to an increase in vacuolar pH in Arabidopsis roots (Dissertation Dr. Anne Kriegel 2015). Moreover, induction of the amiR against VHA-a1 in the *vha-a2 vha-a3* background did not alter vacuolar pH. The observed acidification was thus caused by an activity increase of both tonoplastic V-ATPase isoforms (Dissertation Dr. Anne Kriegel 2015). Hence a communication of vacuolar and TGN/EE-localised V-ATPase isoforms was hypothesised. How both V-ATPases feed-back on each other and whether this feedback acts uni- or bidirectionally is currently unknown.

1.6. pH homeostasis in the TGN/EE

Since the activity of the TGN/EE-localised V-ATPase is crucial for compartment functions, pH within this organelle has to be tightly regulated. Due to the electrogenic nature of the V-ATPase an inside positive electric potential is generated. Anion conductance is required to counter the

bulk positive charge which would shut down V-ATPase activity before a significant pH gradient is built up (Paroutis et al., 2004; Schumacher and Krebs, 2010; Stauber and Jentsch, 2013). Furthermore, a proton leak is necessary to prevent over-acidification of endomembrane lumina (Orlowski and Grinstein, 2007; Bassil et al., 2012). Although V-ATPases are responsible for luminal proton import, activity of TGN/EE-localised ion/H^+ antiporters might take over those regulatory roles and fine tune the pH gradient generated by the proton pump (Pittman, 2012). The steady state pH of a compartment finally represents the net result of all proton im- and export processes (Schumacher, 2014). The role of a proton leak has been assigned to NHX-family of potassium (K^+)/H^+ antiporters, of which NHX5 and NHX6 have been localised to the TGN/EE in plants (Bassil et al., 2011). However, to enable acidification by the V-ATPase, luminal influx of anions is required to sustain H^+ accumulation (Pittman, 2012). Sonawane et al., 2002 showed that endosomal chloride (Cl^-) concentration correlated with an increase in pH in CHO (Chinese hamster ovary) cells. Besides pH regulation, Cl^- has been shown to be crucial for functional intracellular trafficking in animals (Novarino et al., 2010; Weinert et al., 2010) and it is becoming increasingly clear that Cl^- has also physiological roles beyond serving as a mere shunt (Stauber and Jentsch, 2013). A transporter family which has long been implicated to function in pH and ion homeostasis are the ClC-family of chloride transporters and channels.

1.7. ClC-family of chloride channels and transporters

ClC (CHLORIDE CHANNEL) proteins comprise a family of Cl^- channels and Cl^-/H^+ proton antiporters that are present in all kingdoms of life (Miller, 2006). In mammals, nine members are divided into Cl^-/H^+ exchangers distributed across the secretory pathway (ClC-3 to ClC-7) and plasma membrane-localised Cl^- channels (ClC-1, -2, -Ka, -Kb) (Stauber and Jentsch, 2013). Despite the two operation modes, all members share a high structural similarity. Moreover, all ClCs form rhombus-like homodimers whereby each monomer possesses an independent ion transport pathway (Stauber and Jentsch, 2013; Accardi, 2015). A $2Cl^-/1H^+$ transport stoichiometry has been determined for the first prokaryotic ClC-ec1 antiporter from *Escherichia coli* (*E.coli*) (Dutzler et al., 2003) but also for all mammalian (ClC-3 to -7) antiporters as well as for CmClC (Feng et al., 2010) from the thermophilc red algae species *Cyanidioschyzon merolae*.

Plants comprise seven ClC proteins (Zifarelli and Pusch, 2010). All plant ClC members are ubiquitously expressed and quantitative expression analysis detected relatively equal expression levels in all plant organs (De Angeli et al., 2009). By using fluorescent fusions and knock-out mutants, the subcellular localisations as well as physiological roles of the majority of ClC members have been revealed *in vivo* in Arabidopsis. However, the exact mode of transport, as

well as the transported anion remains elusive except for two members. Both tonoplast-localised ClCa (De Angeli et al., 2006) and ClCb (von der Fecht-Bartenbach et al., 2010) have been confirmed via electrophysiological measurements to specifically mediate proton coupled exchange of nitrate (NO_3^-). For ClCa, a $2NO_3^-/1H^+$ stoichiometry has been identified (De Angeli et al., 2006). Knock-out plants of ClCa therefore accumulate 50% less NO_3^- in their vacuoles than WT (De Angeli et al., 2006) assigning ClCa to be required for main vacuolar NO_3^- homeostasis. ClCc has been shown to be located at vacuoles of stomata, pollen and to a lesser extend in root tissues (Jossier et al., 2010). Mutant analysis determined a function in stomata opening and salt tolerance by regulating Cl^- but not NO_3^- homeostasis. The tonoplast localised ClCg is predominantly expressed in mesophyll cells, hydrathods and in phloem cells and has been related to function in shoot Cl^- exclusion (Nguyen et al., 2016). The only thylakoid-localised ClC family member ClCe was proposed to function in Cl^- homeostasis after dark-to-light transition regulating thylakoid structure and photosynthetic electron transport (Herdean et al., 2016). Nonetheless, mode of action is, as in ClCc and -g, unknown.

Two plant ClC members are located at other sites of the endomembrane system. ClCd is found mainly at the TGN/EE (von der Fecht-Bartenbach et al., 2007) while ClC-f has been localised in transient expressions at *cis*-, as well as *trans* side of the Golgi stack (Marmagne et al., 2007). Both ClCd and ClCf were able to complement the pH-dependent growth phenotype of yeast strain *gef1* which contains a deletion in the single, Golgi-localised ScClC (Hechenberger et al., 1996; Gaxiola et al., 1998; Marmagne et al., 2007) suggesting a similar function as ScClC. ClCd knock-outs displayed reduced cell elongation when treated with the V-ATPase inhibitor Concanamycin A and inhibited root growth in alkaline medium (von der Fecht-Bartenbach et al., 2007). Thus, a role for ClCd in pH adjustment of the TGN/EE lumen has been suggested (Figure 2). No *in vivo* data for ClCf is available so far.

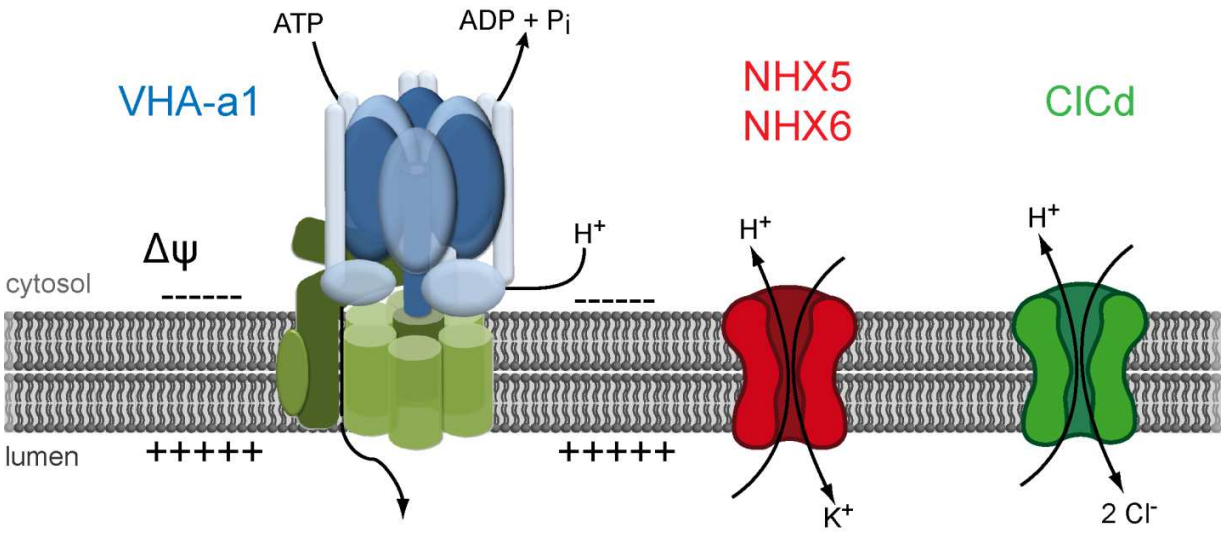

Figure 2: Simplified model of factors potentially influencing TGN/EE pH. VHA-a1-containing V-ATPases generate an inside positive electric potential by the import of protons. Accumulating positive charges have to be counterbalanced in order to prevent stalling of V-ATPase activity. Therefore ClCd has been proposed to provide anions for luminal charge balance to enable V-ATPase-mediated acidifications. To prevent luminal overacidification, NHX-family proteins remove positive charges by electroneutral exchange of H^+ against K^+.

However, if ClCd would support the V-ATPase in acidification, it is remarkable that ClCd knock-outs do not show phenotypes under standard growth conditions (von der Fecht-Bartenbach et al., 2007) as TGN/EE acidification has been shown to be essential (Dettmer et al., 2006; Brüx et al., 2008; Viotti et al., 2010). This raises the question whether ClCd acts as the attributed shunt for VHA-a1-containing V-ATPases and in endosomal pH regulation, or whether a second protein with redundant functions is present. A good candidate poses ClCf despite its intriguing localisation to mainly *cis*-Golgi compartments in a transient expression system (Marmagne et al., 2007). Therefore, *in vivo* studies regarding possible roles of ClCf and ClCd in pH and ion homeostasis of the TGN/EE are required.

1.8. Structural features of ClC transporter

So far five ClC proteins were crystallised, among them ClC-ec1 from *E.coli* (Dutzler et al., 2003) and CmClC (Feng et al., 2010) from the red algae *Cyanidioschyzon merolae*. Very recently the crystal structure of the first ClC channel ClC-K from bovines was determined (Park et al., 2017). Using the structure of ClC-ec1 many features of the anion transport mechanism were revealed.

Each monomer forms a separate ion transport pathway. In each pathway four critical amino acids determine substrate binding, specificity and H^+ coupling. A "gating" glutamate (E149 in *E.coli*), which is conserved in all ClC proteins, serves as gate between pore and external solution (Accardi, 2015). A central serine and tyrosine act as anion selectivity filter and coordinate the dehydrated Cl^- via hydroxyl groups through the transporter pore (Miller, 2006). In ClCa, this serine residue is replaced by proline conferring NO_3^- over Cl^- selectivity (Wege et al., 2010). Lastly, a "proton" glutamate (E203 in *E.coli*) is responsible for H^+ binding and coupling to Cl^- exchange (Miller, 2006) (Figure 3). Presence or absence of this amino acid determines between Cl^-/H^+ antiporter and Cl^- channel. All ClC channels in mammals carry a valine residue at "proton" position and thus function independently of H^+ coupling (Accardi, 2015). All ClC antiporter contain glutamate at this position, or threonine in case of CmClC (Feng et al., 2010).

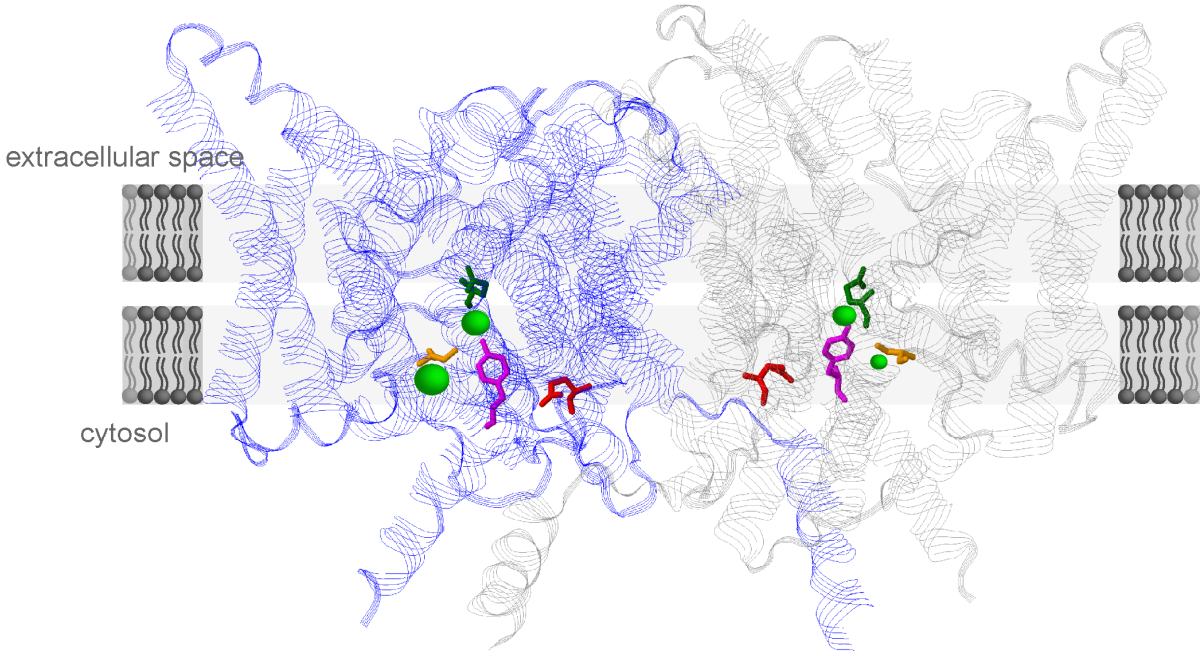

Figure 3: Overview of ClCec-1 dimer and localisation of critical residues for chloride anion transport. Mesh structure of the ClC-ec1 dimer with highlighted monomers (blue, gray). Amino acids for chloride selectivity and proton coupling are depicted as stick models and represent "gating glutamate" E149 (green), "proton glutamate " E203 (red), "chloride selectivity filer" serine S 107 (orange) and tyrosine Y 445 (magenta). Chloride ions are coded in bright green.

Due to presence of a "proton" glutamate and a serine in the selectivity filter domain, the TGN/EE-localised ClCd has been proposed to function as a Cl^-/H^+ antiporter (von der Fecht-Bartenbach et al., 2007). ClCf has been postulated to have channel like residues and amino acids in the anion selectivity filter differing from the conventional ClC sequences (Zifarelli and

Pusch, 2010). However, predictions have been made solely on a "2 dimensional" amino acid sequence alignments where structural and positional information of each amino acid within the protein are neglected. A 3D structure prediction of both endosomal ClCs might aid in identification of critical residues for ion selectivity and mode of action to gain first insights into their function. Still, predictions cannot replace an experimental characterisation.

Aims of this study

V-ATPase activity in the TGN/EE is essential for compartment functions. Previous TGN/EE pH measurements were performed with pHluorin-based pH sensors (Shen et al., 2013; Martinière et al., 2013a) which are suitable for measurements in alkaline conditions. Therefore, this thesis aimed to measure TGN/EE in *Arabidopsis thaliana* using a pH probe appropriate for more acidic pH and to determine the contribution of the V-ATPase to compartment pH. In that respect, a toolset of compartment specific pH sensors for other secretory pathway organelles was generated to enable identification of players involved in generation and maintenance of compartment pH.

Since the V-ATPase is electrogenic, anion conductance is required to enable compartment acidification by the V-ATPase. The TGN/EE-localised anion/ H^+ transporter ClCd has been suggested to be required for TGN/EE pH homeostasis. However, the absence of a strong *clcd* knock-out phenotype suggests functional redundancy. We further characterised the role of ClCd in TGN/EE pH homeostasis and whether the so far uncharacterised ClCf is implicated in similar processes.

Vacuoles without proton pump activity at the tonoplast are still acidified to roughly pH 6,6. This residual acidification is neutralised upon ConcA treatment. Since the only ConcA target left in those plants represents the TGN/EE-localised V-ATPase, a contribution of the TGN/EE to vacuolar pH was proposed. The TGN/EE is connected to the vacuole via at least three trafficking pathways. We therefore determined the impact on vacuolar pH in mutants or pharmacological treatments interfering with the individual trafficking pathways to test the hypothesis of a vesicular proton import from the TGN/EE to the central vacuole.

2. Results

2.1. *In vivo* pH measurements in the TGN/EE of *Arabidopsis thaliana*

2.1.1. Generation of a TGN/EE-localised pH sensor

To specifically target a pH sensor to the TGN/EE, linkage to a TGN/EE-resident protein was performed. The SNARE protein SYP61 (SYNTAXIN OF PLANTS 61), a part of the SYP41/SYP61/VTI12 Q-SNARE-complex at the TGN/EE (Sanderfoot et al., 2001), overlapped with VHA-a1-containing V-ATPases in dot-like, motile signals (Figure 4 A). We subsequently determined co-localisation of SYP61 with VHA-a1 in cells of 6 days old Arabidopsis roots. To define maximum degree of co-localisation of the microscopical setup, Pearson correlation coefficient (r_p) for immobile TetraSpeck^{TM} beads was calculated. Here, a r_p of 0,83 was determined (Figure 4 B). Signals of SYP61-CFP and VHA-a1-mRFP co-localised to a high degree (r_p = 0,78) and were close to the value obtained with the fluorescent microspheres (Figure 4 C). These results confirmed that SYP61 is located at the TGN/EE and thus is a suitable target protein for a TGN/EE-localised pH probe.

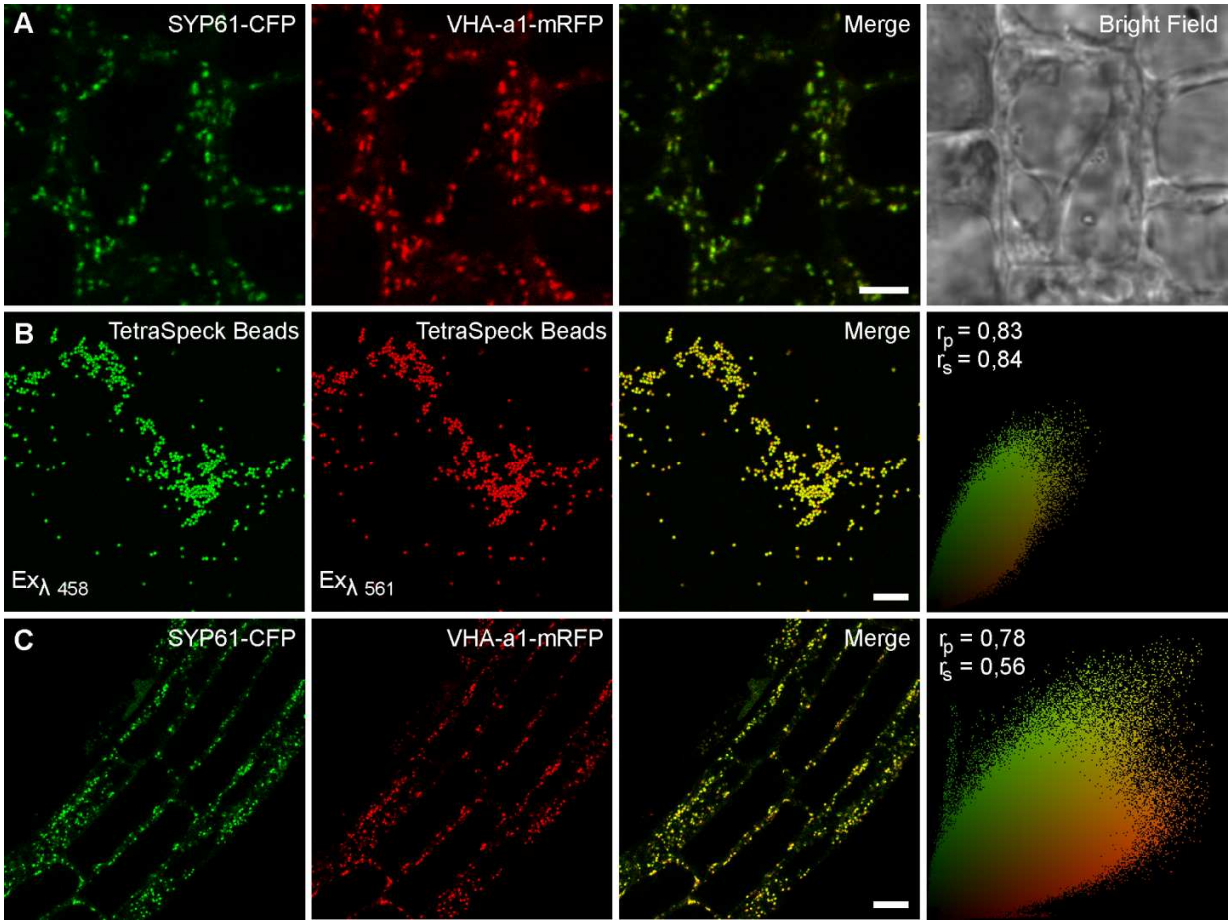

Figure 4: SYP61-CFP co-localises with VHA-a1-mRFP. Confocal laser scanning microscopy (CLSM) images of 6 days old Arabidopsis root cells and quantification of co-localisation using Pearson (r_p) and Spearman (r_s) correlation coefficients. Correlations range from +1 for positive, and -1 for negative correlation. r_p and r_s with respective scatterplots are shown on the right of each series. **(A)** SYP61-CFP and VHA-a1-mRFP displays high signal overlap in punctate structures. **(B)** TetraSpeck™ fluorescent microspheres of 1 µm in diameter. **(C)** Arabidopsis lines stably co-expressing SYP61-CFP and VHA-a1-mRFP. Bars = 5 µm **(A)**; 10 µM **(B, C)**. Scatterplots and correlations were generated from n=30 images for **(B)** or n=5 images of 10 roots for **(C)**.
Results are published in Luo et al. 2015.

To measure the potentially highly acidic pH in the TGN/EE we chose the ratiometric sensor pHusion due to its` ability to resolve low pH values down to pH 4,5 (Gjetting et al., 2012). pHusion consists of eGFP which has pH-dependent emission properties linked to the pH-stable mRFP for internal normalisation (Figure 5 A). In order to target the pH sensor to the TGN/EE lumen we tagged the C- terminus of SYP61 with pHusion (SYP61-pHusion) (Figure 5 B). Additionally, N-terminal coupling of pHusion to SYP61 (pHusion-SYP61), expected to locate the sensor to the cytosolic face of the TGN/EE, was used as a control (Figure 5 B). Both constructs were driven by the P16 promoter (Schlücking et al., 2013) for *in planta* overexpression. We observed a motile, dot-like pattern for SYP61-pHusion and pHusion-SYP61 (Figure 5 C, D) respectively. Furthermore, signals for both constructs accumulated in the core of BFA (Brefeldin A) compartments (Supplementary Figure S1). Constructs of either orientation could be exited with 488 nm and 561 nm laser lines demonstrating that eGFP and mRFP of pHusion were functional and not proteolytically cleaved. Ultimately, we performed immunogold labelling of high pressure frozen and freeze substituted 6 days old Arabidopsis seedlings expressing SYP61-pHusion using antibodies directed against GFP. Gold particles were detected at the TGN/EE (Figure 5 E, F) which altogether confirmed a successful targeting of pHusion linked to SYP61 to the TGN/EE.

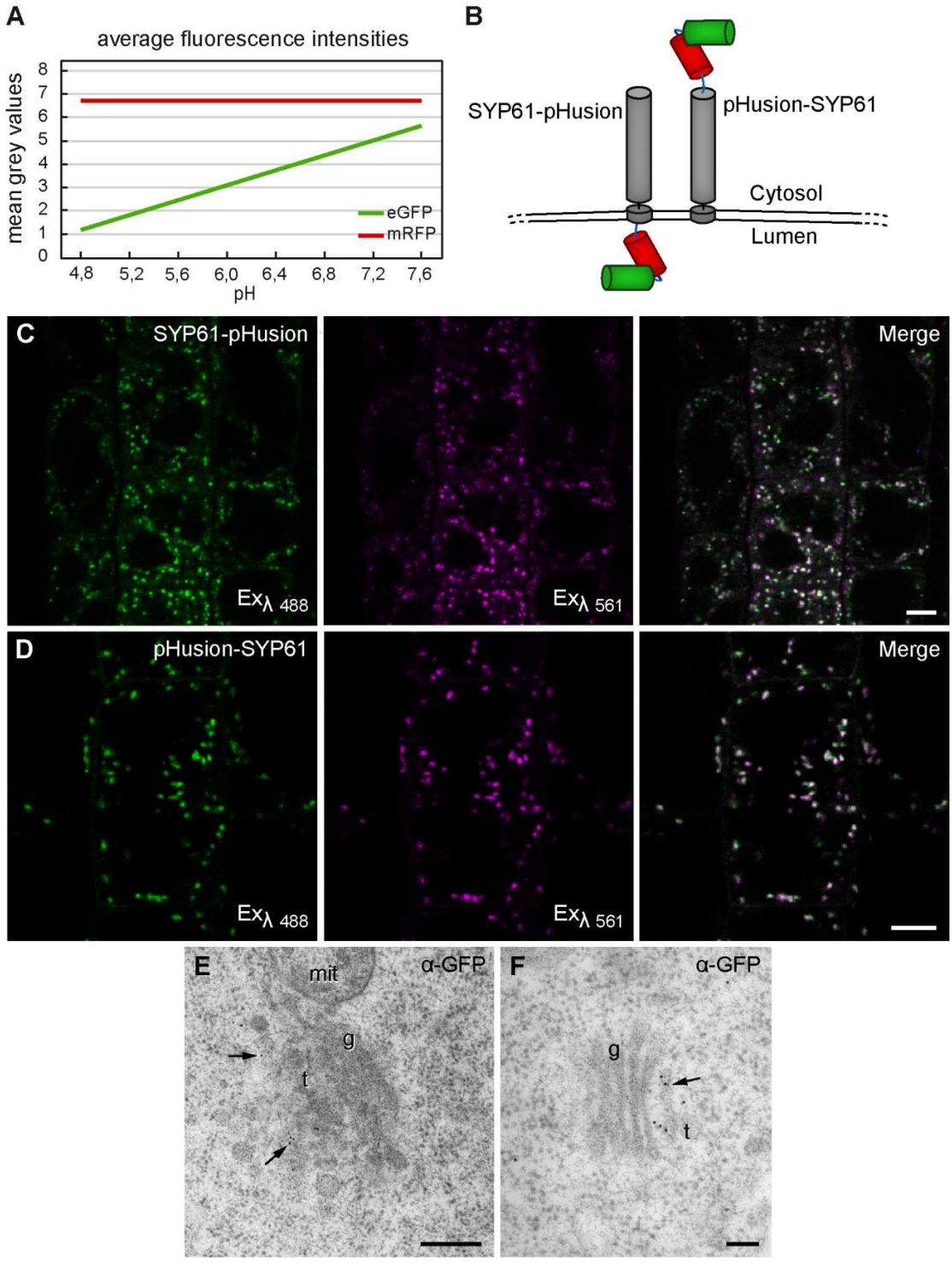

Figure 5: SYP61-pHusion localises to the TGN/EE in *Arabidopsis thaliana*. CLSM images and immunogold labelling of high-pressure frozen, freeze substituted 6 days old Arabidopsis root cells expressing $P16_{Pro}$:SYP61-pHusion or $P16_{Pro}$:pHusion-SYP61. **(A)** Operation method of pHusion. Emission intensity of eGFP increases with rising pH conditions whereas mRFP emission is pH independent. **(B)** Schematic overview of TGN/EE pH sensor constructs and sensor orientation.

Figure 5 (continued)

(C) SYP61-pHusion is exited with 488 nm and 561 nm laser lines and both signals display a dot-like pattern. **(D)** pHusion-SYP61 shows similar signals as SYP61-pHusion. **(E), (F)** SYP61-pHusion could be detected at the TGN/EE (arrows) using α-GFP antibodies on HM-20 embedded root tips. Abbrevations: g = Golgi apparatus, mit = mitochodrium, t = TGN/EE. Bars = 5 µm **(C, D)** 300 nm **(E)** or 100 nm **(F)**.
Images in **(C)** and **(D)** are published in Luo et al. 2015.

In order to test whether pHusion responds to different pH values *in vivo*, we equilibrated intracellular pH by buffer systems of defined pH containing ammoniumacetate (Yoshida, 1994). pH equilibration buffers were applied in presence of 1µM Concanamycin A (ConcA) to prevent V-ATPases from counteracting changes in intraluminal pH evoked by ammoniumacetate (Figure 6 A). To determine kinetics of intracellular pH changes after buffer application, eGFP/mRFP intensity ratios were recorded after application of pH equilibration buffers with different pH values over time. Thereby, ratios of the prospective luminal pH probe SYP61-pHusion were taken in single scans to avoid spectral crosstalk between both fluorophores.

A stable initial eGFP/mRFP ratio of around 0,3 over 5 min was measured which increased rapidly 30 sec after addition of pH 7,6 equilibration buffer. A plateau was reached at a ratio of 1,1 approximately 3 to 4 min after buffer application (Figure 6 B). In subsequent treatments of equilibration buffers with pH 6,8 and pH 6,0 ratios systematically decreased with equal dynamics. Upon pH 5,2 buffer treatment, ratio dropped to 0,24 to 0,23 which was lower than the initial ratio of 0,3 (Figure 6 B). Next, we investigated whether both fluorophores responded correctly to pH changes i.e. eGFP intensity varies with altering pH, mRFP fluorescence intensity remains constant. Also we ascertained the lowest pH possible before complete eGFP quenching. Therefore, entire seedlings were incubated in calibration buffers in presence of 1 µM Concanamycin A (ConcA) for 15 min to ensure complete equilibration of intracellular pH to external values. We observed the weakest eGFP fluorescence at pH 4,8 (Figure 6 C) and highest eGFP intensity at pH 7,6 (Figure 6 D). In both treatments, mRFP intensity remained identical. Untreated roots of SYP61-pHusion resulted in low eGFP/mRFP ratios (Figure 6 E). In conclusion, pHusion is able to respond to changes of intracellular pH which can be effectively manipulated using ammoniumacetate-based pH equilibration buffers. Moreover, low ratios for SYP61-pHusion were obtained in all experiments pointing to an acidic pH in the TGN/EE.

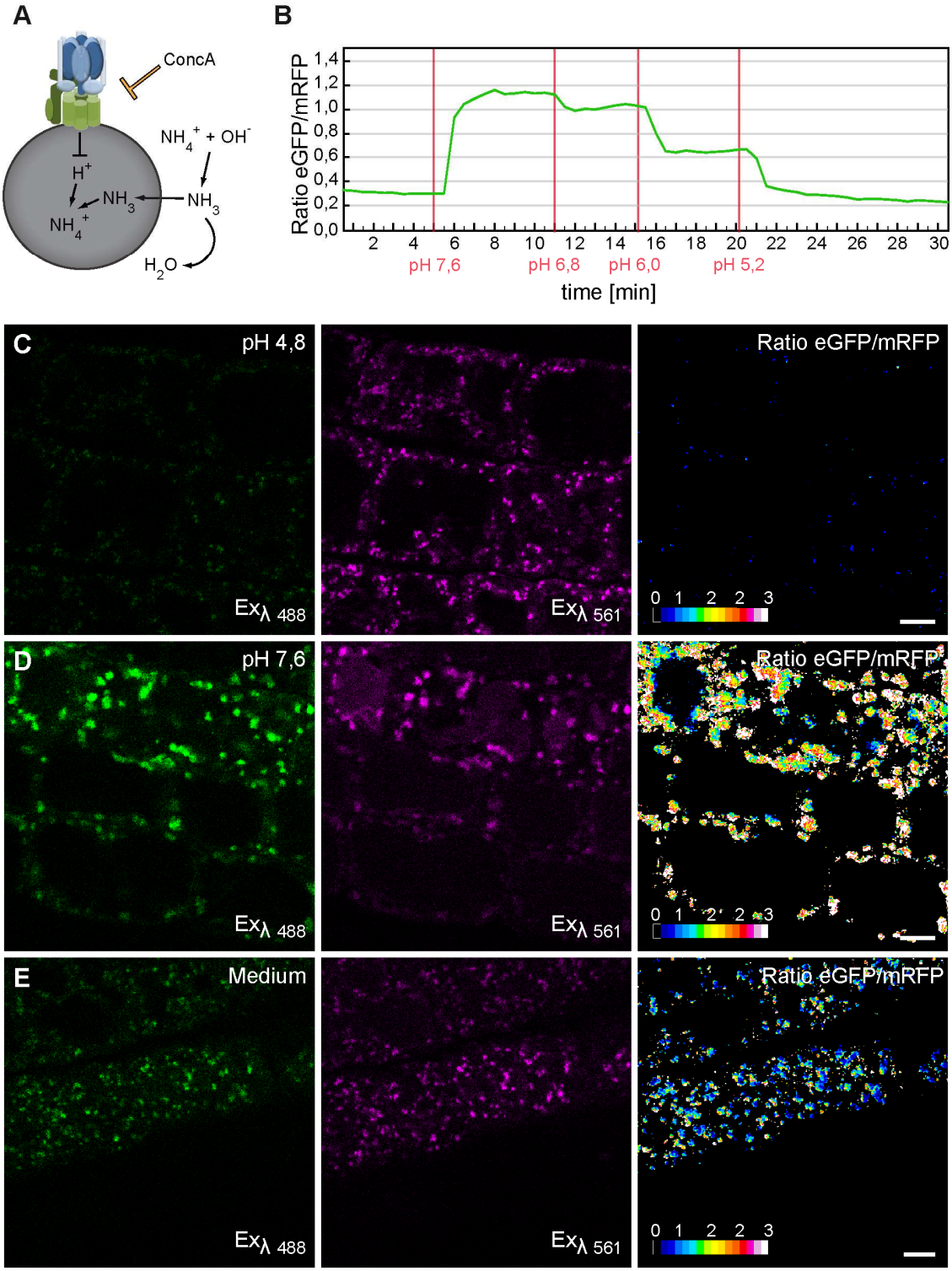

Figure 6: SYP61-pHusion responds to changes in intracellular pH. CLSM images of 6 days old Arabidopsis seedlings stably expressing $P16_{Pro}$:SYP61-pHusion after treatment with pH equilibration buffers containing 50 mM ammoniumacetate. **(A)** Ammoniumacetate equilibrates pH of endomembrane lumina (gray circle) to external buffer values by weak acid/weak base partitioning.

Figure 6 (continued)

By addition of the V-ATPase inhibitor Concanamycin A (ConcA) further influx of protons is hindered to ensure stable and complete pH equilibration.Scheme modified after (Poëa-Guyon et al., 2013)**. (B)** eGFP/mRFP ratios (green) were recorded in single scans over 30 min with 30 second frames. Red bars and numbering represent pH value and time at addition of the respective pH calibration buffer. Changes in eGFP/mRFP ratios occured withing 30 sec after buffer addition and plateau phase is adjusted approximately after 3 to 4 min. **(C)** CLSM image series of SYP61-pHusion incubated in pH equilibration buffer pH 4,8 for 15 min and eGFP/mRFP ratio of respective single channel images **(D)** CLSM image series of SYP61-pHusion incubated 15 min in pH equilibration buffer pH 7,6 and eGFP/mRFP ratio image. **(E)** CLSM image series of SYP61-pHusion in 1/2 MS, pH 5,8 medium and corresponding eGFP/mRFP ratios. Bars = 5 µm, ratio values in **(C, D, E)** range from 0 = low pH to 3 = high pH. All images were taken with constant microscope settings.

2.1.2. Measurement of the TGN/EE pH using SYP61-pHusion and SYP61-pHusion 2

Determination of absolute pH values requires *in vivo* calibration of a pH sensor. For that purpose eGFP/mRFP intensity ratios of seedlings expressing SYP61-pHusion were recorded after 15 min incubation in pH calibration buffers supplied with 1 µM ConcA. Measured average values in epidermal cells of the root elongation zone were afterwards plotted against the respective buffer pH resulting in a sigmoidal calibration curve (Figure 7 A). Thereby, fluorescence intensity values of eGFP increased with rising pH whereas mRFP values were independent of pH (Figure 7 B). These results verified functionality of pHusion as pH sensor and our *in vivo* calibration. Subsequently, *in vivo* calibration was performed for pHusion-SYP61 and a free cytosolic version of pHusion, where in both cases a sigmoidal curve was obtained (Supplementary Figure S2 A, B). Via *in vivo* pH measurements of 6 days old Arabidopsis seedlings we assessed pH of all three constructs maintaining microscope settings identical to the respective calibrations. For the C-terminal pHusion linkage to SYP61 we received an average steady state pH of 5,6 (Figure 7 C). With pHusion-SYP61 a pH value of approximately 7,2 was measured, which resembled values determined with free cytosolic pHusion (pH 7,29) (Figure 7 C). Altogether, these results confirmed that pHusion is exposed in the TGN/EE lumen when fused C-terminally to SYP61. Ultimately, treatment of seedlings expressing SYP61-pHusion with the ionophore Monensin, which causes swelling of the TGN/EE and Golgi stack by exchange of luminal protons with sodium (Na^+) ions (Mollenhauer et al., 1990), effected a rapid neutralisation of TGN/EE pH (Figure 7 D). Nevertheless, strong expression levels were required to detect mRFP signals. Furthermore, mRFP was rapidly bleached at prolonged laser exposure making long term measurements difficult.

To improve brightness and photostability of pHusion, we exchanged the mRFP component with the fluorescent protein mCherry which has improved photostability and brightness with identical pH stable emission properties (Shaner et al., 2005). pHusion 2 was linked C-terminally to SYP61 under control of the Ubiquitin 10 (UBQ10) promoter (Norris et al., 1993). *In vivo* calibration of Arabidopsis lines expressing SYP61-pHusion 2 resulted in an identical dynamic range and emission properties at varying intracellular pH as shown for the original pHusion (Figure 7 E, F). However, signals were less prone to photobleaching and less excitation energy was required. Ultimately, we determined an average pH of 5,6 for the TGN/EE in all measurements using pHusion 2, corresponding to the previous TGN/EE pH measurements with pHusion (Figure 7 G). Thus, SYP61-pHusion 2 is a TGN/EE pH sensor with improved brightness and photostability.

2.1.3. The TGN/EE is the most acidic compartment of the secretory pathway

Since the TGN/EE steady state pH is substantially acidic, we asked whether this low pH is a general feature of the secretory pathway of whether other organelles differ in their luminal pH. We generated pH sensors for *cis*- and *trans*- side of the Golgi apparatus and the cell wall and conducted *in vivo* pH measurements in stable transgenic Arabidopsis lines according to the principle described for SYP61-pHusion. To measure Golgi pH, pHusion was linked to the C-termini of the established Golgi markers α-1-2 MANNOSIDASE I (ManI) for *cis*-Golgi localisation (Figure 8 A) and rat SIALYLTRANSFERASE (ST) for *trans*-Golgi pH measurements (Shen et al., 2013) (Figure 8 B). Similar to our TGN/EE pH sensor, we attached pHusion C-terminally to the plasma membrane-localised SNARE protein Syntaxin of Plants 122 (SYP122) in order to direct the pH probe towards the apoplast (Figure 8 C). After *in vivo* calibration of each sensor (Supplementary Figure S2 C-E) we determined an average pH of 6,7 in *cis*- Golgi cisternae which drops to pH 6,3 at the *trans*-Golgi side (Figure 8 D). Measurements in the apoplastic space of the root elongation zone resulted in a pH of 5,4. However, apoplastic pH was not uniform since ratios increased from root tip to the transition zone and subsequently lowered towards the differentiation zone (Supplementary Figure S2 F). With our toolset of pH probes, we showed increasing acidification along the secretory pathway towards the lowest pH of 5,6 in the TGN/EE (Figure 8 D).

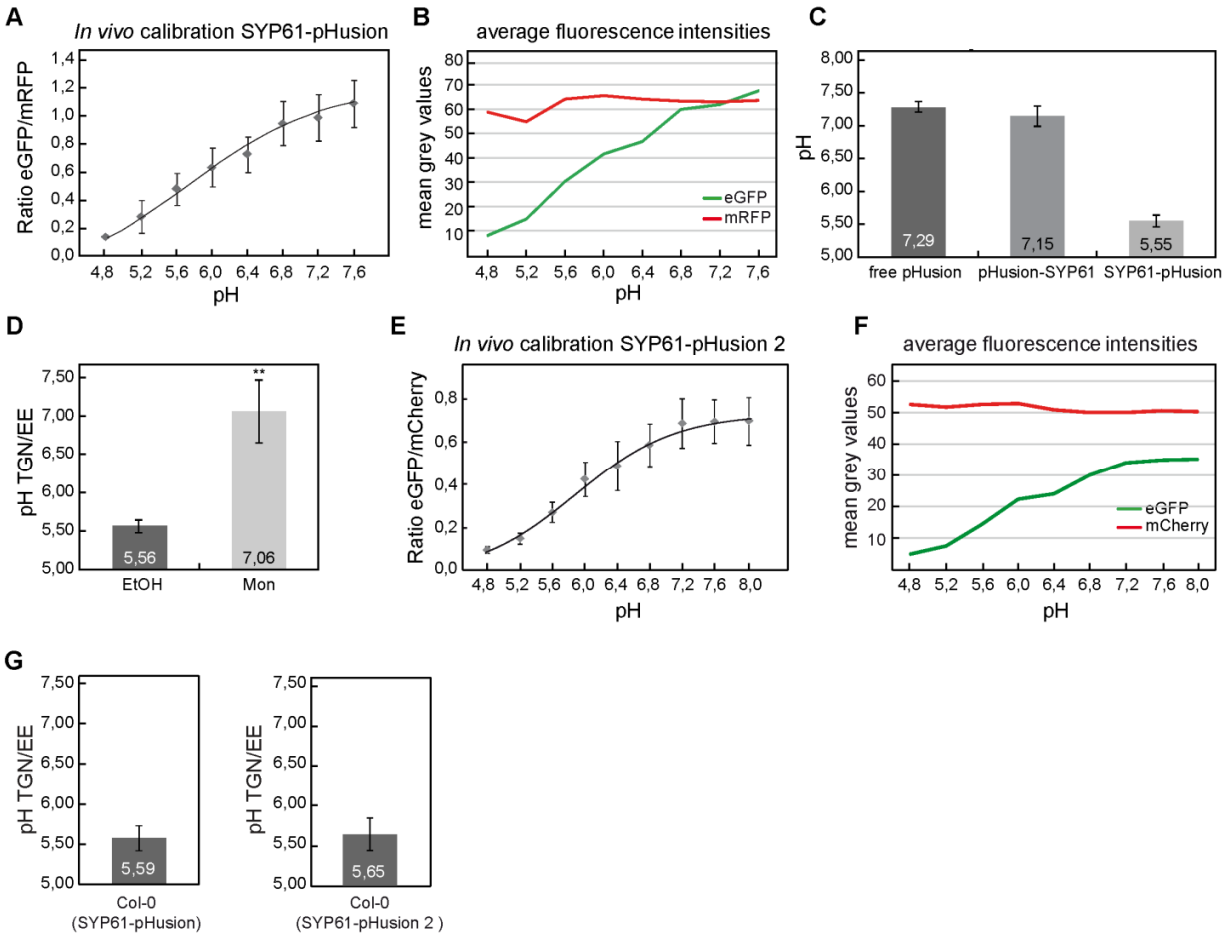

Figure 7: ***In vivo*** **TGN/EE pH measurements using SYP61-pHusion and SYP61-pHusion 2. (A)** *In vivo* calibration curve of P16$_{Pro}$:SYP61-pHusion. eGFP/mRFP intensity ratios are plotted against respective pH equilibration buffer values. Error bars = SD of n=15 seedlings per pH value. **(B)** Fluorescence intensity values of eGFP and mRFP channels of *in vivo* calibration of SYP61-pHusion in (A). **(C)** pHusion is exposed to the acidic TGN/EE lumen in SYP61-pHusion. *In vivo* pH measurements were performed in root epidermal cells of the elongation zone of 6 days old Arabidopsis seedlings. Error bars = SD of n=3 independent measurements with n=15 seedlings, each. **(D)** TGN/EE pH measurement using P16$_{Pro}$:SYP61-pHusion after treatment with 5 µM Monensin (Mon) or equal amounts of EtOH for 30 min. Error bars = SD of n=3 independent measurements with n=15 seedlings, each. Asterisks indicate P-values with *=P<0,05; **=P<0,01; ***=P<0,001, Student´s t-test. **(E)** *In vivo* calibration of UBQ10$_{Pro}$:SYP61-pHusion 2. eGFP/mCherry ratios are plotted against respective pH equilibration buffer values. Error bars = SD of n=15 seedlings per pH value. **(F)** Intensities of eGFP and mCherry single channels of *in vivo* calibration of SYP61-pHusion 2 in (E). **(G)** Identical values for TGN/EE pH were measured using P16$_{Pro}$:SYP61-pHusion and UBQ10$_{Pro}$:SYP61-pHusion 2. Error bars = SD of n=3 independent measurements with n=15 seedlings, each.
Results **(A, C)** are published in Luo et al., 2015.

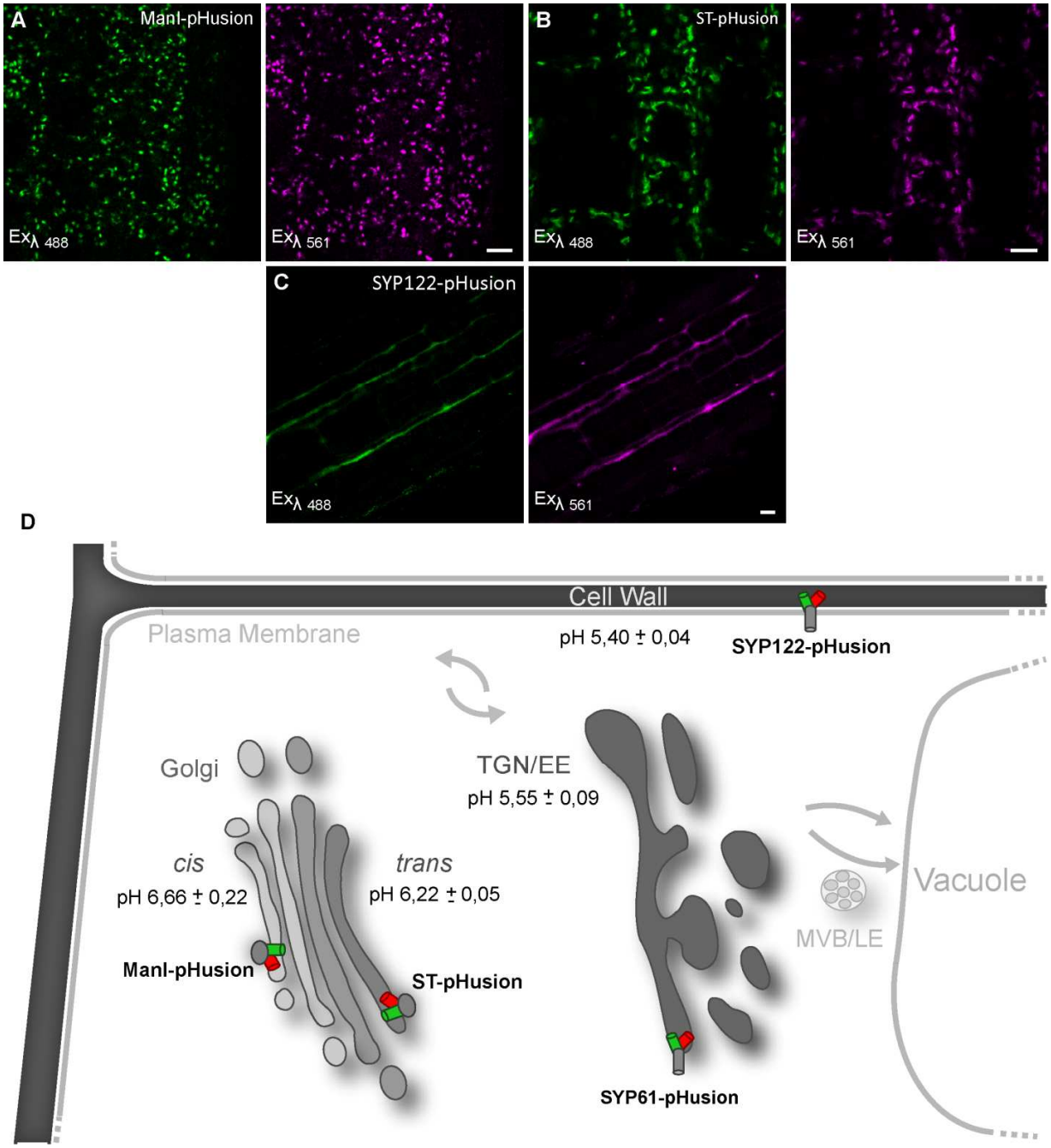

Figure 8: Intracellular pH measurements of secretory pathway organelles and cell wall using pHusion-based pH sensors. All images and *in vivo* pH measurements were performed in root elongation zone cells of stably expressing Arabidopsis lines. **(A)** CLSM images of *cis*-Golgi pH sensor $P16_{Pro}$:ManI-pHusion and **(B)** *trans*-Golgi pH sensor $P16_{Pro}$:ST-pHusion. **(C)** CLSM images of $UBQ10_{Pro}$:SYP122-pHusion as pH sensor for the apoplastic space. **(D)** *In vivo* pH measurement of *cis*-Golgi with $P16_{Pro}$:ManI-pHusion, *trans*-Golgi using $P16_{Pro}$:ST-pHusion and the cell wall (apoplast) using $UBQ10_{Pro}$:SYP122-pHusion. pH values of the TGN/EE correspond to SYP61-pHusion values in Figure 7 C. Error = SD of n=3 independent measurements with n=15 seedlings, each.

2.1.4. The V-ATPase is responsible for TGN/EE acidification

Since the TGN/EE is a major location of the V-ATPase, we next investigated whether the V-ATPase is responsible for acidification of the compartment lumen. For that purpose we monitored TGN/EE pH in epidermal cells of the root elongation zone after 3h treatment with the V-ATPase inhibitor ConcA. A strong alkalisation of the TGN/EE to pH 6,75 was measured upon 3h ConcA treatment (Figure 9 A). Besides pharmacological V-ATPase inhibition, we tested the impact of reduced V-ATPase activity on TGN/EE pH. Thus *$P16_{Pro}$:SYP61-pHusion* was transformed in the *det3* (*de-etiolated 3*) mutant which carries a weak allele of the C-subunit common to all V-ATPases, diminishing V-ATPase activity by 60% (Schumacher et al., 1999). pH in the TGN/EE of *det3* was 0,5 pH units more alkaline compared to WT (*det3*: 6,13; WT: 5,66) (Figure 9 B). Despite the alteration in pH, we did not observe TGN/EE-Golgi hybrids in contrast to ConcA treated cells (Supplementary Figure S3 A-C). Also, localisation of SYP61 was not different to WT in *det3* cells (Supplementary Figure S3 D). To determine whether the VHA-a1-containing V-ATPase is also responsible for acidification of the *trans*-Golgi stack we introduced the *trans*-Golgi pH sensor *$P16_{Pro}$:ST-pHusion* in the *det3* mutant background and performed *in vivo* pH measurements in old 6 days Arabidopsis roots. Localisation of ST-pHusion in *det3* was indistinguishable from wild type (Supplementary Figure S3 E, F) and an average *trans*-Golgi pH of 6,3 was determined for WT and *det3* respectively (Figure 9 C, Supplementary Figure S2 F). These results are in line with preliminary observations that complete V-ATPase inhibition via ConcA does not alter *cis*- or *trans* Golgi pH (Supplementary Figure S3 G).

Since *det3* carries a weak allele of VHA-C subunit leading to reduction of total V-ATPase activity, we tested whether a TGN/EE pH increase can be evoked by a specific knock-down of VHA-a1. Previously, clustered and inflated TGN/EEs due to reduced levels of VHA-a1 were observed in dexamethasone (Dex)-inducible artificial microRNA (amiR) lines against VHA-a1 (Dissertation Dr. Anne Kriegel 2015). Therefore the TGN/EE pH sensor was introduced into the two VHA-a1 knock-down lines by crossing and TGN/EE pH was measured 3 days after Dex induction. We detected a significantly elevated TGN/EE pH relative to WT already in both uninduced amiR-*vha-a1* lines (Figure 9 D, Supplementary Figure S3, H). However, plants did neither display an altered phenotype or growth delays compared to WT and *det3*, nor an altered TGN/EE morphology. amiR-*vha-a1* induction with 30 µM Dex did not increase TGN/EE pH but rather tended to lead to an acidification of the compartment (Figure 9 D).

We confirmed that VHA-a1 containing V-ATPases are responsible for acidification of the TGN/EE but not the Golgi stack in *Arabidopsis thaliana.* However, specific knock-down of VHA-a1 did not incrase TGN/EE pH but appeared to effect an acidification.

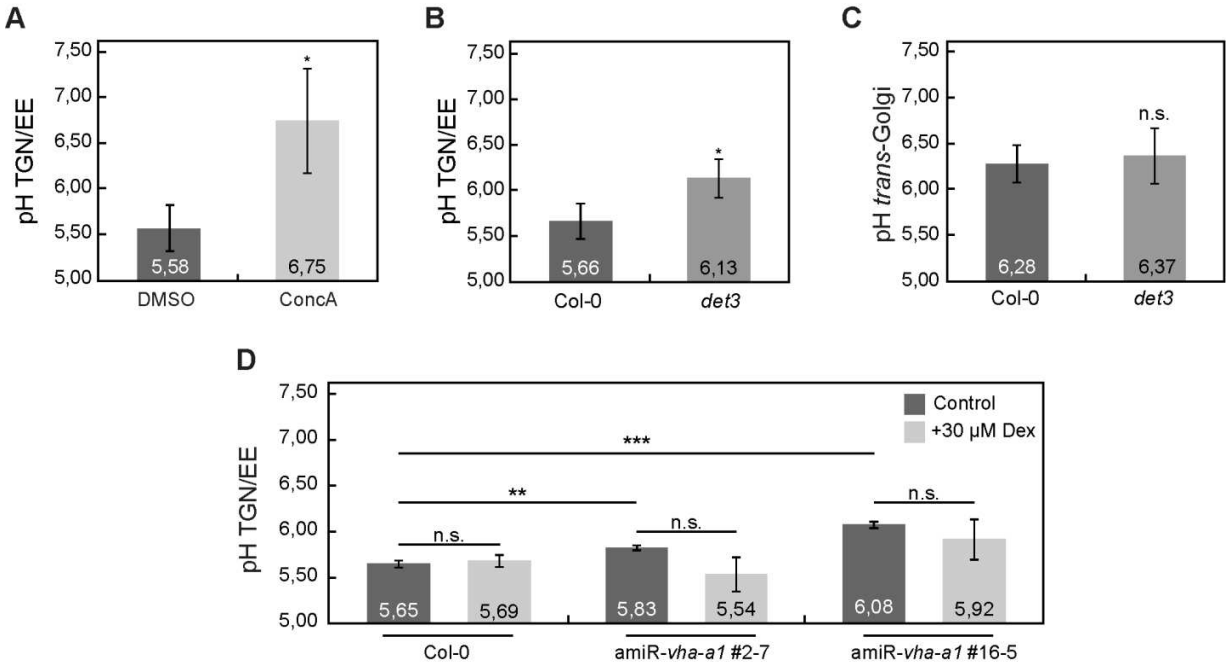

Figure 9: TGN/EE and *trans*-Golgi pH measurements after pharmacological or genetic reduction of V-ATPase activity. pH measurements of the TGN/EE and *trans*-Golgi stack in 6 days old *Arabidopsis thaliana* seedlings. **(A)** TGN/EE pH was alkalised after 3h treatment with 1 µM ConcA but not with equal amounts of DMSO. Measurements were done with plants stably expressing $P16_{Pro}$:SYP61-pHusion. Corresponding calibration curve is shown in Figure 7 A. **(B)** TGN/EE pH measurements in Col-0 or *det3* both stably expressing $P16_{Pro}$:SYP61-pHusion. Calibration curve is depicted in Figure 7 A **(C)** Measurement of the *trans*-Golgi cistern using stably expressed $P16_{Pro}$:ST-pHusion in Col-0 and *det3* background. Corresponding calibration curve is displayed in Supplementary Figure S2 F. **(D)** TGN/EE pH measurements of 7 days old seedlings 72h after Dex induction. Measurements were performed in epidermal cells of the root elongation zone. Error bars = SD of n=3 measurements with n=15 seedlings, each. Asterisks indicate P-values with *=P<0,05; **=P<0,01; ***=P<0,001 or n.s. = P≥ 0,05, P Student´s t-test.
Results in **(A-C)** are published in Luo et al., 2015.

2.1.5. Distribution of pH values for individual TGN/EEs

Data for previous TGN/EE pH measurements were extracted from 3 to 4 cells per image where a large number of individual TGN/EEs were averaged to a final pH value. However, potential pH differences within or between individual TGN/EEs in a cell cannot be assessed by this method. To measure ratios of individual TGN/EEs within single cells, we recorded Z-stacks across root cells of 6 days old seedlings expressing the improved TGN/EE sensor SYP61-pHusion 2. We observed in epidermal cells of the elongation zone a pH gradient across single TGN/EEs (Figure 10 A, B). Thereby it appeared that in each compartment an alkaline and acidic side is present. To test if populations of TGN/EEs with different pH exist, we analysed pH in SYP61-pHusion positive particles. It is crucial to note that SYP61-pHusion positive particles were determined by thresholding and circularity. Therefore a particle can represent a single TGN/EE, a TGN/EE subdomain or a cluster of two or three TGN/EEs. Measurements showed that average pH of the majority of particles ranged around pH 5,6 to 5,7. Moreover, SP61-pHusion positive particles with more acidic pH (pH 5,3 - 4,8) or more alkaline pH than the average (pH 6,0 - 6,5) were detected as well (Supplementary Figure S4). When followed over consecutive Z-stack slices, homotypic fusion events of two or more TGN/EE were observed as reported earlier (Viotti et al., 2010). Concomitant with contact sides between two compartments or at membrane fission events, a strong alkalisation close to the surface of a TGN/EE seemed to be present (Figure 10 C, D). However, whether membrane fission events correspond to vesicle formation cannot be stated certainly. In conclusion, we provided evidence that a pH gradient is present in TGN/EEs which forms alkaline and acidic compartment sides or subdomains.

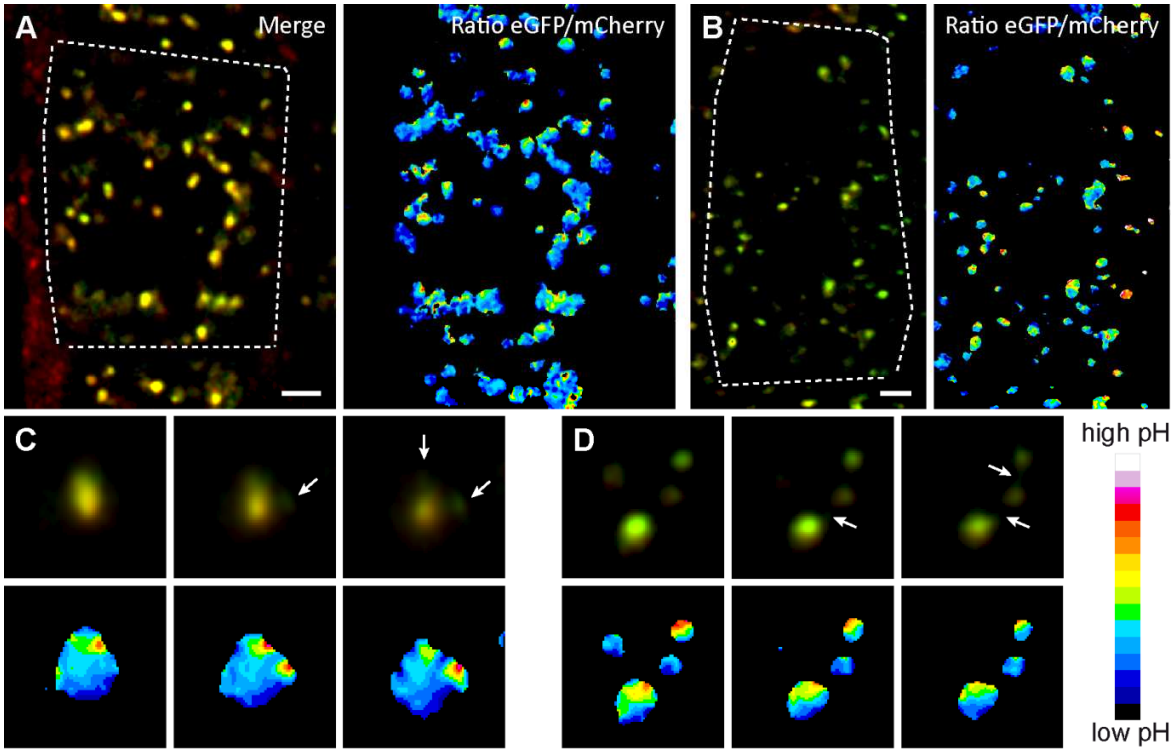

Figure 10: CLSM of single root cells expressing SYP61-pHusion 2. Images were recorded in elongation zones of 6 days old Arabidopsis seedlings with a Zeiss LSM800 in "Fast Airyscan" projections. **(A), (B)** Representative merge images of $UBQ10_{Pro}$:SYP61-pHusion 2 (green=eGFP, red=mCherry) and corresponding eGFP/mCherry ratio images. Dashed lines mark cell outlines. **(C)**, **(D)** Magnified, consecutive Z-stack images of a single TGN/EE. Arrows point to contact sites of homotypic fusions between two TGN/EEs. Note ratio increase at membrane surface at TGN/EE contact sites. Similar observations were made in cells of 5 different roots. Bars = 2,5 µm.

2.2. Contribution of the TGN/EE to vacuolar acidification

The TGN/EE contributes to vacuolar acidification either by proton transport via three TGN/EE-to-vacuole transport routes (Kriegel et al., 2015). Furthermore, a communication between the vacuolar and the TGN/EE V-ATPase pool was proposed (Dissertation Dr. Anne Kriegel 2015). Due to the fact that we detected more alkaline TGN/EEs in *det3* we tested whether vacuolar pH is altered as well. Using the pH sensitive dye BCECF (2',7'-bis(2-carboxyethyl)-5(6)-carboxyfluorescein) which accumulates in plant vacuoles (Swanson and Jones, 1996; Krebs et al., 2010) we determined an average vacuolar pH of 5,82 in *det3* which did not differ significantly from WT (pH 5,91) (Figure 11 A, Supplementary Figure S5 A). In contrast, vacuolar pH was more alkaline in *vha-a2 vha-a3* lacking both tonoplastic V-ATPases (Krebs et al., 2010). Subsequently, we investigated whether in plants lacking both tonoplastic V-ATPases, activity of

the TGN/EE-localised V-ATPase is altered as part of an possible compensation mechanism. For that purpose *P16$_{Pro}$:SYP61-pHusion* was introduced in *vha-a2 vha-a3* via crossing and *in vivo* TGN/EE pH was monitored. Yet, a TGN/EE pH of 5,54 was determined in *vha-a2 vha-a3* (Figure 11 B, Supplementary Figure S5 B) corresponding to results in Col-0.

To further study proton transport from the TGN/EE to vacuole, we determined vacuolar pH in a mutant interfering with the multivesicular bodies/late endosomal (MVB/LE) pathway. We did not observe an altered vacuolar pH in *sand1-1* (*sand1-1* pH 5,92; Col-0 pH 5,83) which lacks a component required for endosomal maturation (Singh et al., 2014) (Figure 11 C; Supplementary Figure S5, C). We next employed the dominant-negative *wat1-1D (weak-acid tolerant 1-1D)* which overexpresses a truncated form of the ß-subunit of the Arabidopsis AP-3 complex (Niñoles et al., 2013). Besides, vacuolar pH was measured in the *pat2-2 (protein affected trafficking 2-2*) mutant representing a full knock-out of AP-3 ß-subunit due to a T-DNA insertion in the same gene (Feraru et al., 2010). Interestingly, vacuolar pH was significantly increased in *pat2-2* by 0,2 pH units compared to WT (WT = 5,67 *pat2-2* = 5,86) whereas an identical but not significant pH difference was measured in *wat1-1D* (*wat1-1D* = 5,87) (Figure 11 D; Supplementary Figure S5 D). Subsequently, we tested if vacuolar pH of AP-3 mutants can be further increased by inhibition of the MVB/LE pathway. After treatment with the phosphatidylinositol 3-kinase inhibitor (PI3K) LY294002 causing MVB/LE to aggregate (Lee et al. 2008, Jung et al. 2002), no change in vacuolar pH compared to DMSO controls was detected in Col-0 and in both AP-3 mutants (Figure 11 D). We finally measured vacuolar pH in *hapless13* (*hap 13*) and *ap1m2-1* (Park et al. 2013) mutants, both carrying a T-DNA insertion in the gene encoding the µ-subunit of AP-1. Here, vacuolar pH of *hap 13* was 0,2 pH units more acidic than WT (*hap13* = 5,61, WT Col-0= 5,99) or decreased by 0,3 pH units in *ap1m2-1* (*ap1m2-1* = 5,72, WT = 6,01) (Figure 11 E). In conclusion we measured an altered vacuolar pH in mutants with alterations in AP-3 and AP-1 dependent clathrin-coated vesicle pathways. Interestingly, pH was either increased by approximately 0,2 pH units in AP-3 mutants or decreased by 0,2 pH units in mutants with alterations in AP-1 complexes. However, we did not observe an altered vacuolar pH in *sand1-1* or after LY294002 treatment of WT and both AP-3 mutants.

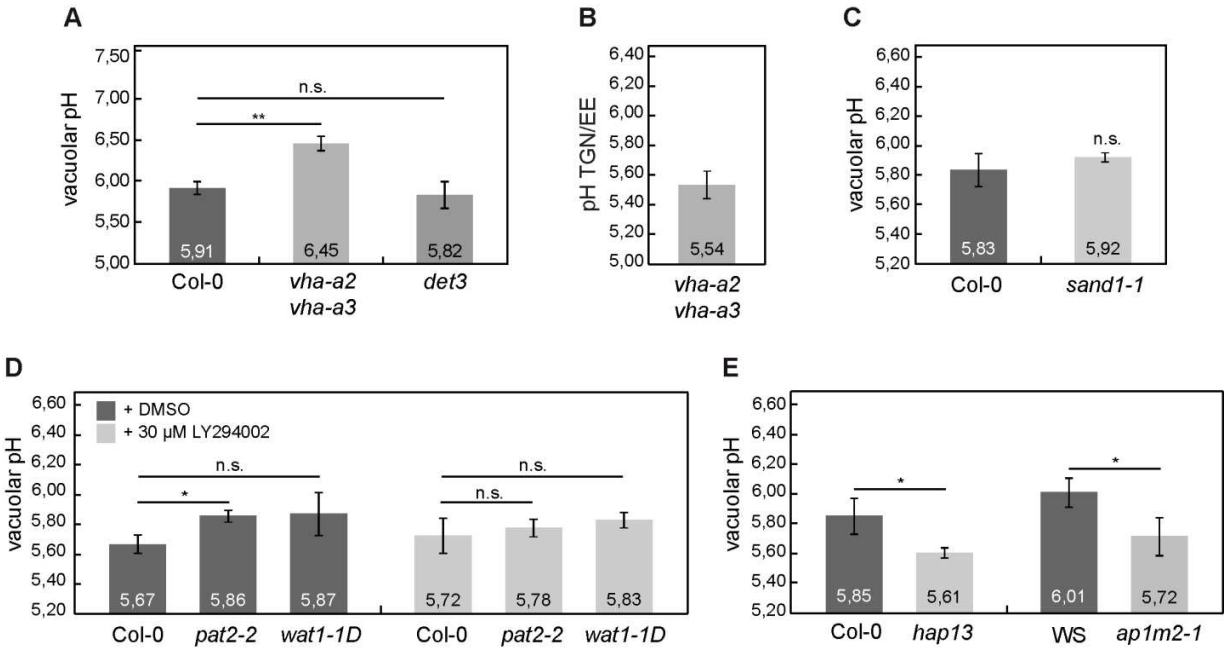

Figure 11: The TGN/EE contributes to vacuolar acidification via clathrin coated vesicle routes. TGN/EE and vacuolar pH measurements of 6 days old *Arabidopsis thaliana* seedlings. Data for TGN/EE pH was taken in root elongation zones, all vacuolar pH measurements were done in epidermis and cortex cells of the root differentiation zone. **(A)** Vacuolar pH measurements via BCECF in 6 days old seedling roots of Col-0, *vha-a2 vha-a3* and *det3*. **(B)** TGN/EE pH measurements in *vha-a2 vha-a3* stably expressing $P16_{Pro}$:SYP61-pHusion. **(C)** Vacuolar pH measurements in WT or *sand 1-1* using BCECF. Corresponding calibration curve is shown in Supplementary Figure S5 B **(D)** Vacuolar pH of AP-3 mutants *pat2-2* or *wat 1-1D* at DMSO- or 30 µM LY 294002 treatment for 1h. For calibration curve see: Supplementary Figure S5 C. **(E)** Vacuolar pH measurements of AP-1 mutants *hap13* and *ap1m2-1* and corresponding WT controls. Error bars = SD of n=3 independent measurements with n=15 seedlings, each. Asterisks indicate P-values with *=P<0,05; **=P<0,01; ***=P<0,001 or n.s. = P≥ 0,05, P Student´s t-test.

Results in **(A)** are published in Luo et al. 2015.

2.3 pH homeostasis of the TGN/EE

We recorded a steady state pH of the TGN/EE of on average pH 5,6 which is generated by VHA-a1-containing V-ATPases. In addition, we showed that TGN/EE acidification is crucial for functional intracellular trafficking (Luo et al., 2015) and hence needs to be kept on homeostatic levels. The NHX5 NHX6 K^+/H^+ exchangers at the TGN/EE (Bassil et al., 2011a) have been proposed to serve not only in luminal K^+- but also pH homeostasis (Reguera et al., 2015). We therefore introduced *P16$_{Pro}$:SYP61-pHusion* the *nhx5 nhx6* background. An average TGN/EE pH of 4,94 (WT = 5,46) was measured showing that NHX5 and NHX6 co-determine TGN/EE pH (Figure 12).

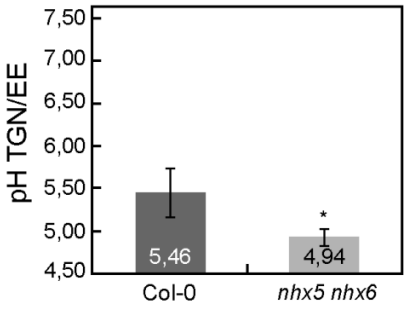

Figure 12: *nhx5 nhx6* contains more acidic TGN/EEs. TGN/EE pH measurements in Col-0 or *nhx5 nhx6* using in 6 days old *Arabidopsis thaliana* seedlings expressing P16$_{Pro}$:SYP61-pHusion. Error bars = SD of n=4 independent measurements with n=15 seedlings, each. asterisks indicate P-values with *=P<0,05; **=P<0,01; ***=P<0,001 or n.s. = P≥ 0,05 Student´s t-test.

The average TGN/EE pH of 5,0 in *nhx5 nhx6* also illustrated that the V-ATPase is able to generate a steeper pH gradient than in the WT steady state. Due to the electrogenecity of the V-ATPase, counterbalance of the positive charge imported in form of protons (H^+) is a prerequisite to make luminal acidification possible. The TGN/EE-localised, putative anion/H^+ antiporter ClCd has been proposed to provide the shunt conductance for the V-ATPase (von der Fecht-Bartenbach et al., 2007). Nevertheless, ClCd single mutants do not display a phenotype under standard growth conditions which proposes functional redundancy. Marmagne et al. reported that the plant ClC-family member ClCf (At1g55620) is located at Golgi stacks in transiently expressing onion epidermal cells. We therefore included ClCd and the uncharacterised ClCf into our studies and monitored whether both ClC-family proteins have a role in supporting the V-ATPase in TGN/EE acidification and pH homeostasis.

2.3.1. ClCf is mainly located at the TGN/EE in *Arabidopsis thaliana*

To investigate *in vivo* localisation of ClCf, we linked the full length *ClCf* coding sequence to mRFP and overexpressed *ClCf-mRFP* via the constitutive UBQ10 promoter (Norris et al., 1993). In stable expressing Arabidopsis lines, ClCf-mRFP yielded a motile punctate signal pattern which strongly overlapped with VHA-a1-GFP at the TGN/EE (Figure 13 A). Quantification of co-localisation resulted in a high degree of co-localisation between both proteins (Supplementary Figure S6 A-C). Subsequently, we screened whether ClCf is located also at other compartments. Treatment with the PI3K inhibitor Wortmannin (Tse, 2004) did not alter ClCf-mRFP signals (Figure 13 B) excluding that ClCf is present at MVB/LEs. Contrary to published data (Marmagne et al., 2007), we only observed partial co-localisation of ClCf-mRFP with the *trans*-Golgi marker ST-GFP in co-expressing lines (Figure 13 C, Supplementary Figure S6 D, E). Ultimately, we saw strong co-localisation between ClCf-mRFP and ClCd-GFP (Figure 13 D). Via immunogold-labelling of high pressure frozen and freeze substituted seedlings expressing ClCf-mRFP, we detected the majority of gold particles at the TGN/EE (Supplementary Figure S6 F). Altogether our results demonstrated that ClCf is mainly located at the TGN/EE and displays a localisation identical to ClCd.

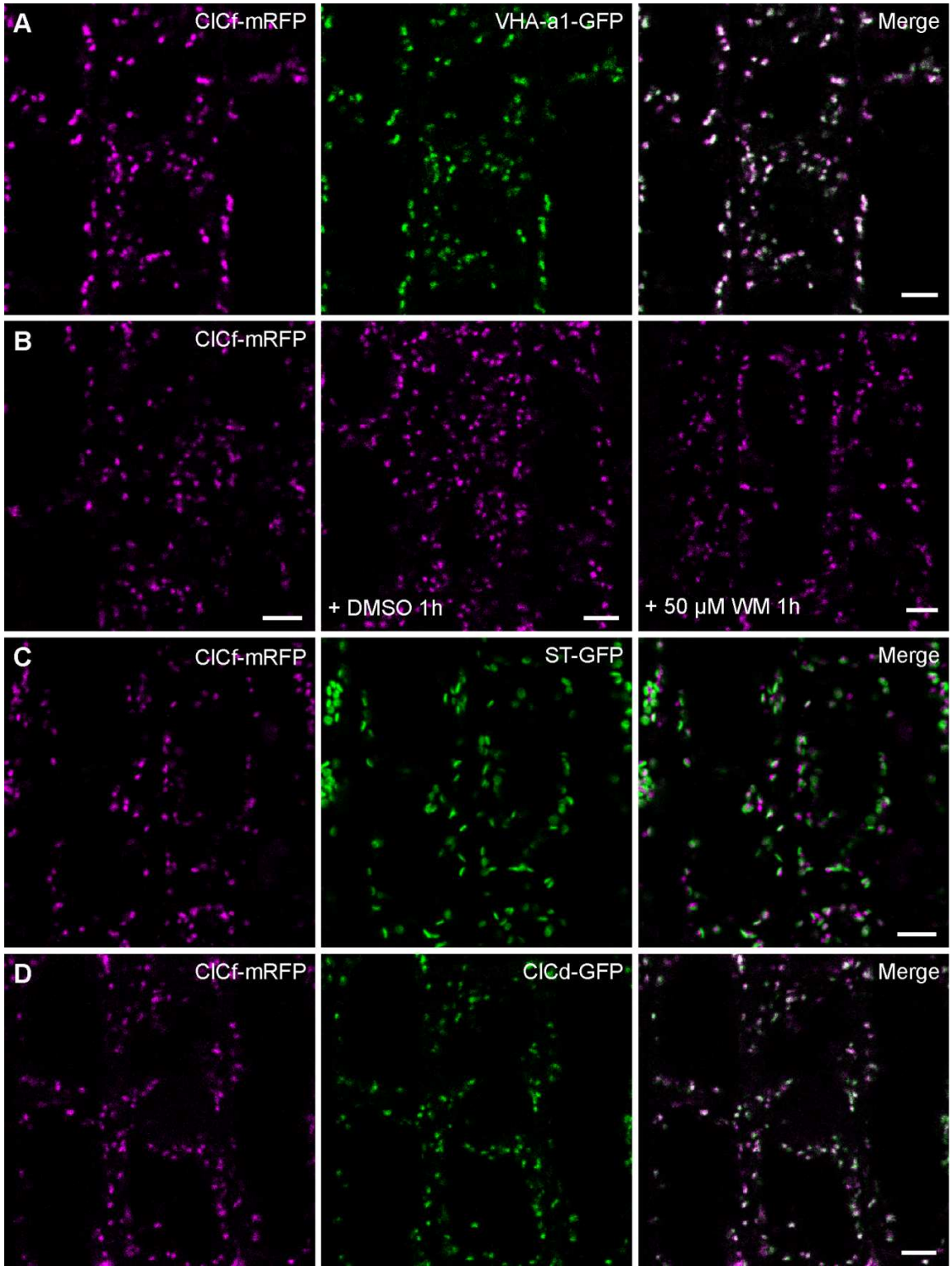

Figure 13: ClCf is mainly located at the TGN/EE. Images were taken in root elongation zone cells of 6 days old Arabidopsis seedlings. **(A)** ClCf-RFP co-localises with the TGN/EE marker VHA-a1-GFP **(B)** ClCf-mRFP localises to dot-like, motile structures that did not change after 1h of DMSO or 50 µM Wortmannin (WM) treatment. **(C)** ClCf-mRFP overlaps to a minor extend with the *trans*-Golgi marker ST-GFP.

Figure 13 (continued)

(D) High co-localisation is present when ClCf-RFP is co-expressed with ClCd-GFP. Bars=5 µm.

2.3.2. ClCf and ClCd are hypersensitive to Concanamycin A

To investigate the *in vivo* roles of ClCf, we employed a homozygous T-DNA insertion line from the SALK collection (SALK_112962). PCR-based genotyping and sequencing confirmed a T-DNA insertion in intron 6 of *ClCf*. The T-DNA insertion caused truncation of *ClCf* transcript by which exon 7 and 8 are eliminated (Figure 14 A). However, as *clcd* knock-outs, *clcf* plants did not show phenotypes under standard growth conditions (Figure 14 B).

clcd knock-outs were reduced in hypocotyl elongation after ConcA-mediated V-ATPase inhibition (von der Fecht-Bartenbach et al., 2007). To test if *clcf* displays identical hypersensitivity to ConcA, we measured hypocotyl length of etiolated seedlings in presence of ConcA. We verified that hypocotyls of *clcf* and *clcd* were 15% shorter than WT when grown on 100 µM ConcA whereas on control medium all genotypes depicted comparable hypocotyl length (Figure 14 C; Supplementary Figure S7 A). Hypersensitivity of *clcf* could partially be complemented by overexpression of ClCf-mRFP in the *clcf* background by the UBQ10 promoter (Figure 14 C). However, reported root growth defects of *clcd* on alkaline medium (von der Fecht-Bartenbach et al., 2007) could not be confirmed and were not observed for clcf as well (Supplementary Figure S7 B).

ClCd was proposed to provide counterions for V-ATPase-mediated acidification of the TGN/EE (von der Fecht-Bartenbach et al., 2007). To determine whether steady state TGN/EE pH of *clcd* or *clcf* is altered, we monitored compartment pH in both single knock-out lines stably expressing SYP61-pHusion. After *in vivo* calibration and three independent measurements, an average TGN/EE pH of 5,50 for *clcd* and pH 5,61 for *clcf* (Figure 14 D; Supplementary Figure S8 A, B) was determined which corresponded values measured in Col-0. We confirmed that ClCf single mutants are hypersensitive to ConcA identically to *clcd* and that hypersensitivity is caused by a *ClCf* knock-out. This hypocotyl shortening at ConcA presence could be complemented by insertion of the full length coding sequence of ClCf tagged with mRFP in *clcf*. Nevertheless, steady state TGN/EE pH of both *clcd* and *clcf* was not affected.

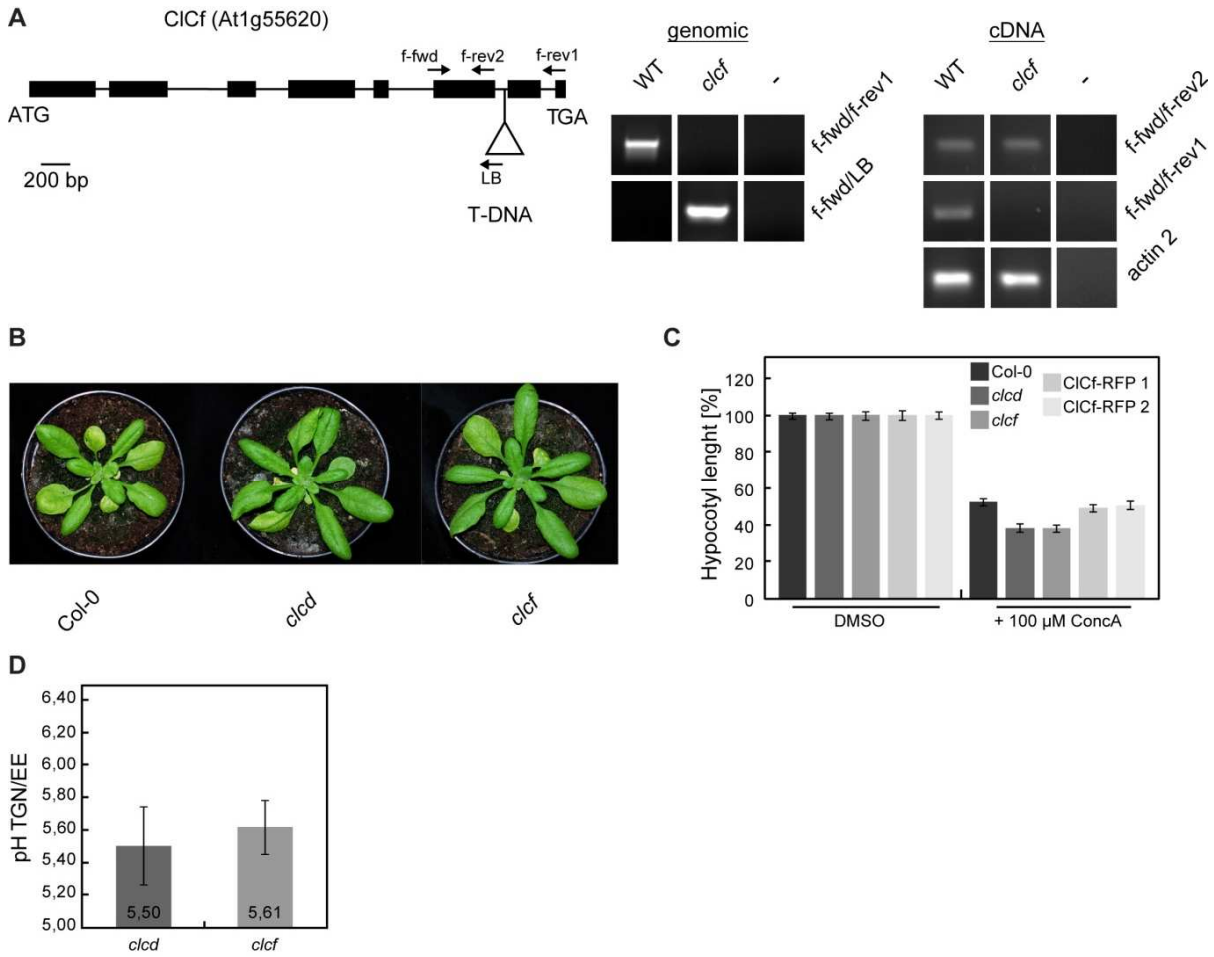

Figure 14: *clcf* is hypersensitive to Concanamycin A. (A) Schematic overview over the *ClCf* sequence. Exons are indicated as black boxes, introns as black lines. Arrows = primers used for genotyping of the T-DNA insertion in *ClCf* (SALK_112962) using genomic DNA (gDNA) or cDNA as template. **(B)** Images of WT Col-0, *clcd* and *clcf* 20 days after stratification and growth at long day conditions (16h light/8h dark cycles). **(C)** Hypocotyl length measurements of 5 days old etiolated seedlings grown on 1% phytoagar, 5 mM MES-KOH (pH 5,8) supplied with 1µM ConcA or DMSO. Representative results of at least 3 independent repetitions. Error bars=SE of n=30 hypocotyls for each sample. **(D)** TGN/EE pH measurements in *clcd* and *clcf*. Measurements were done with plants stably expressing $P16_{Pro}$:SYP61-pHusion and after *in vivo* calibration of each sensor line. Error bars = SD of n=3 independent measurements with n=15 seedlings, each.

2.3.3. ClCf does not interact with ClCd and VHA-a1-containing V-ATPases

All ClCs from pro- to eukaryotes form homodimers (Accardi, 2015). To further characterise both TGN/EE-localised ClCs, we investigated whether ClCf and ClCd are able to form heterodimers or interact directly. As ClCf has been shown to be hypersensitive to ConcA, which proposes that ClCf and the TGN/EE-localised V-ATPase function in similar pathways, we additionally tested for

interaction of ClCf with VHA-a1. We conducted *in vivo* FLIM-FRET measurements using 6 days old Arabidopsis seedlings expressing ClCf-mRFP as FRET acceptor together with ClCd-GFP or VHA-a1-GFP as FRET donors. pHusion-SYP61 was used as FLIM-FRET positive control in both experiments. All measurements were performed in root elongation- and transition zones of 6 days old seedlings. However, we did not observe a GFP lifetime change between ClCd-GFP and co-expression of ClCf-mRFP with ClCd-GFP (Figure 15 A). Thus no direct interaction between both TGN/EE-localised ClC-transporters could be detected via FLIM-FRET. Identical values were determined with VHA-a1-GFP as FRET-donor (Figure 15 B) and therefore a direct interaction of ClCf with VHA-a1 containing V-ATPases was excluded using this method.

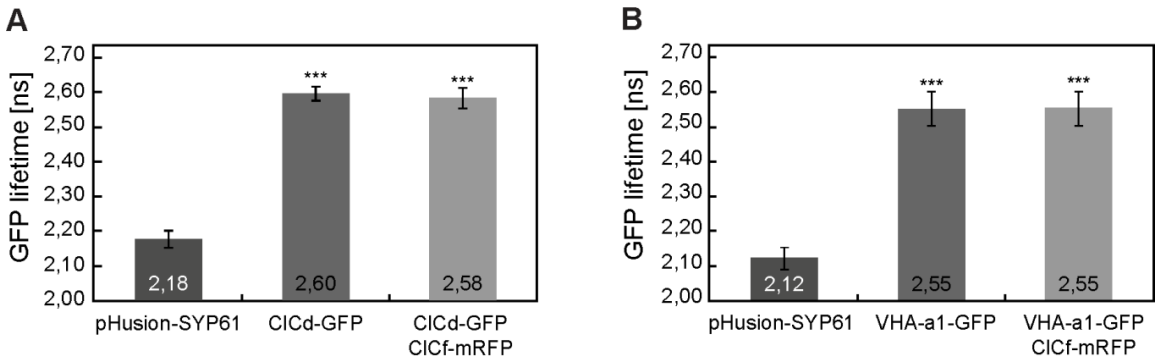

Figure 15: ClCf does not interact with ClCd or V-ATPase subunit VHA-a1. (A) GFP fluorescence lifetime measurements in Arabidopsis lines stably expressing $P16_{Pro}$:pHusion-SYP61, $UBQ10_{Pro}$:ClCd-GFP or co-expressing $UBQ10_{Pro}$:ClCd-GFP and $UBQ10_{Pro}$:ClCf-mRFP. **(B)** GFP fluorescence lifetime measurements in Arabidopsis lines stably expressing $P16_{Pro}$:pHusion-SYP61, $UBQ10_{Pro}$:ClCd-GFP or co-expressing $UBQ10_{Pro}$:ClCd-GFP and $UBQ10_{Pro}$:ClCf-mRFP. Error bars = SD of n=3 independent measurements with n=15 seedlings, each. Asterisks indicate P-values relative to positive controls with *=P<0,05; **=P<0,01; ***=P<0,001 or n.s. = P≥ 0,05, Student´s t-test.
FLIM-FRET measurements in **(B)** were performed by Franziska Lesche.

2.3.4. TGN/EE-localised anion transporters ClCf and ClCd are essential

Except for a ConcA-dependent hypocotyl length reduction, both ClCd and ClCf single mutants did not display alterations in growth, organ size or TGN/EE pH. To monitor effects of a total loss of endosomal ClC transporters, we generated a *clcd clcf* double mutant by crossing both T-DNA insertion lines. In mature siliques (approximately 14 days after fertilisation) of *clcd*/+ *clcf* and *clcf clcd*/+ parent plants, we identified roughly 25% aborted seeds or degenerated ovules (Figure 16 A; Supplementary Figure S8, C). Since we would expect homozygous *clcd clcf* in one quarter of the offspring, results suggested lethality of a double knock-out.

We subsequently performed reciprocal crosses of *clcd clcf*/+ with Col-0 to test whether mutations affected gametophyte development. Via genotyping of F_1 offspring of *clcd clcf*/+ crossed with Col-0, we detected the segregating T-DNA in approximately 33% of the plants when *clcd clcf*/+ was used as pollen receiver. However, when *clcd clcf*/+ was used as pollen donor, the respective T-DNA was present in only 2% of the offspring (Figure 16 B). Approximately 1 out of 50 plants were *clcd clcf* double mutants but seedlings did not survive after transfer to soil and could never be recovered. By introduction of the *$UBQ10_{Pro}$:ClCf-mRFP* construct we were able to rescue a *clcd clcf* mutant. Nevertheless, plants were reduced in growth compared to WT and the respective overexpression lines probably caused by the C-terminal tag (Supplementary Figure S8, D). In conclusion, we showed that the TGN/EE-localised ClCd and ClCf transporters are essential and that a lack of both ClCs causes male gametophyte lethality.

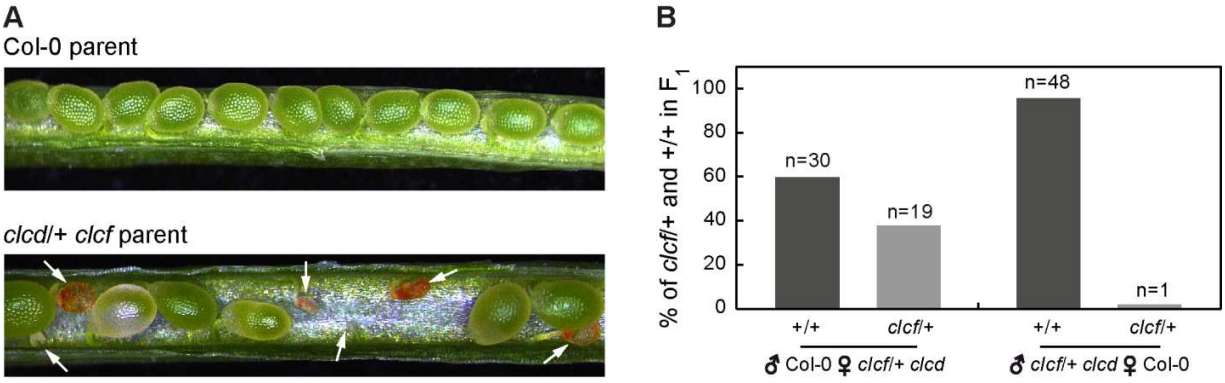

Figure 16: A ClCd and ClCf double knock out leads to male gametophyte lethality. (A) Opened, mature siliques of WT or *clcd*/+ *clcf* with aborted or degenerated ovules (arrows). **(E)** In reciprocal crosses of *clcf clcd*/+ with Col-0, the segregating T-DNA in the *clcf* allele could not be detected when *clcf clcd*/+ was used as pollen donor. 2/3 of the F_1 offspring carried a *ClCf* T-DNA insertion when *clcf clcd*/+ was pollen receiver. n=50 plants were analysed for each cross.

2.3.5. Generation of a knock-down against ClCd and ClCf

Despite lethality of a *clcd clcf* mutant, *in vivo* functions can be studied via targeted knock-down of one or both genes. Since both ClC sequences were too distinct to generate one knock-down construct for both genes, an artificial micro RNA (amiR) against *ClCf* was constructed using the Web MicroRNA Designer (www.weigelworld.de) and put under control of the 6xOP dexamethasone (Dex)-inducible promoter/LhGR system (Craft et al., 2005). The final amiR construct (Figure 17 A) was introduced into the *clcd* background and two independent

homozygous lines were established. Induction of the amiR by 72h treatment with 60 µM Dex reduced ClCf protein levels to approximately 50% in *clcd* amiR-*clcf* 1 (Figure 17 B, C) or less than 5% (3,9%) in *clcd* amiR-*clcf* 2 (Figure 17 D, E) using ClCf-mRFP as reporter which was targeted by the amiR. Finally, reduction in ClCf levels was repressed by mutating the amiR recognition site in the ClCf ORF depicting that protein reduction is specifically caused by the introduced amiR targeting *clcf* (Supplementary Figure S9).

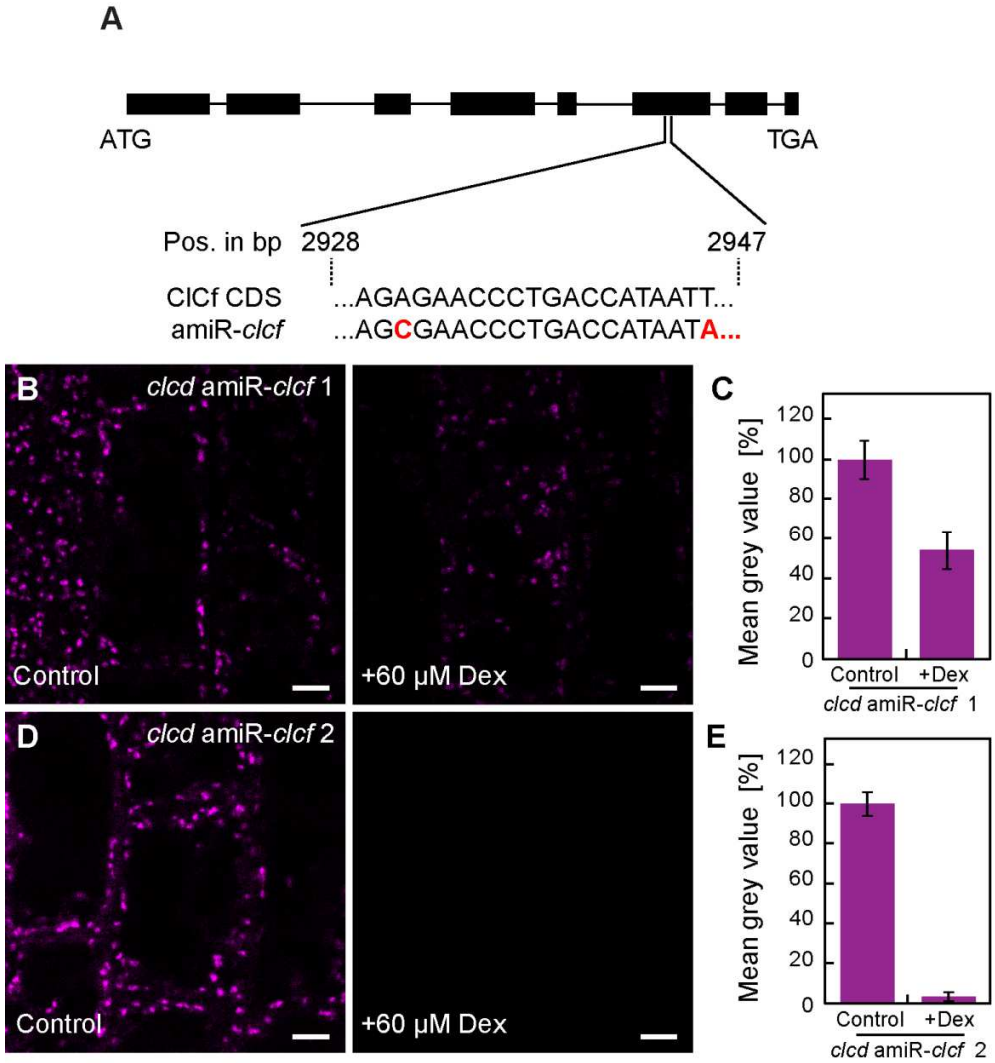

Figure 17: Generation of an artificial micro RNA against ClCf. (A) Schematic overview over the ClCf coding sequence and the binding site of an artificial micro RNA targeted against *ClCf*. Bases highlighted in red are altered in the amiR sequence compared to WT *ClCf* sequence. Exons are indicated as black boxes, introns as black bars. **(B)** $UBQ10_{Pro}$:ClCf-mRFP in *clcd* amiR-*clcf* 1 after 72h control or 60 µM Dex treatment. **(C)** Quantification of ClCf-mRFP fluorescence in *clcd* amiR-*clcf* 1 after 72h control or 60 µM Dex (Dex) treatment. Error bars= standard deviation of n=3 independent measurements with n=15 seedlings, each. **(D)** $UBQ10_{Pro}$:ClCf-mRFP in *clcd* amiR-*clcf* 2 after 72h

Figure 17 (continued)

(E) Quantification of ClCf-mRFP fluorescence in *clcd* amiR-*clcf* 2 after 72h control or 60 µM Dex (Dex) treatment. Error bars= standard deviation of n=3 independent measurements with n=15 seedlings, each. Bars= 5 µm.

2.3.6. ClCd and ClCf are required for cell elongation

Hypocotyl length of *clcd* and *clcf* were reduced upon co-inhibition of the V-ATPase via ConcA. To test if cell elongation is affected in both *clcd* amiR-*clcf* knock-down lines we measured hypocotyl length of etiolated seedlings and root length of light grown plants. Upon Dex induction, hypocotyl length of *clcd* amiR-*clcf* 1 was reduced by approximately 80% and length of *clcd* amiR-*clcf* 2 hypocotyls was diminished up to 49% compared to WT (Figure 18 A Supplementary Figure S10 A). Thereby reduction in hypocotyl length correlated with the degree of ClCf protein reduction. Similar to hypocotyls, root length was diminished by approximately 85% in *clcd* amiR-*clcf* 1 lines and by around 50% in *clcd* amiR-*clcf* 2 (Figure 18 B). In both hypocotyl- and root length measurements, growth of WT or *clcd* was not inhibited by Dex. Interestingly, hypocotyl and root length of both *clcd* amiR-*clcf* lines was larger than WT and *clcd* in the uninduced state (Supplementary Figure S10 A, B).

We subsequently looked at root tip architecture of *clcd* amiR-*clcf* to determine whether alterations in shape and size were visible. Whereas uninduced roots of 7 days old plants did not display any phenotype compared to WT (Figure 18 C, D, E), we observed stunted cells in the elongation- and differentiation zone as well as non elongated root hairs in both induced *clcd* amiR-*clcf* lines. However, meristematic zones were not altered in overall morphology (Figure 18 F, G, H). Measurement of root zones confirmed a Dex-dependent size reduction of elongation zones in both *clcd* amiR-*clcf* lines and a shorter meristematic zone in *clcd* amiR-*clcf* 2 (Figure 18 I, J, K; Supplementary Figure S10 C-K). Altogether, these results indicated a role of ClCd and ClCf in cell elongation, similar to the TGN/EE-localised V-ATPase.

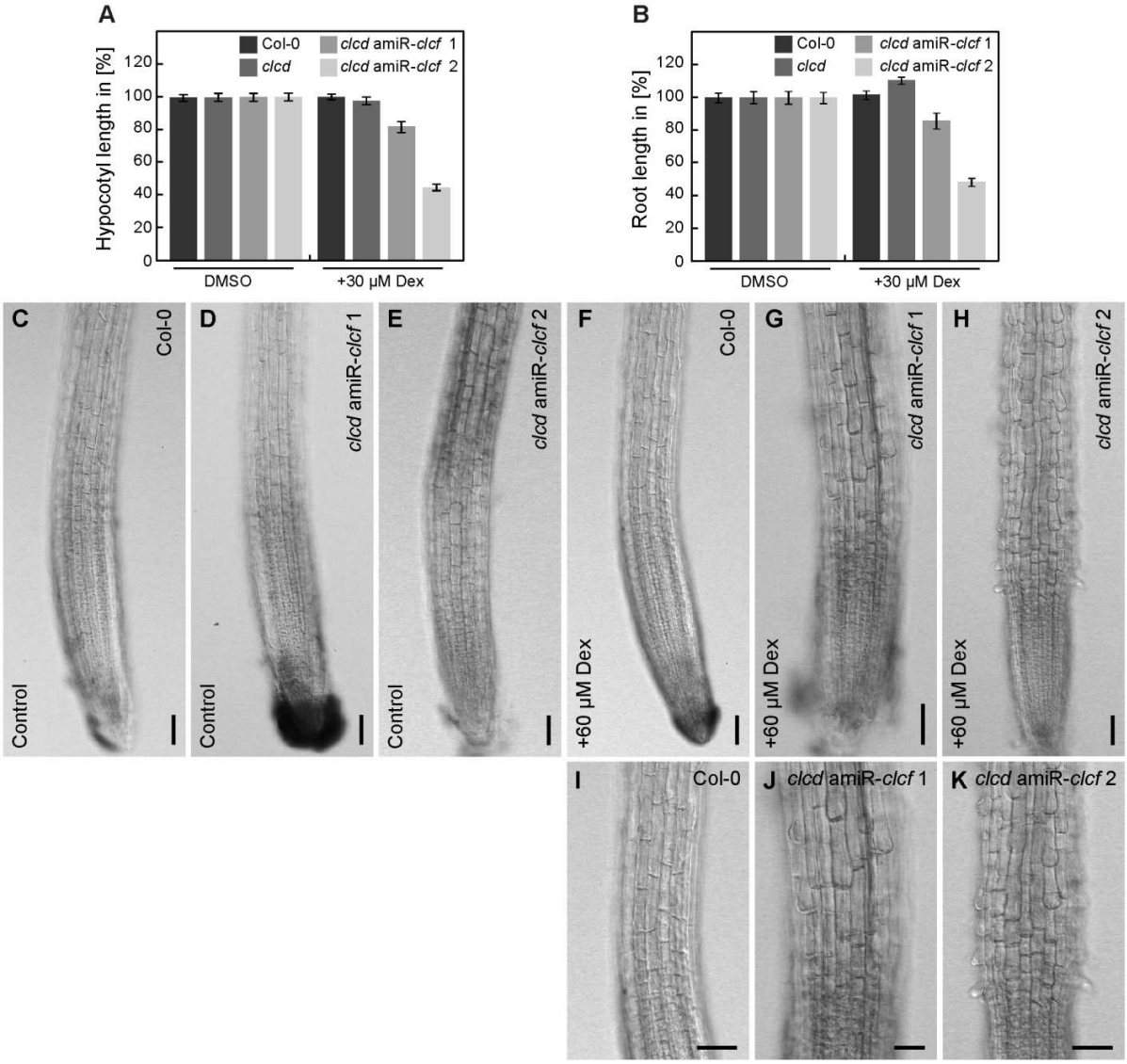

Figure 18: ClCd and ClCf are required for cell elongation. (A) Hypocotyl length measurements of 5 days old etiolated seedlings grown on H_2O, 5 mM MES-KOH (pH 5,8) supplied with 30 µM Dex or DMSO. Representative results of at least 3 independent repetitions. Error bars = SE of n=30 hypocotyls for each sample. **(B)** Root length of 7 days old seedlings grown on 1/2 MS, pH 5,8, 1% phytoagar at long day conditions. Plates were supplied with 30 µM Dex or equal amounts of DMSO. Error bars = SE of n=30 roots for each sample. **(C)** Overview of root tip of WT, **(D)** *clcd* amiR-*clcf* 1 or **(E)** *clcd* amiR-*clcf* 2 72h after transfer to 1/2 MS medium or **(F)** Col-0, **(G)** *clcd* amiR-*clcf* 1 and **(H)** *clcd* amiR-*clcf* 2 72h after transfer to 1/2 MS medium plus 60 µM Dex. Magnification of Dex-treated roots of **(I)** WT Col-0, **(J)** *clcd* amiR-*clcf* 1 or **(E)** *clcd* amiR-*clcf* 2. Bars = 50 µm.

2.3.7. Knock-downs of ClCf in *clcd* do not show an altered TGN/EE pH

TGN/EE pH of ClCd and ClCf single mutants was not altered. To answer whether a knock-down of *ClCf* in *clcd* has influences on the TGN/EE pH, we measured TGN/EE pH of the strong *clcd* amiR-*clcf* 2 (compare: Figure 17 E) using $UBQ10_{Pro}$:SYP61-pHusion 2 (Figure 19 A, B). Since ClCf and ClCd partially co-localised with the *trans*-Golgi marker ST, we also determined *trans*-Golgi pH using ST-pHusion (Figure 19 C, D). *In vivo* pH measurements were done in 7 days old seedling roots grown on John`s medium devoid of chloride (Cl^-) and nitrate (NO_3^-) (von der Fecht-Bartenbach et al., 2007). Calibrations were conducted in every genetic background to exclude possible quenching effects of Cl^- on pHusion 2 (Supplementary Figure S11 A-F). However, TGN/EE pH was neither altered in induced or uninduced *clcd* amiR-*clcf* plants compared to WT or *clcd* (Figure 19 E; Supplementary Figure S11 G). Surprisingly, pH of the *trans*-Golgi was approximately 0,6 pH units lower in induced *clcd* amiR-*clcf* 2 lines, whereas pH of uninduced *clcd* amiR-*clcf* was similar to *clcd* or WT (Figure 19 F; Supplementary Figure S11 H). To monitor if a lack of ClCf in *clcd* only altered pH of a TGN/EE subpopulation, we measured pH in particles positive for SYP61-pHusion 2. However, distribution of pH values in individual TGN/EEs, subdomains or cluster was not different compared to WT (Figure 19 G). Most values ranged between pH 5,4 to 5,6 with alkaline (up to pH 6,0) and acidic particles of approximately pH 5,0 (Figure 19 G) in all genotypes and conditions. In conclusion, we observed that *trans*-Golgi but not TGN/EE pH was altered in plants lacking both endosomal ClCd and ClCf anion transporters.

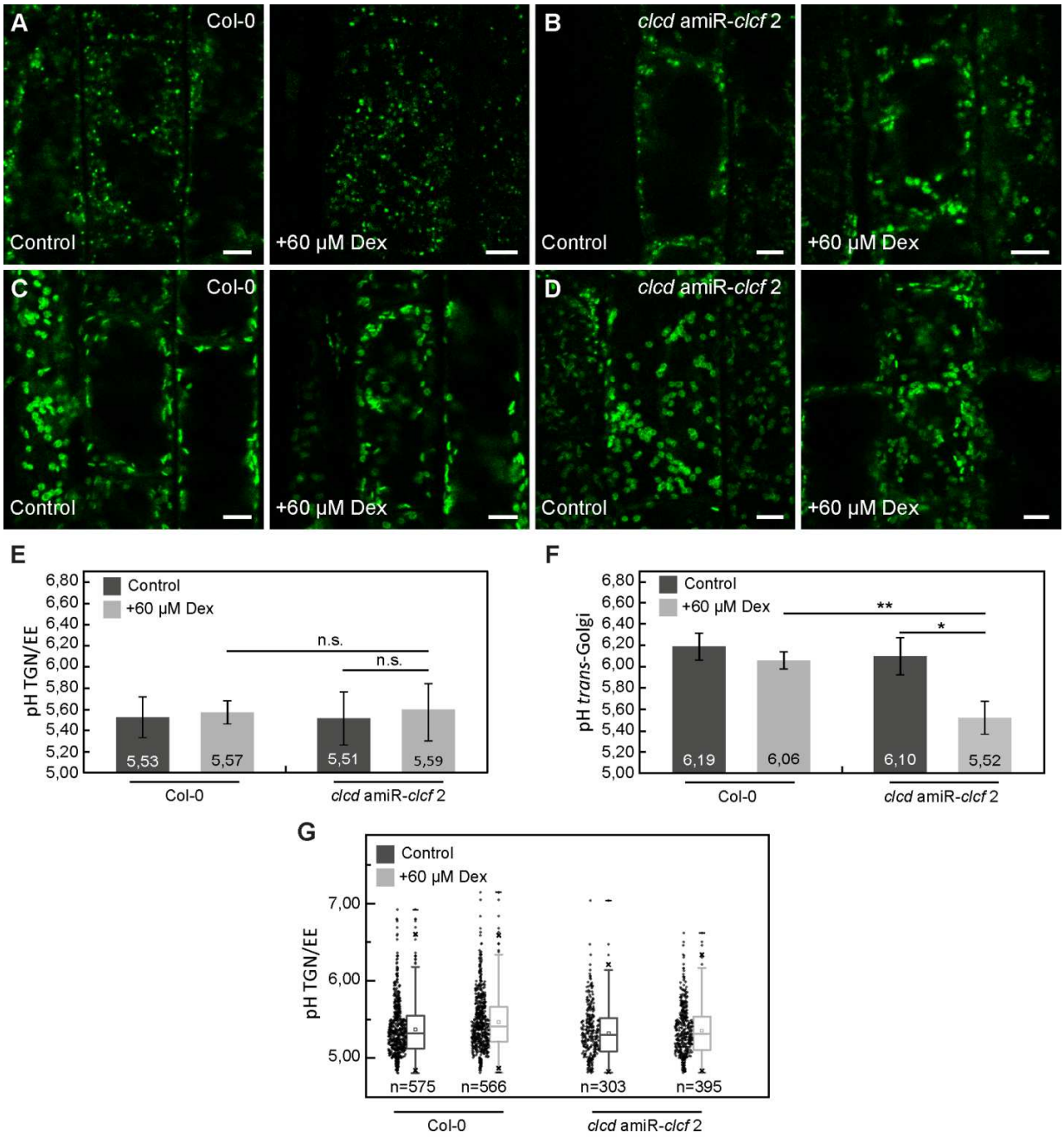

Figure 19: pH in the *trans*-Golgi stack but not the TGN/EE is altered in *clcd* amiR-*clcf*. **(A)** Root cells of 7 days old Arabidopsis seedlings expressing $UBQ10_{Pro}$:SYP61-pHusion 2 in Col-0 or **(B)** *clcd* amiR-*clcf* 2 background after 72h control or Dex treatment. **(C)** Root cells of 7 days old Arabidopsis seedlings expressing $UBQ10_{Pro}$:ST-pHusion in Col-0 or **(D)** *clcd* amiR-*clcf* background after 72h control or Dex treatment. **(E)** *In vivo* pH measurements after 72h Dex treatment using $UBQ10_{Pro}$:SYP61-pHusion 2. Average of 3 independent measurements with n=15 seedlings each. Error bars = SD. **(F)** *In vivo* pH measurements after 72h of Dex treatment using $UBQ10_{Pro}$:ST-pHusion. Error bars = SD of 3 independent measurements with n=15 seedlings each. Asterisks indicate P-values with *=P<0,05; **=P<0,01; ***=P<0,001 or n.s. = P≥ 0,05, P Student´s t-test. **(G)** Distribution of pH values measured in SYP61-pHusion 2 positive particles. Data was extracted from 5 cells per line and condition. Bars= 5µm.

2.3.8. VHA-a1 is partially mislocalised to the *trans*-Golgi stack in *clcd* amiR-*clcf*

As a knock-down of *ClCf* in *clcd* did not affect TGN/EE pH, we investigated whether effects on compartment morphology are present. Hence we introduced the TGN/EE marker VHA-a1-GFP (Dettmer et al., 2006) in *clcd* amiR-*clcf* and observed TGN/EE morphology via CLSM 72h after Dex induction. Whereas signal and localisation of VHA-a1-GFP did not change after 3 days Dex treatment of Col-0 (Figure 20 A, B) and *clcd* (Supplementary Figure S12 A, B), TGN/EEs clustered and inflated in induced *clcd* amiR-*clcf* seedlings (Figure 20 C, D; Supplementary Figure S12 C). Here, only partial co-localisation of VHA-a1-GFP with the styryl dye and endocytic tracer FM 4-64 (Geldner et al., 2003) was observed. Non co-localising VHA-a1-GFP signals were present in ring-like structures similar to *trans*-Golgi signals (compare Figure: 20 C, D) which were not stained with FM 4-64 after 1h chase (Supplementary Figure S13 A-D). However, we did not detect a change of Golgi diameter (Supplementary Figure S13 E). A quantification using Manders correlation coefficients confirmed a decrease in VHA-a1-GFP to FM 4-64 co-localisation (M1) in induced but also in uninduced *clcd* amiR-*clcf* (Figure 20 E). Nevertheless, M2 values representing FM 4-64 signal overlapping with VHA-a1-GFP were already strongly increased in uninduced *clcd* amiR-*clcf* and *clcd* (Supplementary Figure S12 D). In summary, knock-down of *ClCf* in *clcd* causes TGN/EE inflation and aggregation as well as partial mislocalisation of VHA-a1-containing V-ATPases to the *trans*-Golgi stack.

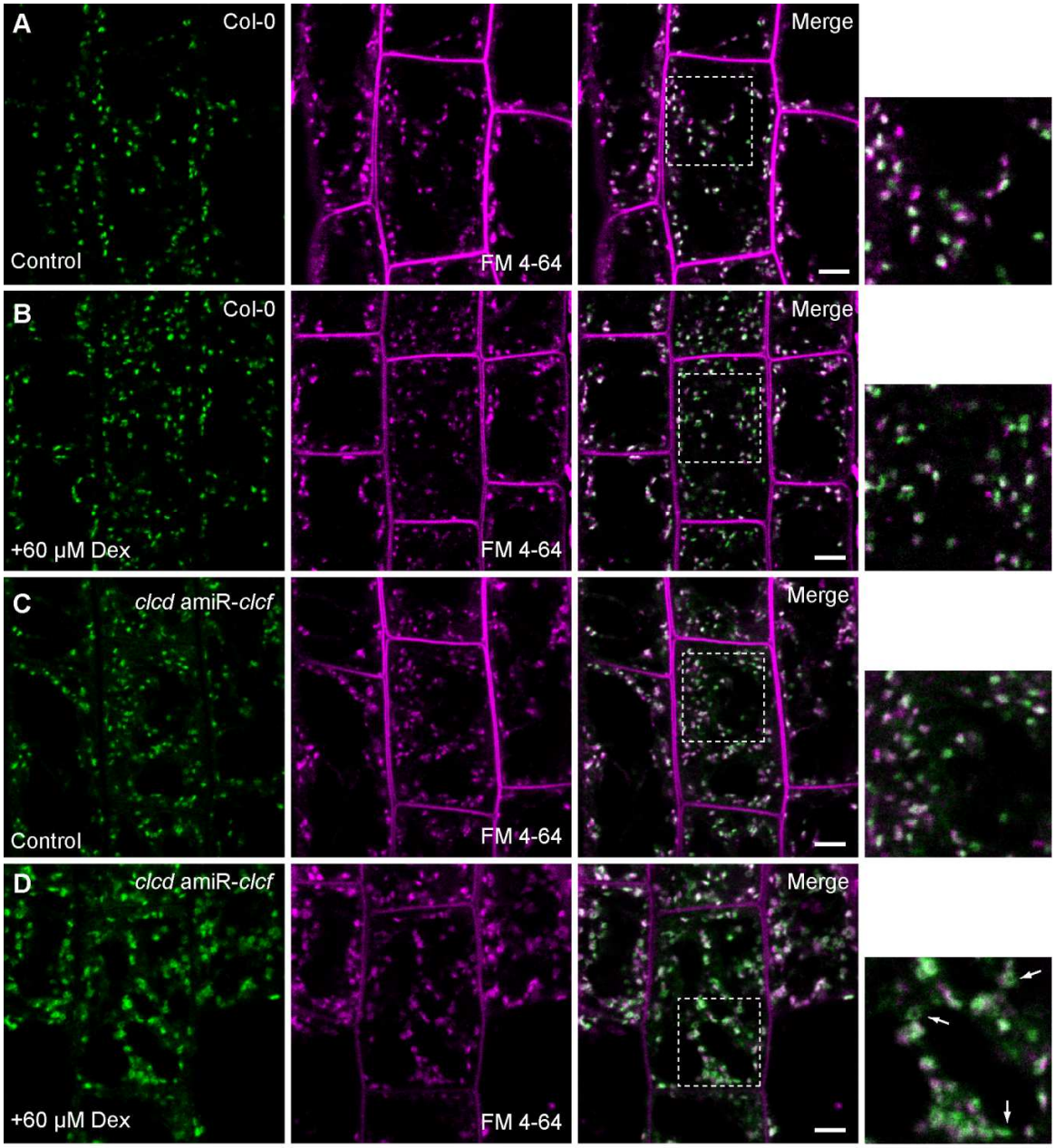
A
Col-0
Control
FM 4-64
Merge
B
Col-0
+60 µM Dex
FM 4-64
Merge
C
clcd amiR-clcf
Control
FM 4-64
Merge
D
clcd amiR-clcf
+60 µM Dex
FM 4-64
Merge

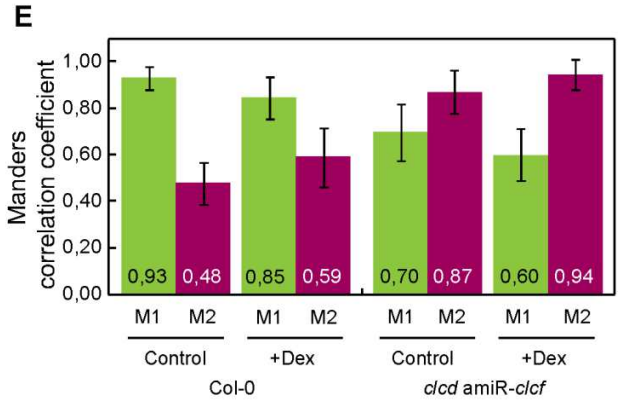
E
Manders correlation coefficient
1,00
0,80
0,60
0,40
0,20
0,00
0,93
0,48
0,85
0,59
0,70
0,87
0,60
0,94
M1
M2
Control
+Dex
Col-0
clcd amiR-clcf

Figure 20: VHA-a1 is partially mislocalised to the Golgi stack in *clcd* amiR-*clcf* CLSM images of elongation zone cells of 6 days old Arabidopsis roots expressing VHA-a1 (green), co-stained with 1 µM FM 4-64 for 15 min (magenta). For Dex treatment, seedlings were transferred after 4 days to 1/2 MS medium plates as control or to plates supplied with 60 µM Dex. Plants were imaged 72h after transfer. CLSM images of **(A, B)** WT Col-0 or **(C, D)** *clcd* amiR-*clcf*. Arrows indicate ring-like structures resembling signals for the *trans*-Golgi stack. Bars = 5µm. Dashed line marks magnified area at right side of corresponding image. **(E)** Manders correlation coefficient of M1: VHA-a1 to FM 4-64 and M2: FM 4-64 to VHA-a1. Data was taken from 10 cells of 10 different roots. Error bars = SD.

2.3.9. Secretion and vacuolar trafficking is not altered in *clcd* amiR-*clcf*

The altered TGN/EE morphology in plants lacking ClCf and ClCd raised the question whether TGN/EE-mediated trafficking is still functional. We therefore crossed plants expressing a secreted version of mRFP (secRFP) (Batoko et al., 2000; Zheng et al., 2005) or the plasma membrane-localized auxin efflux carrier PIN1 (PIN-FORMED1)-GFP (Benková et al., 2003) with both inducible *clcd* amiR-*clcf* lines. Both markers were imaged 72h after amiR induction via Dex in homozygous F_2 lines. Although TGN/EE morphology was altered, both induced *clcd* amiR-*clcf* plants did neither display intracellular accumulations of secRFP (Figure 21 A, C, E) or mislocalisation of PIN1-GFP (Figure 21 B, D, F). Furthermore, we evaluated if vacuolar trafficking is still functional in *clcd* amiR-*clcf* by a FM 4-64 chase experiment. We detected tonoplast labelling in both induced *clcd* amiR-*clcf* lines after 100 min FM 4-64 uptake. In Col-0 and *clcd*, staining of the tonoplast was observed within the same time frame (Figure 21 G-J). We could show that secretion and vacuolar trafficking is operating normally in *clcd* amiR-*clcf* and that trafficking to cell wall and vacuole does not require action of ClCd and ClCf.

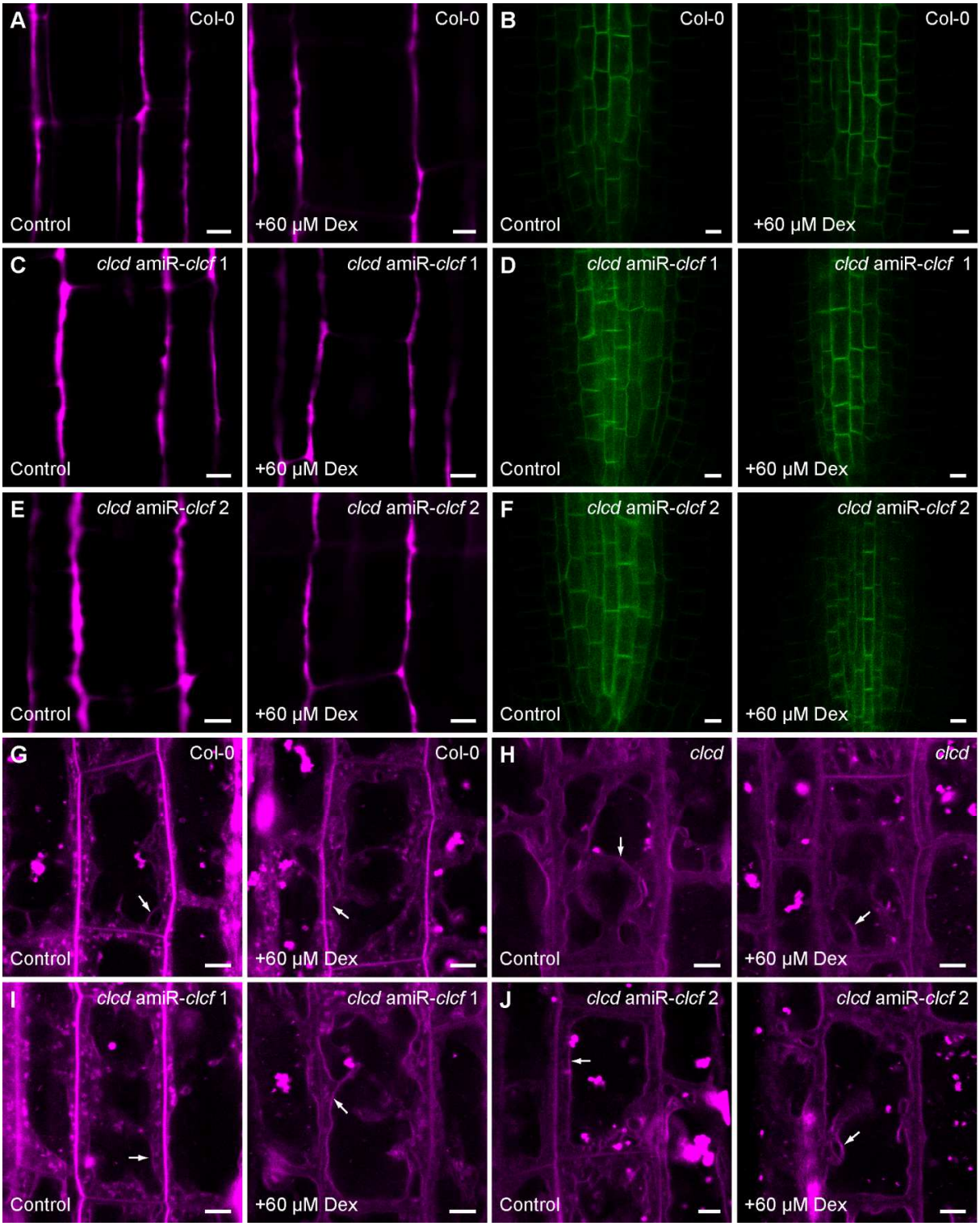

Figure 21: Secretion and vacuolar transport is not altered in *clcd* amiR-*clcf*. CLSM images of root cells of 7 days old Arabidopsis seedlings after 72h of Dex or control treatment. **(A)** Root cells of 7 days old Arabidopsis seedlings expressing secRFP in Col-0 background after 72h control or 60µM Dex treatment. **(B)** Seedling roots of Col-0 expressing PIN1-GFP.

Figure 21 (continued)

(C) secRFP signals in *clcd* amiR-*clcf* 1 are not altered after 72h growth on Dex containing medium. **(D)** PIN1-GFP signals are not altered in control or Dex treated roots in *clcd* amiR-*clcf* 1. **(E)** Signals for secRFP in *clcd* amiR-*clcf* 2 are identical in control and Dex-treated root cells. **(F)** *clcd* amiR-*clcf* 2 expressing PIN1-GFP do not show different signals in Dex and control treatments. Chase of the endocytic tracer FM 4-64 led to a tonoplast staining after 100 min in **(G)** WT Col-0, **(H)** clcd, **(I)** *clcd* amiR-*clcf* 1 or **(J)** *clcd* amiR- *clcf* 2, respectively. Arrows indicate labeled tonoplast. Bars= 5µm.

2.3.10. e^2GFP-mRFP is not suitable for *in vivo* chloride measurements in the TGN/EE of *Arabidopsis thaliana*

Trafficking and TGN/EE pH was not altered in induced *clcd* amiR-*clcf* plants but TGN/EEs were clustered and inflated. Effects on compartment structure might solely be caused by anion deficiency in the TGN/EE lumen due to absence of both ClCs. To test if plants lacking ClCd and ClCf accumulate less Cl^- in the TGN/EE, we generated a GFP-based chloride/pH sensor according to Arosio et al., 2010. By exchange of threonine with tyrosine at position 203 in the eGFP sequence a Cl^- binding site was introduced generating "e^2GFP". Thereby, e^2GFP fluorescence gets quenched upon Cl^- presence (Arosio et al., 2007).

To form the chloride/pH sensing e^2GFP, threonine 203, which is located adjacent to the chromophore region of eGFP (Figure 22 A) was replaced by a two base exchange to tyrosine (Figure 22 B). Identically to pHusion, e^2GFP was linked to the chloride and pH insensitive mRFP for normalisation. To target e^2GFP-mRFP to the TGN/EE lumen, C-terminal linkage to SYP61 was performed. SYP61- e^2GFP-mRFP was overexpressed by the *P16* promoter and finally transformed into *Arabidopsis thaliana* ecotype Col-0 as well as into *clcf*. However, stable expressing Arabidopsis lines in Col-0 and *clcf* background did not show fluorescence for the e^2GFP but for mRFP channel only (Figure 22 C, D). Also when grown on John`s medium devoid of chloride and nitrate, only mRFP signal could be detected (Figure 22 E, F). Thus, it seemed that e^2GFP fluorescence was strongly quenched due to the additional chloride binding site increasing pK_a to 6,81 (Arosio et al., 2010) (pK_a pHusion 5,8; Gjetting et al., 2012) and was therefore not detectable in the acidic TGN/EE lumen.

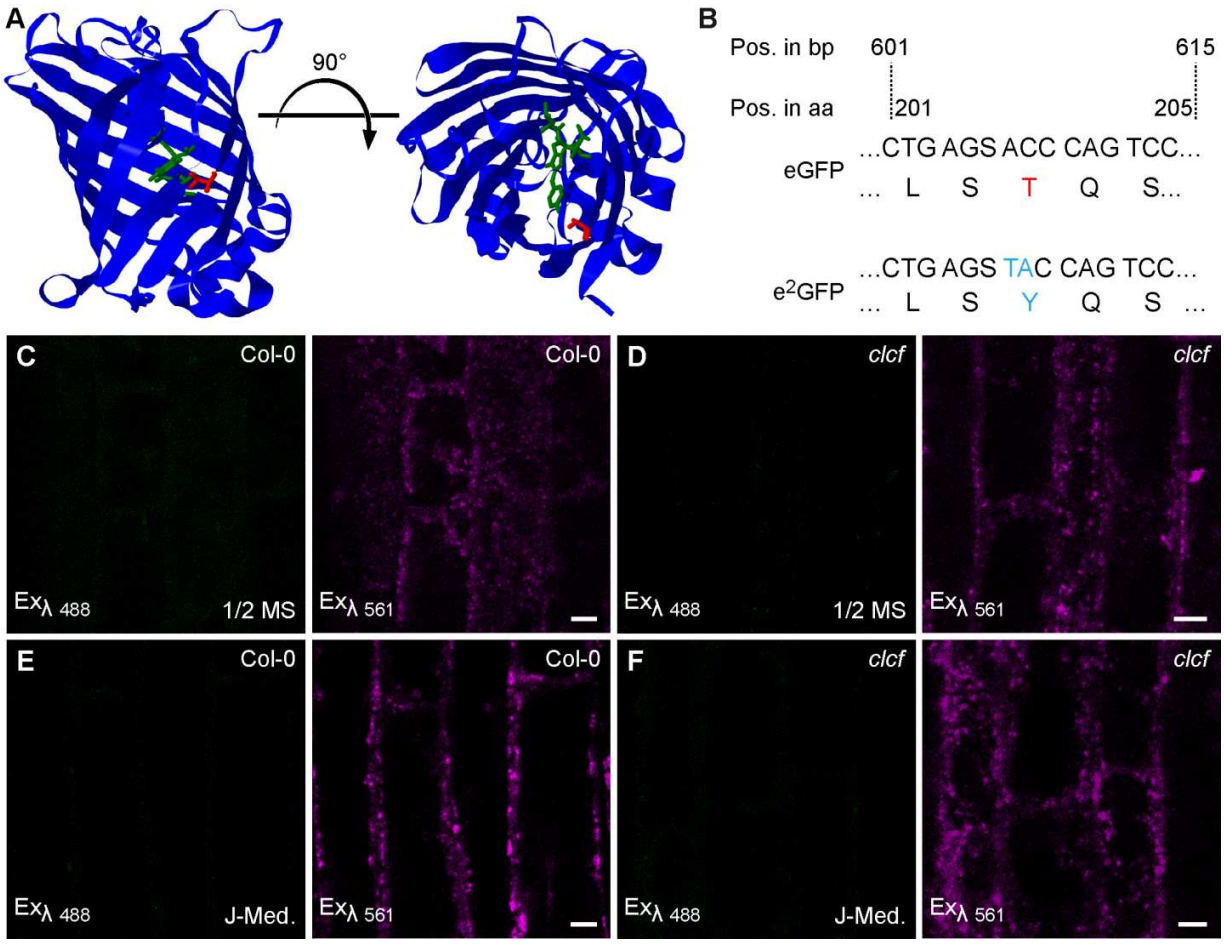

Figure 22: The chloride/pH sensor SYP61-e^{2}GFP-mRFP is not detectable in the TGN/EE. (A) Ribbon model of eGFP (blue) with stick model of amino acid threonine 203 (red) relative to the chromophore. Amino acids flanking chromophore region 64 (leucine) and 68 (valine) are highlighted in green. **(B)** By exchange of 2 basepairs (cyan) in the eGFP sequence, threonine 203 (red) is converted to tyrosine which is able to bind Cl^-. **(C)** P16$_{Pro}$:SYP61-e^{2}GFP-mRFP results in detectable mRFP signals only when stably expressed in Arabidopsis WT Col-0 grown on 1/2 MS medium. **(D)** P16$_{Pro}$:SYP61- e^{2}GFP-mRFP expression in *clcf* grown on 1/2 MS harbored mRFP signals only. **(E)** Identical signals for P16$_{Pro}$:SYP61- e^{2}GFP-mRFP are observed when **(E)** Col-0 or **(F)** *clcf* plants are grown on Cl^- and NO_3^- free John`s medium (J-Med.). All CLSM images were taken in root elongation or differentiation zones of 6 days old plants. Bars = 5 µm.

2.3.11. Computational structure prediction of ClCd and ClCf

ClCd has been predicted to act as a Cl^-/H^+ antiporter due to conservation of critical amino acids for ion selectivity and proton coupling to the well characterised ClC-ec1 $2Cl^-/1H^+$ antiporter from *Escherichia coli* (*E.coli*) (Zifarelli and Pusch, 2010). However, amino acid sequence of ClCf differs from ClCd and other characterised plant ClC proteins. Thus ClCf has been proposed to function as Cl^- channel (Marmagne et al., 2007).

In order to predict critical residues for anion selectivity and transport mode within the protein structure, we generated a structural model for both TGN/EE-localised ClCs using the online protein structure prediction tool "I Tasser" (http://zhanglab.ccmb.med.umich.edu). The annotated, full length amino acid sequence of ClCd and ClCf (www.arabidopsis.org) was sent as query without reference structure for the program in order to find the best matching data. The crystal structure of the eukaryotic CmClC from the thermophilic red algae species *Cyanidioschyzon merolae* (Feng et al., 2010) was chosen by the program as template for modelling of ClCd and ClCf, respectively. CmClC has a sequence identity of 21,2% to ClCd and 17,3% to ClCf. Despite a sequence identity of only 14,1%, a similar structure was predicted for both ClCs (Figure 23 A; Supplementary Figure S14 A, B). Alignment of ClCd and ClCf structures resulted in a high TM (template modelling)-score of 0,73 whereby 1,00 indicates identical sequence and 0,3 and below a rather random structure similarity. An even higher TM-score was present at alignment between ClCd and CmClC (0,986) (Supplementary Figure S15 A) and ClCf and CmClC (TM Score: 0,963) (Supplementary Figure S15 B) indicating almost identical protein structures. However for ClCf, fold of the first 35 amino acids of the N-terminus could not be determined (Supplementary Figure S15 C) and were thus not aligned in all structural comparisons.

We next investigated whether critical residues required for anion selectivity and transport mode can be identified in ClCd and ClCf. We aligned amino acid sequences of both TGN/EE-localised ClCs with CmClCa and the well characterised ClC-ec1 2 Cl^-/H^+ antiporter from *E.coli* (Supplementary Figure S15 D). In ClCd, we could classify the "gating" glutamate 192 and "proton" glutamate 259 required for pore gating and H^+ coupling based on conserved amino acids in ClC-ec1 and CmClC. Furthermore, a serine 149 and tyrosine 562 was identified and located in the transporter core close to Glu 192 and Glu 259 (Figure 23 B; Supplementary Figure S14 C). In ClCf, we found only two conserved critical amino acids in comparison to all other aligned ClCs (Supplementary Figure S15 D). The "gating" glutamate residue at position 247 was the only residue shared with all other ClCs. We further identified a tyrosine 301 situated at the

"proton" residue which is also present in the experimentally confirmed Cl^-/H^+ antiporter CmClC (Feng et al., 2010) (Supplementary Figure S15 D). ClC channels such as TmClC-0 or HsClC-1 carry a valine at this position (Supplementary Figure S15 D). At the selectivity filter position, glycine 192 was located, which is also present in AtClCe (data not shown) and was predicted to be able to serve as Cl^- binding site by the I Tasser software. Adjacent to "gating" glutamate E247 and G192, a tyrosine 463 was identified, however, not at identical position as Y562 in ClCd (Figure 23 B; Supplementary Figure S14 D). According to structure and critical residues for Cl^- binding, selectivity and H^+ coupling, ClCd is likely to function as Cl^-/H^+ antiporter. ClCf has identical amino acids of gating glutamate and proton tyrosine to CmClC, but Cl^- selectivity filter residues appear to be different or are conferred by other residues.

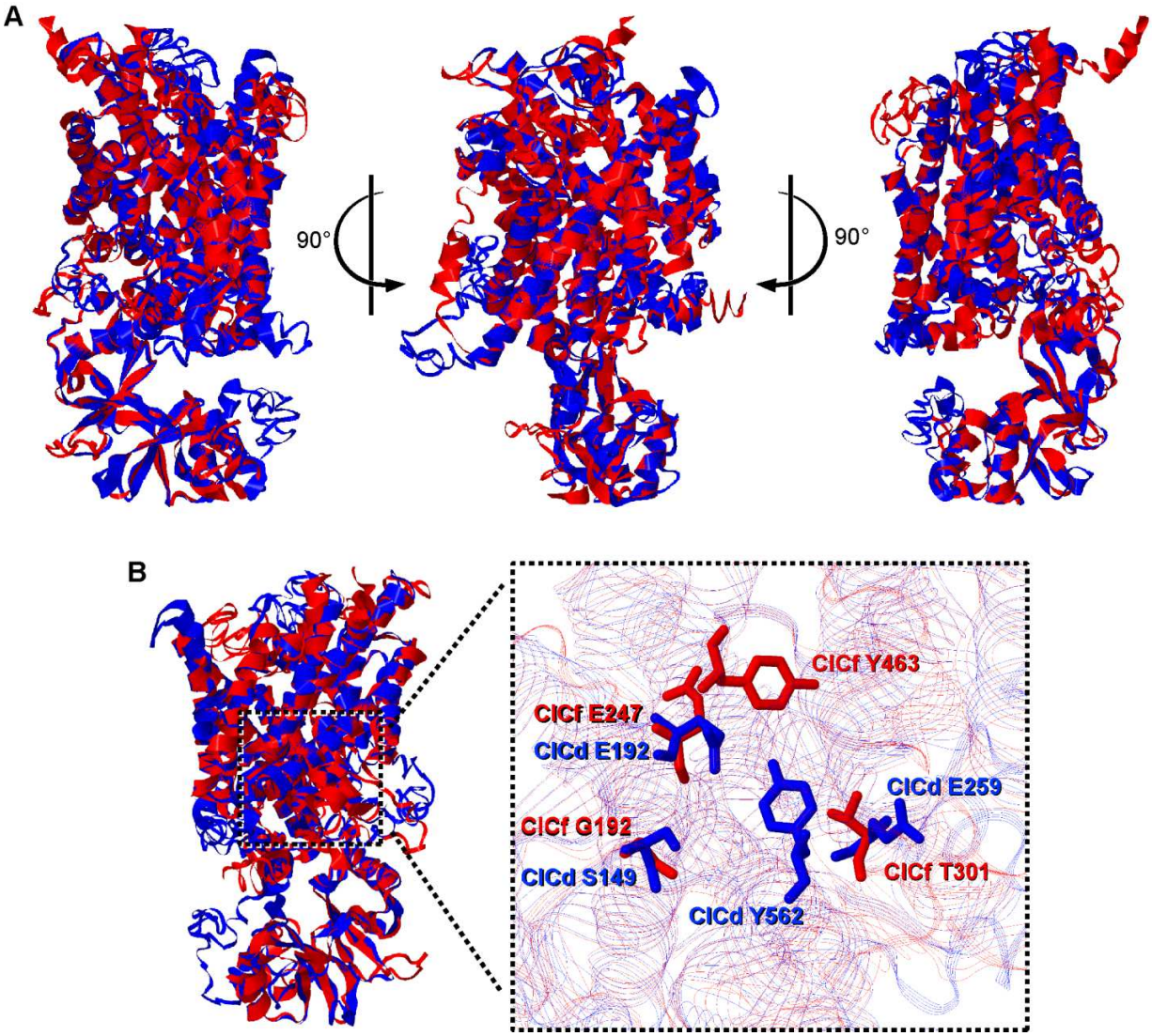

Figure 23: Structural model and analysis of critical residues of ClCd and ClCf. All structures were generated using the online tool I Tasser based on the crystal structure of the eukaryotic CmClC from the red algae *Cyanidioschyzon merolae*. Models were rotated 90° to left and 90° to the right from centered view. **(A)** Alignment of ClCd (blue) and ClCf (red) model structures displayed as ribbon fold. **(B)** ClCd (blue) and ClCf (red) model structures with highlighted critical residues as stick models.

2.3.12. Re-targeting of endosomal ClCs to the tonoplast

To experimentally determine whether ClCd and ClCf function as antiporter or channel and which anion is preferentially transported, electrophysiological measurements are required. A prerequisite for this approach is the re-targeting of the TGN/EE-localised transporters to the tonoplast since the vacuole can be subjected to electrophysiological measurements. Moreover, TGN/EE and vacuole share an acidic intraluminal pH which potentially can have influences on activity or protein conformation. For redirection, we exchanged either the first 35 amino acids (aa) of ClCd and ClCf with those of the tonoplast-localised ClCa (De Angeli et al., 2006) or the last 13 aa with the vacuolar *myo*-inositol transporter INT1 (Wolfenstetter et al., 2012). All constructs were overexpressed by the UBQ10 promoter in Arabidopsis mesophyll protoplasts and imaged 3 days after PEG-mediated transfection.

For ClCf_INT1-GFP a presumably cytosolic or plasma membrane signal was observed (Supplementary Figure S16 A). ClCd_INT1-GFP was concentrated in motile, punctate structures identical to the ClCd-GFP signal perceived in Arabidopsis roots (Supplementary Figure S16 B). However, by the exchange of the first 35 aa of ClCf with those of ClCa, signals for ClCa_ClCf-GFP were almost exclusively found in the Endoplasmic Reticulum (ER) and in rare cases focused in dot-like structures on or adjacent to the ER (Supplementary Figure S16 C). Contrary to ClCa_ClCf-GFP, in all protoplasts expressing ClCa_ClCd-GFP a cell-peripheral signal was detected (Figure 24 A). This signal did not overlap with the FM 4-64-stained plasma membrane (Figure 24 B). Additionally, ClCa_ClCd-GFP signals strongly resembled ClCa-GFP (Figure 24 C) and thus we concluded that ClCd was successfully re-targeted to the tonoplast.

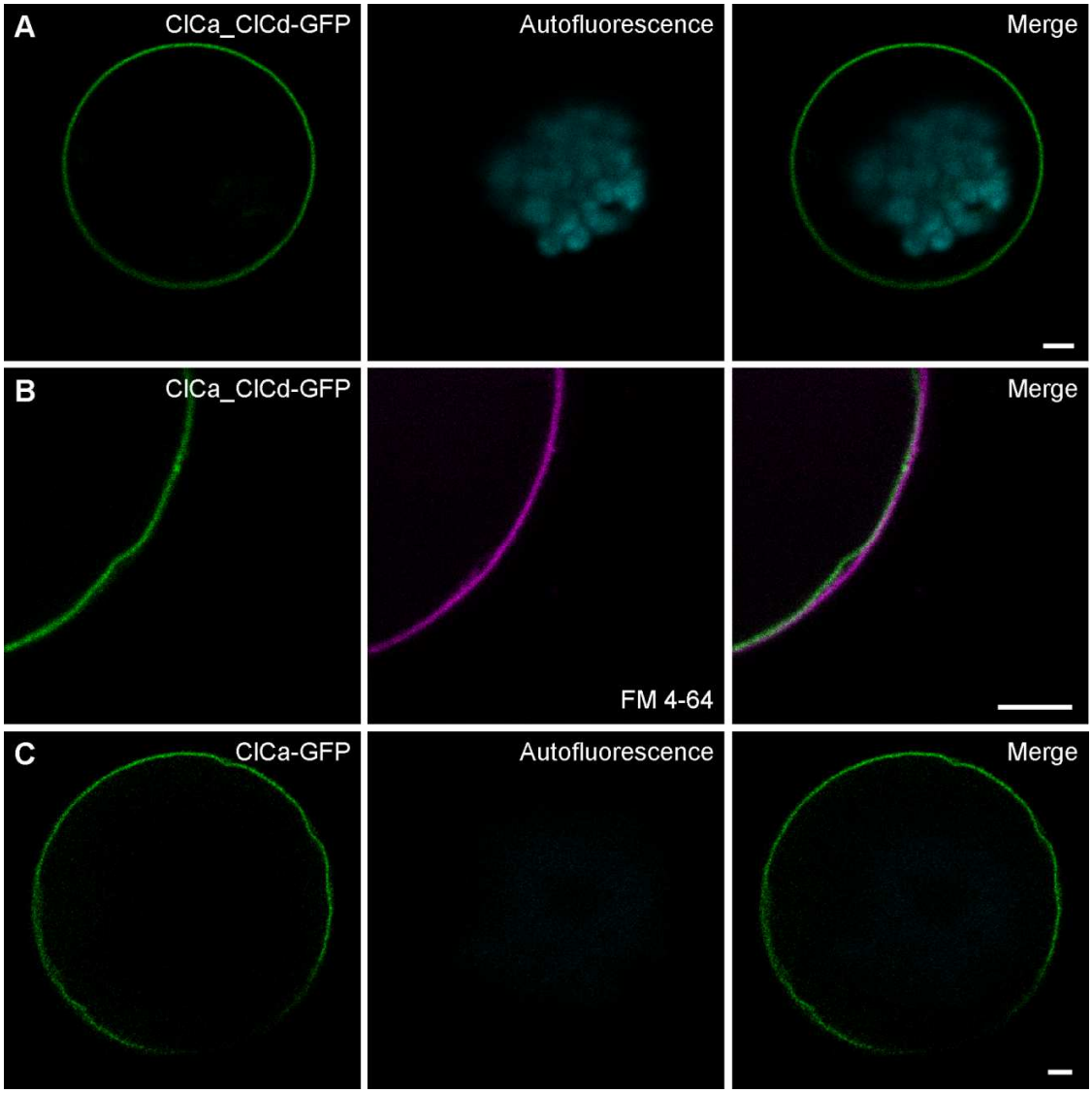

Figure 24: Redirection of ClCd to the tonoplast. CLSM images of Arabidopsis mesophyll protoplasts 3 days after transfection. **(A)** Exchange of the first 45 amino acids of ClCd with ClCa is sufficient to alter ClCd localisation to a ring structure surrounding the cell. **(B)** Co-staining of the plasma membrane with 1 µM FM 4-64 does not overlap with ClCa_ClCd and confirmed a tonoplast localisation of the construct. **(C)** Tonoplast signal of $UBQ10_{Pro}$:ClCa-GFP in Arabidopsis mesophyll protoplasts. Bars=5µm.
Experiments were done jointly with Franziska Lesche.

3. Discussion

3.1. *In vivo* pH measurements in the TGN/EE of *Arabidopsis thaliana*

3.1.1. SYP61-pHusion as *in vivo* TGN/EE pH sensor

The *trans*-Golgi network (TGN) /early endosome (EE) is the central hub of secretory and endocytic pathways (Reyes et al., 2011). Vacuolar proton (H^+)-ATPase (V-ATPase) activity at the TGN/EE is crucial for functional protein trafficking via both routes (Viotti et al., 2010). Previous measurements of V-ATPase activity in the TGN/EE, which is represented by acidification to a large extend, were done mainly in transient expression systems. Furthermore measurements were performed using the pH probe pHluorin and -variants (Miesenböck et al., 1998) which are theoretically functional between pH 5,4 and 8,4 (Martinière et al., 2013b). Nevertheless, as TGN/EE function and morphology is determined by VHA-a1-containing V-ATPases compartment pH is presumably rather low.

We therefore employed the pH probe pHusion (pK_a = 5,8; Gjetting et al., 2012) which was shown to be fluorescent in highly acidic conditions (Fendrych et al., 2016). To target the pH sensor *in vivo* to the TGN/EE, pHusion was linked to the TGN/EE-localised SNARE protein SYNTAXIN OF PLANTS 61 (SYP61; Sanderfoot et al., 2001). C-terminal tagging of SYP61 exposed pHusion to the compartment lumen, which also succeeded in a similar approach to identify the localisation of the mammalian SNARE protein SYNTAXIN 1A (Yang et al., 2006). Our SYP61-pHusion *in vivo* calibration showed that pH values between 7,6 down to pH 4,8 can be reliably measured (Figure 7 A). All *in vivo* calibrations resulted in sigmoidal calibration curves similar to pHusion *in vitro* calibrations (Gjetting et al., 2012). We therefore assumed that pHusion functions correctly when exposed to the cellular environment. As calibration agent we used ammoniumacetate which was employed in similar approaches to measure pH in the plant vacuole (Yoshida, 1994; Krebs et al., 2010; Kriegel et al., 2015). Ammonium (NH_4^+) is in equilibrium with the membrane permeable weak base ammonia (NH_3) which enters acidic compartments where it reacts with one proton to NH_4^+ (Yoshida, 1994; Poëa-Guyon et al., 2013). Thereby, OH^- in the cytosol and H^+ in endosomal lumina are consumed resulting in dissolved pH gradients across endomembranes. For each compartment sensor and orientation, separate calibration curves were generated. Each compartment features with its unique composition of ions, organic acids and others a microenvironment potentially influencing sensor properties (Martinière et al., 2013b). By *in vivo* calibration, the pH sensor is adjusted to the conditions present in the respective compartment diminishing or excluding unspecific effects.

However, we cannot rule out that ammoniumacetate alters the native ionic composition and buffer capacity of compartment lumina which could affect properties of the pH probe (Martinière et al., 2013b).

We determined a steady state TGN/EE pH of 5,6 which was significantly lower to values measured by Shen et al. and Martinière et al. In these reports different pH sensors and evaluation methods were applied compared to our approach. Both studies employed pHluorin-based pH probes which can detect pH values down to pH 6,0 (Martinière et al., 2013a) or pH 5,0 (Shen et al., 2013). Shen et al. 2013 reported a TGN/EE pH of 6,2 in Arabidopsis protoplasts using plant-solubility-modified PRpHluorin. Here, all pH values were calculated based on calibration of cytosolic PRpHluorin. Martinière et al. 2013a measured pH 6,4 in Tobacco leaves and pH 6,1 in Arabidopsis roots using pHluorin linked to the VACUOLAR PROTEIN STORAGE RECEPTOR 4 (VSR4) in co-localising particles with SYP61. *In vivo* pH values were calculated from *in vitro* calibration curves.

The fact that we measured a TGN/EE pH of 5,6 after *in vivo* calibration in compartments where measurements were conducted with a pH sensor with low pK_a suggest that TGN/EE pH is actually more acidic than previously reported.

3.1.2. VHA-a1-containing V-ATPases are responsible for TGN/EE acidification

The TGN/EE represents a major location of V-ATPase complexes containing the VHA-a1 subunit (Dettmer et al., 2006). Secreted and endocytosed proteins accumulate in the TGN/EE after V-ATPase inhibition and thus V-ATPase-mediated acidification seems essential for functional trafficking (Viotti et al., 2010). We could show that VHA-a1-containing V-ATPases are directly involved in TGN/EE acidification. Pharmacological V-ATPase inhibition via Concanamycin A (ConcA) (Huss et al., 2002) effected an almost full neutralisation of the TGN/EE lumen. In addition, reduction of total V-ATPase activity led to an alkalisation of TGN/EE pH. Furthermore, we used the *det3 (de-etiolated 3)* mutant which has a reduced total V-ATPase activity by 60% caused by a weak allele of the mutual V-ATPase VHA-C-subunit (Schumacher et al., 1999). In *det3*, steady state pH of the TGN/EE but not of the vacuole was approximately 0,5 pH units more alkaline than WT. These results confirmed previous assumptions that reduced V-ATPase activity at the TGN/EE is sufficient to restrict cell elongation (Brüx et al., 2008). Likewise, the altered TGN/EE pH of *det3* affected cycling of the brassinosteroid-receptor BRI1 (BRASSINOSTEROID INSENSITIVE1; Friedrichsen et al., 2000) and exocytosis of cellulose synthase complexes (CSCs) (Luo et al., 2015) depicting that compartment acidification is required for TGN/EE-mediated trafficking processes. The reduced cellulose content in *det3*

causing inhibition of cell elongation (Brüx et al., 2008) can therefore be explained by partially inhibited exocytosis of CSCs due to impaired TGN/EE acidification. An improper assembly of CSCs, which takes place in the Golgi apparatus (Zhang et al., 2016), is unlikely hence *trans*-Golgi pH in *det3* did not differ from WT. Despite an average TGN/EE pH of 6,1 compartment morphology was not changed in *det3* in contrast to TGN/EE-Golgi hybrids observed after full V-ATPase inhibition by ConcA. Results suggest that certain pH alterations in the TGN/EE deviating from the measured average of pH 5,6 can be tolerated.

Why is exclusively TGN/EE pH altered in *det3*? *det3* carries a single basepair exchange in intron 1 of *VHA-C.* This deleted the brachpoint consensus sequence 32 bp upstream of the actual 3`splice site of intron 1 resulting in a retained intron and thus non-functional VHA-C (Schumacher et al., 1999). However, an alternative brachpoint consensus is located 10 bp upstream of the mutation which effects that that the *det3* mutation is spliced out leading to 50 % residual V-ATPase activity. Distribution of remaining functional VHA-C subunits could occur to a higher rate in VHA-a2 and VHA-a3-containing V-ATPases. The result would be an underrepresentation of TGN/EE-localised V-ATPases and consequently a reduced acidification of the compartment.

To monitor if a stronger TGN/EE pH increase can be caused by a specific knock-down of the TGN/EE-localised V-ATPase, we next measured TGN/EE pH in dexamethasone(Dex)-inducible artificial micro RNA (amiR) lines targeting VHA-a1. Here, strong reduction in root and hypocotyl length as well as TGN/EE inflation and aggregation was observed upon amiR induction (Dissertation Dr. Anne Kriegel 2015). These effects propose that an amiR-*vha-a1*-mediated knock-down has more severe effects on the TGN/EE than *det3*. Opposed to these findings, TGN/EE pH of uninduced amiR-*vha-a1* was already significantly increased compared to WT. However, plants did not show growth alterations despite the shifted pH in the TGN/EE which could hint to weak promoter activity in absence of dexamethasone. Contrariwise, TGN/EE pH tended to be more acidic upon Dex-induction of the amiR targeting *vha-a1* compared to uninduced controls (Figure 9 D). An explanation for this slight TGN/EE acidification could be an influence of the acidic apoplast via endocytic vesicle import. Endocytosis is not affected at V-ATPase inhibition (Dettmer et al., 2006; Viotti et al., 2010). amiR-*vha-a1* knock-downs clearly reduce VHA-a1 protein levels (Dissertation Dr. Anne Kriegel 2015) which would in turn lead to reduced proton import into the TGN/EE. However, endocytic vesicles coming from the apoplast (pH 5,4) could import protons along with their cargo in the TGN/EE and thereby diminish luminal TGN/EE pH. To answer this hypothesis, inhibition of the plasma membrane-localised P-type

ATPase in induced amiR-*vha-a1* would be a key experiment. Furthermore, a contribution from the *trans*-Golgi cistern to TGN/EE pH might be possible. TGN/EE and Golgi apparatus are interconnected. An alteration in TGN/EE pH could feed back on the Golgi stack and promote Golgi acidification as well as Golgi-to-TGN/EE trafficking rates. It is therefore necessary to find out how Golgi acidification is mediated (discussed in 3.1.5.) and if Golgi and TGN/EE can cross-regulate luminal pH of their neighbour compartment.

3.1.3. TGN/EE-localised antiporter co-determine compartment steady state pH

The steady state TGN/EE pH of 5,6 in Arabidopsis WT roots represents the net result of proton supply by the V-ATPase and proton consumption (Schumacher, 2014). We demonstrated that TGN/EEs in the *nhx5 nhx6* mutant lacking two K^+/H^+ antiporter (Bassil et al., 2011a) were 0,5 pH units more acidic compared to WT. This difference was also measured in an earlier approach (Reguera et al., 2015). Results illustrate that activity both K^+/H^+ antiporter co-determine TGN/EE pH and that part of the protons are used up by those transporters. Previous reports of missorting of vacuolar cargo to the apoplastic space in *nhx5 nhx6* (Bassil et al., 2011a) confirm than pH in the TGN/EE needs to be maintained at steady state levels for functional protein trafficking. Whether both antiporter also serve as a "proton safety valve" to prevent compartment over-acidification (Bassil et al., 2012) or whether the increased TGN/EE acidification is caused simply by elimination of a major proton consumer cannot be stated. Nevertheless, NHX5 and NHX6 do not participate in establishment of TGN/EE acidification.

3.1.4. pH in individual TGN/EEs

In all TGN/EE pH measurements we calculated the average pH from all TGN/EEs present in the respective images. pH values of single TGN/EEs were not considered by this evaluation method. Thus ratio images of Z-stacks across single root cells of SYP61-pHusion 2 expressing Arabidopsis plants were taken. We gathered evidence that pH in individual TGN/EEs is not uniform (Figure 10). pH measurements in SYP61-pHusion positive particles, which represent single or clustered TGN/EEs, as well as a TGN/EE subdomain, determined that pH can range from pH 5,0 and below, up to pH 6,0 to 6,2. Thereby TGN/EE pH appeared to be modulated locally at prospective homotypic fusion or membrane fission sites.

By now it is established that the TGN/EE has different subdomains where secretory vesicles (SVs), clathrin-coated vesicles (CCVs) (Boutté et al., 2013) and multivesicular bodies (MVB)/ late endosomes (LE) are formed (Scheuring et al., 2011). It would be now worthwhile to monitor if certain TGN/EE subdomains also feature distinct pH conditions and if for instance sites of

vesicle fusion/fission coincide with high/low pH. In this respect a comparison between pH of Golgi-associated and non-associated TGN/EEs would be interesting. It has been postulated that Golgi-associated TGN/EEs take up cargo from the Golgi stack for further distribution in the cell, whereas an individual TGN/EE function in secretion and uptake of endocytosed material (Viotti et al., 2010).

Nevertheless, a full confirmation of our results is necessary beforehand. Observed pH gradients in single TGN/EEs could also have been caused by fluctuations in the microscopical system or by bleaching of one fluorophore. Therefore, ratios using pHusion exposed to the cytosol (pHusion-SYP61) or two luminal localised, non pH-responsive fluorophores should be taken. Furthermore, all ratios were recorded with Z-stacks and homotypic fusions could only be observed when TGN/EEs were moving in the scan direction. Ratios taken over time and in a defined Z-volume would be more precise and would allow tracking of individual TGN/EEs.

3.1.5. The V-ATPase does not acidify the Golgi stack

Although Golgi motility was slower in *det3* (Luo et al., 2015) neither steady state *trans*-Golgi pH was altered in *det3*, nor *cis* and *trans*-Golgi pH changes were observed after 3h ConcA treatment in preliminary experiments. Results suggest that *trans*-Golgi cisternae are acidified independently of the V-ATPase in Arabidopsis. This would differ drastically from animal cells, where a subproportion of the V-ATPase is responsible for Golgi acidification (Paroutis et al., 2004). Good candidates for *trans*-Golgi acidification in Arabidopsis are the two isoforms of H^+-translocating pyrophosphatases (H^+-PPases) VHP2;1 and VHP2;2 (Segami et al., 2010) which are located at *trans*-Golgi cisternae (Mitsuda et al., 2001). H^+-PPases are composed out of a single polypeptide chain with 17 predicted transmembrane domains (Segami et al., 2010). To drive luminal H^+ translocation those proton pumps hydrolyse inorganic pyrophosphate (PP_i). Double mutants of VHP2;1 and VHP2;2 where VHP2;2 is completely and VHP2;1 is partly reduced in protein levels by approx. 70% to WT (Dr. Shoji Segami, personal communication) do not show phenotypes. By introduction of a Dex-inducible amiR targeting both VHP2 isoforms we plan to further reduce VHP2 levels. Dex treatment of T_1 plants expressing amiR-*vhp2* drastically diminished plant size which proposed an important function of VHP2;1 and VHP2;2. We now want to determine whether reduction of both VHP2 isoforms causes alkalisation of *trans*-Golgi pH. Furthermore, we plan to test whether VHP2;1 and VHP2;2 are also responsible for the weak acidification of *cis*-Golgi cisternae. Ultimately, we will monitor whether both H^+-PPases contribute to TGN/EE pH.

3.2. Contribution of the TGN/EE to vacuolar acidification

Root cell vacuoles of plants that do not have active proton pumps at the tonoplast (*vha-a2 vha-a3 fugu5-1*) are still acidified to approximately pH 6,5 (Kriegel et al., 2015). V-ATPase inhibition via ConcA neutralised vacuolar pH. Since in *vha-a2 vha-a3 fugu5-1*, the only ConcA target left are VHA-a1-containing V-ATPases, a contribution of the TGN/EE-localised V-ATPase to vacuolar acidification was shown (Kriegel et al., 2015). We investigated whether the TGN/EE transports H^+ to the vacuole via one or several TGN/EE trafficking pathways.

If a H^+-transporting trafficking pathway from TGN/EE to the vacuole is disabled, an alkalisation of the vacuole would be the logical consequence. We measured a more alkaline vacuolar pH in mutants with deficiencies in the ß-subunit of the tetrameric adaptor protein (AP)-3 required for CCV formation. In *wat 1-1D* (*weak acid tolerant 1-1D*) which expresses a truncated ß-subunit (Niñoles et al., 2013) or *pat2-2* (*protein affected trafficking 2-2*) lacking respective AP-3 subunit (Feraru et al., 2010), vacuolar pH was increased relative to WT. However, pH difference to WT was significant in *pat2-2,* whereas *wat 1-1D* only tended to have a higher vacuolar pH. *wat1-1D* is an activation tagged line (Weigel et al., 2000). Here, a 35S enhancer element is located on the T-DNA inserted in the gene encoding the AP-3 ß-subunit. This 35S enhancer leads to overexpression of the truncated ß-subunit (Niñoles et al., 2013). Overexpression could either cause secondary effects or other genes in proximity of the 35S enhancer sequence are overexpressed as well causing higher variations in vacuolar pH. The *pat2-2* mutant contains a T-DNA in intron 1 with a premature stop codon. (Feraru et al., 2010). Since only this particular gene is affected, vacuolar pH could be less variable in *pat2-2*. Nevertheless, presence of a second T-DNA insertion cannot be excluded.

In knock-outs of the µ-subunit of the AP-1 complex the opposite effect on vacuolar pH was present. *hap13* (*hapless13*) and *ap1m2-1* mutants (Park et al., 2013) harboured more acidic vacuoles than WT, respectively (Figure 11). Why do vacuoles of AP-1-affected mutants contain more protons? In contrast to the AP-3 ß-subunit, knock-out of the AP-1 µ-subunit in *hap13* and *ap1m2-1* is lethal (Park et al., 2013). Trafficking to vacuole and plasma membrane are similarly affected in *hap13* (Wang et al., 2013) and in *ap1m2-1* (Park et al., 2013) which hints to a general breakdown of TGN/EE functions as previously suggested (Robinson and Pimpl, 2014). The loss of this essential route could therefore increase vesicle flow of other trafficking pathways, thus leading to the increased vacuolar acidification. Another explanation might be the impaired import of a tonoplast-localised transporter crucial for vacuolar pH homeostasis or an abundant tonoplast protein consuming a large part of the membrane gradient. For instance the

nitrate/proton antiporter ClCa whose knock-outs have a 50% reduction in nitrate content has been implicated in shunting both tonoplast-localised V-ATPases (De Angeli et al., 2006). Also knock-outs of the two tonoplast-localised NHX1 NHX2 K^+/H^+ antiporter had more acidic vacuoles than WT (Bassil et al., 2011b). To be able to distinguish between both effects the trafficking routes of different tonoplast-localised transporters have to be identified.

Furthermore, a communication between vacuolar- and TGN/EE-localised V-ATPase isoforms has been proposed. An amiR-mediated knock-down of VHA-a1 led to more acidic vacuoles due to activity increase of the tonoplast V-ATPases (Dissertation Dr. Anne Kriegel 2015). If the AP-1-dependend CCV pathway takes up essential functions in TGN/EE-to-vacuole trafficking, vacuolar proton import would be affected drastically. Tonoplast-localised V-ATPases might thereupon sense the suppressed proton import and upregulate their activity. Interestingly, in *det3* only TGN/EE but not vacuolar pH was altered. However, we do not know if the unaltered pH actually reflects an activity increase of tonoplast-localised V-ATPase isoforms or if the vacuolar V-ATPase pool is preferentially equipped with functional VHA-C. Since specific antibodies against individual VHA-a isoforms are lacking, determination of abundance of the V-ATPase isoforms is not possible. Moreover, we demonstrated that TGN/EE pH in *vha-a2 vha-a3* mutants lacking both tonoplastic V-ATPases (Krebs et al., 2010) resembles WT. Either communication between vacuolar and TGN/EE V-ATPase isoforms is unidirectional or the increased vacuolar pH in amiR-*vha-a1* was not directly caused by a reduction of VHA-a1. However, we might assume that vacuolar pH of 6,4 in *vha-a2 vha-a3* is not altered by elevated VHA-a1 activity but it is unknown whether trafficking rate between TGN/EE and vacuole is increased in *vha-a2 vha-a3*.

Lastly, we did not observe an altered vacuolar pH in *sand1-1* which lacks a component required for MVB/LE maturation (Singh et al., 2014), or after treatment with the phosphatidylinositol 3-kinase inhibitor (PI3K) inhibitor LY294002 (Jung et al., 2002; Lee et al., 2008). MVB/LEs mature out of the TGN/EE and hence luminal pH of both compartments should not be different (Scheuring et al., 2011). However, pH measurements by Martinière et al., 2013a determined that MVB/LEs are 0,7 pH units more alkaline than the TGN/EE. On the other hand, measurements by Shen et al. in 2013 did not observe a difference between TGN/EE and MVB/LE pH. So, do MVB/LEs transport protons? Both studies measured MVB/LE pH in the bulk luminal fluid. Further studies repeating pH measurements *in vivo* should also involve an additional pH sensor located at the inner MVB/LE vesicles. Also, it cannot be excluded that other pathways act in compensation for an MVB/LE loss hence *sand1-1* seedlings are not viable (Singh et al., 2014).

We provided evidence that H^+ are imported via trafficking routes from the TGN/EE to the vacuole, probably via CCVs. However, it is not clear whether MVB/LEs participate in vacuolar H^+ import and whether loss of one trafficking route is compensated by other pathways. An optimal tool for future experiments would be an inducible system to shut down individual or all pathways simultaneously in a selective manner.

3.3. The role of ClC anion/H^+ transporters at the TGN/EE of *Arabidopsis thaliana*

The TGN/EE-localised anion transporter ClCd has been proposed to be required for TGN/EE pH homeostasis by providing shunt conductance for VHA-a1-containing V-ATPases (von der Fecht-Bartenbach et al., 2007). However, absence of a drastic *clcd* phenotype, which would be expected when TGN/EE pH homeostasis is altered, suggested functional redundancy. We considered the plant ClC-family member ClCf (At1g55620) as candidate. ClCf was observed at Golgi stacks and could complement as ClCd the yeast Gef1 mutant deficient in the Golgi-localised ScClC (Marmagne et al., 2007).

We showed that ClCf is located at the TGN/EE together with VHA-a1-containing V-ATPases and ClCd in *Arabidopsis thaliana*. Immunogold labelling confirmed observations made by CLSM. Only partial co-localisation was present with the *trans*-Golgi marker ST (SIALYLTRANSFERASE)-GFP which is generally observed for TGN/EE signals (Viotti et al., 2010). Rarely, gold particles were detected at *trans*-Golgi cisternae in ClCf-mRFP immunolabellings. However, quantifications are required to determine if a proportion of ClCf localises to the *trans*-Golgi cisterna. Ultimately, ClCf-mRFP was not found on MVB/LEs since signals were not altered after Wortmannin treatment (Tse, 2004) causing swelling of MVB/LEs.

Hypocotyl length of *clcf* was, similar to *clcd*, shorter than WT upon V-ATPase inhibition by ConcA suggesting that both ClCs have identical functions. However, no *clcf* phenotypes were present at standard growth conditions. Also, steady state TGN/EE pH of *clcd* and *clcf* resembled WT. A close corporation between ClC proteins and the V-ATPase was proposed (von der Fecht-Bartenbach et al., 2007). We therefore tested whether ClCf is able to directly interact with ClCd and VHA-a1-containing V-ATPases. However, no interaction was detected via FLIM-FRET measurements. Nonetheless, other protein-protein interaction studies are required to fully confirm these observations.

3.3.1. ClCd and ClCf are essential and required for cell elongation

Due to absence of a phenotype in ClC single mutants, we generated a *clcd clcf* mutant by crossing *clcd* and *clcf* T-DNA insertion lines. Reciprocal crosses confirmed that lack of both ClCd and ClCf causes male gametophyte lethality and pointed out an essential role of both TGN/EE-localised ClCs. Introduction of ClCf-mRFP rescued the lethal *clcd clcf* effect which showed that lack of at least *ClCf* lead to this severe phenotype. Rescue plants were nevertheless smaller than WT, probably caused by the C-terminal mRFP.

We subsequently generated a Dex-inducible amiR-mediated knock-down against *ClCf* in the *clcd* background. This amiR could efficiently reduce ClCf protein levels upon Dex induction. Mutation of the amiR recognition site in the *ClCf* ORF did not change fluorescence of the reporter showing that ClCf protein reduction was specifically caused by the amiR targeting *clcf.* Induction of *clcd* amiR-*clcf* inhibited elongation of hypocotyls and roots, respectively. Hence shortened root elongation zones and meristems as well as non-elongated roots hairs observed in both induced *clcd* amiR-*clcf* are probably caused by the inability of cells to expand. A *clcd clcf* mutant could most likely not be generated since pollen tubes were not able to elongate and reach the ovules. Interestingly, hypocotyls of both *clcd* amiR-*clcf* lines, and at least *clcd* amiR-*clcf* 1 roots, were longer than WT in the uninduced state. Probably, a slight reduction of *ClCf* levels due to unspecific activity of the 6xOP promoter was compensated by the plant leading to the observed overshoot in hypocotyl and root length.

We could pinpoint an essential role of ClCd and ClCf in cell elongation. Nevertheless, inhibition of the TGN/EE-localised V-ATPase similarly effects drastic inhibition of cell elongation. Hence we conducted TGN/EE pH measurements to determine if impaired cell elongation in *clcd* amiR-*clcf* was caused by a pH alteration in this compartment.

3.3.2. Reduction of ClCd and ClCf does not alter TGN/EE pH

Since the V-ATPase accumulates positive charges inside the compartment lumen, an anion shunt is necessary to equalise (Paroutis et al., 2004; Schumacher and Krebs, 2010; Stauber and Jentsch, 2013). Due to the strong effects on cell elongation in *clcd* amiR-*clcf* both ClCs could provide this shunt for the TGN/EE-localised V-ATPase.

Surprisingly, TGN/EE pH was not different in induced *clcd* amiR-*clcf* compared to uninduced lines or controls (Figure 19 E; Supplementary Figure S11 G). Also pH values in individual TGN/EEs, subdomains or cluster were indistinguishable from to WT excluding that pH was altered in a TGN/EE subpopulation. These results would propose that both ClCs are not involved

in supporting the V-ATPase in acidification as hypothesised previously (von der Fecht-Bartenbach et al., 2007). On the other hand, if both ClCs are anion/H^+ antiporter, a strong TGN/EE pH decrease as present in *nhx5 nhx6* would be expected since TGN/EE pH represents the sum of proton im- and export processes (Schumacher, 2014). The increased H^+ concentration due to a lack of ClCd and ClCf could be masked by a reduced V-ATPase-mediated proton import resulting in an unaltered TGN/EE pH. This would support that at least parts of charges are balanced by ClCd and ClCf. Another possibility might be that charge balance can partially or fully be maintained by the activity of endosomal NHX5 and NHX6 K^+/H^+ antiporters. The unaltered compartment pH in *clcd* amiR-*clcf* might therefore be derived from a compensation by NHX-transporters.

Clearly, activity of ClCd and ClCf is essential proposing a physiological role of anions or chloride (Cl^-) in the TGN/EE. However, we cannot exclude a role of both ClCs in luminal charge balance. Further studies are required to fully clarify the function of ClCd and ClCf at the TGN/EE. To directly monitor effects on V-ATPase activity, a systematic knock-out of ClCd and ClCf in *nhx5 nhx6* background would eliminate possible regulatory effects coming from NHX activity. Furthermore, analysis of NHX5 NHX6 transcripts in the *clcd* amiR-*clcf* background could give first hints on whether both antiporter families are co-regulated. In the end, charge balance at the TGN/EE could be conducted also by a yet unknown transporter or process.

It is remarkable that no effect on trafficking to the plasma membrane and vacuole was observed in induced *clcd* amiR-*clcf* cells despite clustering and inflation of TGN/EEs. These findings would propose that presence of luminal anions or Cl^- is required for overall compartment structure but not function. Unfortunately, Cl^- levels in the TGN/EE could not be measured due to the fact that the Cl^-/pH-sensor e^2GFP-mRFP was quenched at the acidic TGN/EE pH. Exchange of T203Y in the eGFP sequence increases pK_a from 5,8 in pHusion to a pK_a of 6,81 in e^2GFP-mRFP (Arosio et al., 2010). Perhaps with the FRET sensor Clomeleon which has a pK_a of 5,2 (Kuner and Augustine, 2000; Arosio and Ratto, 2014) *in vivo* Cl^- levels can be determined.

3.3.3. *trans*-Golgi cisternae are increasingly acidified in *clcd* amiR-*clcf*

Curiously, reduction of *ClCf* in *clcd* effected partial mislocalisation of the VHA-a1-containing V-ATPases to *trans*-Golgi cisternae. The TGN/EE marker VHA-a1-GFP was observed in circular structures resembling signals of the *trans*-Golgi marker ST. These structures were never stained by the endocytic tracer FM 4-64 which travels from the plasma membrane via TGN/EE to the vacuole (Geldner et al., 2003). Apparently, V-ATPase mislocalisation led to an acidification of the *trans*-Golgi cisterna by 0,5 pH compared to WT or uninduced *clcd* amiR-*clcf*. This

acidification proposes that the V-ATPase is still able to pump protons despite absence of luminal anions.

Partial mislocalisation to the Golgi stack was further confirmed by a reduction in co-localisation between VHA-a1-GFP and FM 4-64 signal in induced but also uninduced *clcd* amiR-*clcf* cells (Figure 20 E). However, the proportion of FM 4-64 signal co-localising with VHA-a1-GFP was larger in *clcd* amiR-*clcf* and *clcd* compared to WT. This increase might hint that VHA-a1-GFP was mislocalised also to other compartments than the Golgi stack, presumably MVB/LEs. On the other hand, VHA-a1-GFP signals were never observed at MVB/LEs in *clcd* (von der Fecht-Bartenbach et al., 2007) and mislocalisation of a V-ATPase to this compartment would most likely inhibit or severely alter MVB/LE functions. One possible outcome would be inhibited or delayed trafficking to the vacuole which was not the case in *clcd* or *clcd* amiR-*clcf*. Hence it is questionable, whether Manders` correlation coefficient was a suitable quantification method. It is also difficult to distinguish if the correlation increase of FM 4-64 to VHA-a1 was caused by a more broader V-ATPase mislocalisation or due to artefacts such as elevated background fluorescence. Therefore a more precise method to test for VHA-a1 localisation in *clcd* amiR-*clcf* lines would be immunogold labelling. In addition it would provide ultrastructural data to clarify general TGN/EE structure in induced *clcd* amiR-*clcf*.

VHA-a1-containing V-ATPases are partially mislocalised to the *trans*-Golgi cisterna upon reduction of *ClCf* in *clcd*. The connection between luminal anion/Cl^- presence and localisation of TGN/EE resident proteins represents a previously unknown function and no other reports are available. Partial re-localisation was also observed for SYP61 which is a common TGN/EE marker. It would be now interesting to test if proteins that are associated and not integrated in the TGN/EE membrane are similarly mislocalised to the *trans*-Golgi stack when ClCd and ClCf are lacking.

3.3.4. What causes cell elongation defects in *clcd* amiR *clcf*?

The major question from inhibited cell elongation in *clcd* amiR-*clcf* plants is whether impaired cell elongation is the consequence of improper TGN/EE anion/Cl^- homeostasis or of the altered *trans*-Golgi pH. From yeast studies it is known that intracellular Cl^- is required for maturation of the multicopper oxidase Fet3 involved in high-affinity iron uptake (Askwith and Kaplan, 1997). Import of Cl^- is mediated by the Golgi-localised ClC-family Cl^-/H^+ antiporter Gef1 or ScClC (Gaxiola et al., 1998). On the one hand, Cl^- was proposed to function as counterion to balance copper import by the P-type copper ATPase CCC2 (Gaxiola et al., 1998). On the other hand Cl^- could serve as co-factor during the copper loading process by keeping the Fet3 precursor in a

permissive conformation (Davis-Kaplan et al., 1998; Braun et al., 2010). Both, CCC2-mediated copper import and formation of the Fet3 copper-containing active center takes place in the late Golgi and prevacuolar compartment (Gaxiola et al., 1998; Braun et al., 2010).

In Arabidopsis the CCC2 homologue is the P-type copper ATPase RAN1 (RESPONSE TO ANTAGONIST1). RAN1 transports copper from the cytoplasm into presumably post-Golgi vesicles (Himelblau and Amasino, 2000). It has been shown that RAN1 is required for processing of the ethylene receptor ETR1 (ETHYLENE RESPONSE1; (Chang et al., 1993). ETR1 contains a copper ion required to bind its ligand ethylene and subsequently activate the ethylene hormone response pathway (Binder et al., 2010). Misprocessing of ETR1 constitutively activates ethylene responses which includes shortening of hypocotyl and root in etiolated seedlings. Also RAN1 mutants behave similar to an ETR1 loss-of-function mutant, defects in cell elongation were suggested to be regulated by a non-ethylene-dependent pathway (Woeste and Kieber, 2000). *In vivo* RAN1 was speculated to localise to post-Golgi vesicles (Himelblau and Amasino, 2000). If Ran1 co-localises with ClCd and ClCf, a role of Cl^- in charge balance or copper-loading on proteins similar to yeast could be possible. Therefore it would be worthwhile to test if ethylene response genes are upregulated in *clcd* amiR-*clcf.*

Furthermore, enzymes requiring copper are for instance multicopper laccases which polymerise lignin components to the final lignin polymer at the cell wall (Liang et al., 2006). A general misprocessing of copper-dependent enzymes could also affect lignin polymerisation or composition. In preliminary experiments we detected ectopic lignin deposition in induced *clcd* amiR-*clcf* roots. Analysis of lignin contend and composition in *clcd* amiR-*clcf* could give hints whether an alteration in lignin processing enzymes are present. Nevertheless, if ClCd and ClCf deliver intracellular Cl^- required for copper-dependent protein processing, we expect that proteins of other pathways are similarly affected when both ClCs are absent.

However, ectopic lignification was also observed as a response of reduced cellulose content in cell walls. *det3* which has a lower cellulose contend due restricted exocytosis of cellulose synthase complexes (CSCs) displays ectopic lignification of root cell walls (Luo et al., 2015; Caño-Delgado et al., 2003). CSCs are hetero-trimers of different isoforms of cellulose synthases (CesA) which are assembled in the Golgi stack (Zhang et al., 2016). In *clcd* amiR-*clcf,* the *trans*-Golgi cisterna was increasingly acidified (Figure 19). The suboptimal pH could affect CSC assembly or structure of CesA proteins altogether leading to an altered protein complex. Additionally, the major pectin component hemigalactuoran (HG) is synthesised in the Golgi apparatus. Pectins are cell wall matrix polysaccharides and major determinants of the cohesion,

adhesion, extensibility, porosity and electrostatic potential of plant cell walls (Anderson, 2016). Biosynthesis of HG out of galacturonic acid takes place in the *cis*- and *medial*-Golgi cisterns. Then, galacturonic acid components are linked to HG polymers, undergo maturation and are conveyed to the *trans*-Golgi side. Here methyl-esterification occurs (Zhang and Staehelin, 1992; Kim and Brandizzi, 2014) and HGs are finally secreted to the cell wall (Zhang and Staehelin, 1992; Wolf and Greiner, 2012). Dynamic de-methyl-esterification of hemigalactuoran enables cross-linking of two adjacent HG molecules via calcium (Ca^{2+}) thereby increasing cell wall rigidity. Low pectin esterification is associated with reduced cell wall extensibility (Wolf and Greiner, 2012). The more acidic *trans*-Golgi pH could alter pectin methyltransferase activity leading to overall lower HG methyl-esterification. As a result, low-methylesterified pectins could be secreted to the cell wall which would render HGs more accessible for Ca^{2+} crosslinking. This would effect a cell wall rigidification which disables the cells to elongate leading to the observed cell elongation defects in *clcd* amiR-*clcf*. It has also been suggested that enzymes responsible for pectin stability and degradation are co-processed with its substrate in the Golgi stack (Anderson, 2016). Also, the transit from Golgi pH to the acidic environment in the cell wall was proposed to alter solubility of HG and other matrix polymers (Anderson, 2016). If now pH is already altered during pectin processing in the Golgi stack misprocessed components are delivered to the apoplast in *clcd* amiR-*clcf* which could result is altered cell wall properties and composition.

Preliminary experiments suggested that a lower methyl-esterification state is present in induced *clcd* amiR-*clcf* root cells. Now, a detailed analysis of cell wall composition in root tips of *clcd* amiR-*clcf* plants is required to identify and quantify cell wall matrix composition. Therefore, antibodies directed against high- (JIM-7) and low- (JIM-5) methylesterified HG, as well as Ca^{2+} crosslinked HG (2F4) (Zhang and Staehelin, 1992) can give insights whether the main pectin component is influenced in *clcd* amiR-*clcf*.

In conclusion, cell elongation phenotypes of *clcd* amiR-*clcf* could be caused by a maturation defect of copper-dependent enzymes due to impaired copper loading. On the other hand cell elongation could be inhibited due to cell wall alterations probably increasing rigidification (Figure 25). It will be exciting to see which process is causing the main proportion of the phenotype or if both processes equally contribute to *clcd* amiR-*clcf* phenotypes.

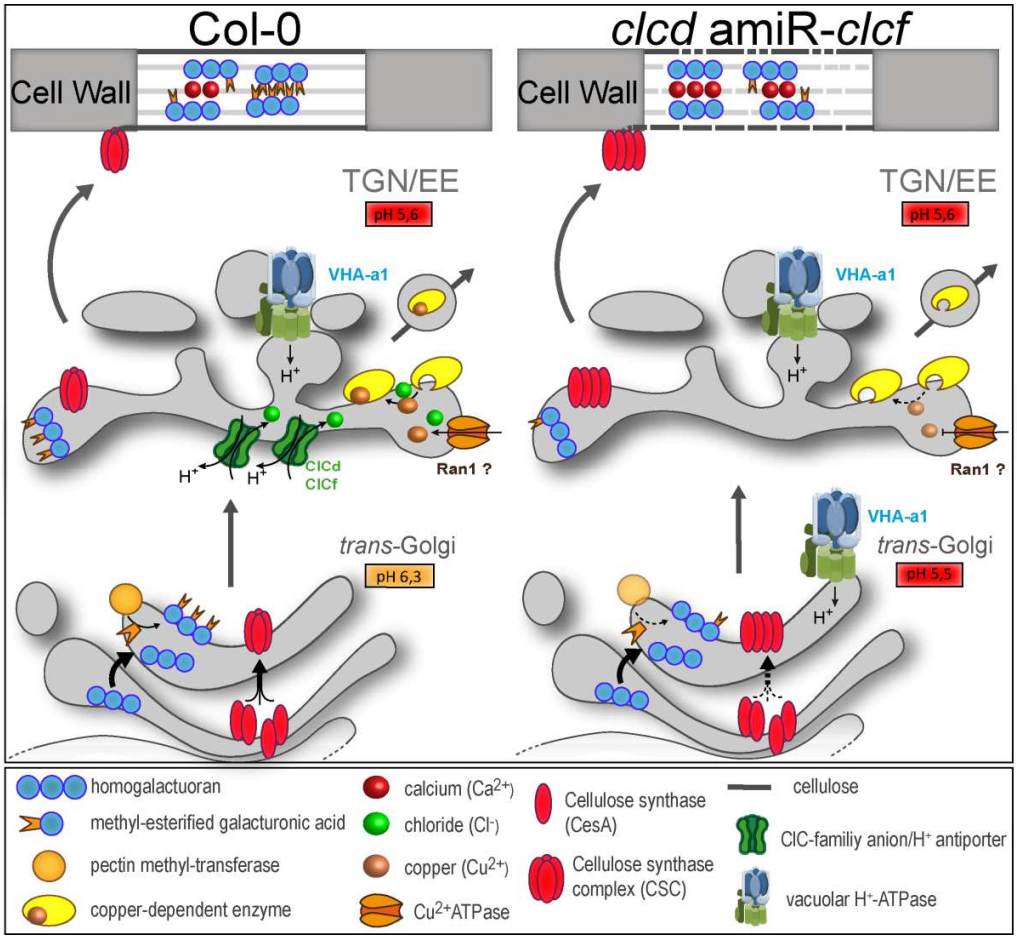

Figure 25: Current model of ClCd and ClCf functions in the TGN/EE and defects in *clcd* amiR-*clcf*. In Col-0 *trans*-Golgi pH is 6,3 and processes such as homogalactuoran (HG) methyl-esterification or CSC assembly function normally. Cl^- dependend copper (Cu^{2+}) loading on proteins or Cu^{2+} import might presumably be conducted at the the TGN/EE. Highly methyl-esterified HG and CSCs are secreted to the cell wall, where a dynamic de- and methyl-estrification takes place over growth an development. Demethyl-esterified homogalcturan can undergo calcium (Ca^{2+})-dependent crosslinking that increases cell wall rigidification. In *clcd* amiR-*clcf* the suboptimal *trans*-Golgi pH could lower pectin-methyltransferase acitvity or affect CSC assembly. Low methyl-esterified HG could therefore be more accessible for Ca^{2+} crosslinks. Furhtermore, alteration in CSCs could lead to a reducd cellulose content in the cell wall. The lack of luminal Cl^- in the TGN/EE would impair all Cu^{2+} import or loading processes.

3.3.5. Structural modeling and critical amino acids of ClCd and ClCf

ClC-proteins are a highly conserved family of Cl^- antiporters and channels present in all kingdoms of life with nearly identical structure (Accardi, 2015). By presence or absence of critical amino acids in the channel pore, predictions about anion selectivity as well as operation mode

can be made. Based on amino acid alignments, ClCd has been suggested to function as Cl^-/H^+ antiporter (von der Fecht-Bartenbach et al., 2007). ClCf was proposed to rather work as channel and to possess an atypical sequence for the anion selectivity filter region (Zifarelli and Pusch, 2010). However all predictions did not consider protein 3D structure and the localisation of the critical amino acids within the protein.

We therefore generated 3D structure models of both ClCd and ClCf and compared localisation of critical amino acids. Structures of both ClCd and ClCf were highly similar to the more ancestral eukaryotic CmClC from the red algae *Cyanidioschyzon merolae* (Feng et al., 2010). In ClCd we identified the presence of a "gating" glutamate 192 which is conserved in all ClC proteins (Accardi, 2015). Furthermore, a serine 149 and tyrosine 562 (both determining Cl^- specificity) was identified. The serine was located in the ClC "signature sequence" G**S**GIPG (Bergsdorf et al., 2009) and is well conserved among all Cl^- transporting ClC antiporters and channels, respectively (Accardi, 2015). Exchange of serine with proline alters preference from Cl^- to nitrate (NO_3^-) (Bergsdorf et al., 2009; Wege et al., 2010). The tyrosine coordinates with serine the dehydrated Cl^- via hydroxyl groups through the transporter pore (Miller, 2006). Together with a conserved "proton" glutamate 259 ClCd contains all amino acids necessary to function as Cl^-/H^+ antiporter. All ClC channels in mammals carry a valine residue at "proton" position (Accardi, 2015). Furthermore, these amino acids were located at identical positions as critical residues of ClC-ec1 and CmClC (Dutzler et al., 2003; Feng et al., 2010). It now remains to be experimentally tested, whether predictions for ClCd can be confirmed and currently efforts are made to electrophysiologically measure ClCd activity.

In ClCf only the "gating" glutamate 247 is conserved compared to all other ClC proteins. At the "proton" residue ClCf carries a tyrosine (T301) (Figure 23). This tyrosine can also be found in the Cl^-/H^+ antiporter CmClC (Feng et al., 2010) at the same position. Thus ClCf might function as well as anion/H^+ antiporter. Nevertheless, no clear assumptions which anion is likely to be transported by ClCf could be made. ClCf lacks the ClC "signature sequence" GSGIPG. Furthermore, the proposed selectivity filter region by Zifarelli and Pusch, 2010 is located at the protein periphery and is therefore unlikely to serve in anion binding. Based on localisation in the 3D model of ClCf, we identified glycine 192 at identical locations of serine/proline residues required for anion selectivity (Figure 23). This amino acid is not present in all other ClC proteins, except in the closely related ClCe transporter which forms a separate clade with ClCf (Zifarelli and Pusch, 2010). ClCe has already been associated with Cl^- homeostasis after dark-to-light transition but electrophysiological characterisation is lacking (Herdean et al., 2016). It remains to

be tested if glycine is able to bind Cl^-, probably by the partial positive amide backbone as this amino acids does not feature a residue. It also needs testing whether tyrosine 463 in ClCf serves in identical Cl^- stabilisation and guidance as in all other ClC proteins (Miller, 2006) despite its altered position compared to ClCd.

To experimentally determine ClCf activity another strategy has to be applied since we were not able to redirect ClCf to the tonoplast. Further redirection attempts could involve deletion of a putative TGN/EE retention motif in ClCf. A previously indentified TGN/EE retention motif in the N-terminus of VHA-a1 showed that an acidic amino acid cluster determines TGN/EE localisation (Dissertation Dr. Upendo Lupanga 2017). In our ClCa_ClCd-GFP tonoplast re-localisation construct, an acidic cluster in the ClCd N-terminus was partly disrupted. A similar cluster of acidic amino acids was identified between positions 108 and 119 in the ClCf sequence. Exchange of respective residues with uncharged amino acids might successfully relocate the protein to the tonoplast.

3.4. pH of the secretory pathway in *Arabidopsis thaliana*

In animal cells secretory pathway organelles become progressively acidified along the secretory route. Starting at pH 7,4 in the ER, pH in *cis*-Golgi cisternae is significantly lower (pH = 6,7) and systematically decreases down to pH 6,0 at the *trans*-Golgi network. In secretory granules luminal pH reaches pH 5,2 (Casey et al., 2010). In endocytic organelles pH systematically decreases from early endosomes (pH 6,3), late endosomes (pH 6,0) to highly acidic lysosomes (pH 5,5) (Paroutis et al., 2004; Casey et al., 2010).

We generated a toolset of pHusion-based pH sensors for compartments of the secretory pathway of *Arabidopsis thaliana* and conducted *in vivo* pH measurements. With these pH sensors and the data previously acquired for ER and vacuole we confirmed a similar progressive acidification of the secretory path in plants. pH in the ER is mildly alkaline (pH 7,6; Master Thesis Fabian Fink 2012) and on average 0,3 pH units different to the cytosol (pH 7,3). pH is with 6,7 at *cis*-Golgi cisternae higher than *trans*-Golgi cisternae (pH 6,3). Then, pH in the TGN/EE reaches pH 5,6 which is only minimally different to vacuolar pH (pH 5,8; Krebs et al., 2010). In the apoplast of the root elongation zone, pH of 5,4 was measured (Figure 26). However, we detected a pH gradient along the root tip which increases from meristem to early elongation zone and then systematically lowers with cell maturity and length. This data is in accordance to previous observations (Staal et al., 2011). Preliminary results also showed that apoplastic pH at apical and lateral cell sides could be different. For MVB/LEs, we were not able to find a protein located at inner MVB/LE vesicles.

The TGN/EE is the most acidic compartment of the secretory pathway and acidification is crucial for its functions (Luo et al., 2015). However, pH does not differ greatly between TGN/EE, cell wall and vacuole. This proposes that receptor-ligand interaction, which is an essential mechanism for targeted protein sorting and commonly dependent on pH, is controlled differently in plants. In mammalian cells receptor-ligand interaction is clearly dependent on organelle pH. For instance the mannosyl-6-phosphate receptor, that delivers acidic hydrolases to the lysosome, binds to its cargo at pH 6,3 in the TGN and releases at pH 6,0 to 4,8 during endosomal maturation (Huotari and Helenius, 2011). The receptor is then recycled to the TGN where it binds another cargo protein. In plants it was shown that soluble vacuolar proteins sorted by the VACUOLAR SORTING RECEPTOR4 (VSR4) bind their cargo already in the ER and separate again in the TGN/EE at pH 5,6 (Künzl et al., 2016). But how do endocytosed receptors at the plasma membrane separate from their ligands if pH in the apoplast and TGN/EE is not different? Cleary, ligand binding of all plasma membrane-localised receptors exposing their binding domains to the apoplast has to take place at acidic pH. After endocytosis the receptor-ligand complex is not exposed to a greatly different pH in the TGN/EE. Therefore, pH cannot control interaction which raises the question how these processes are regulated. It is unknown whether separation of receptor and ligand is mediated by another factor for instance luminal ion concentration or whether they separate at all. Instead of recycling, bound receptor-ligand complexes could be degraded and replaced by exocytosis of new receptor proteins. By adjustment of degradation and exocytosis rates, for instance in response to certain environmental stimuli, a dynamic re-arrangement of plasma membrane receptors could be achieved. The TGN/EE would then serve as a platform where trafficking rates of the different routes are measured and adjusted to the demands of the current environment.

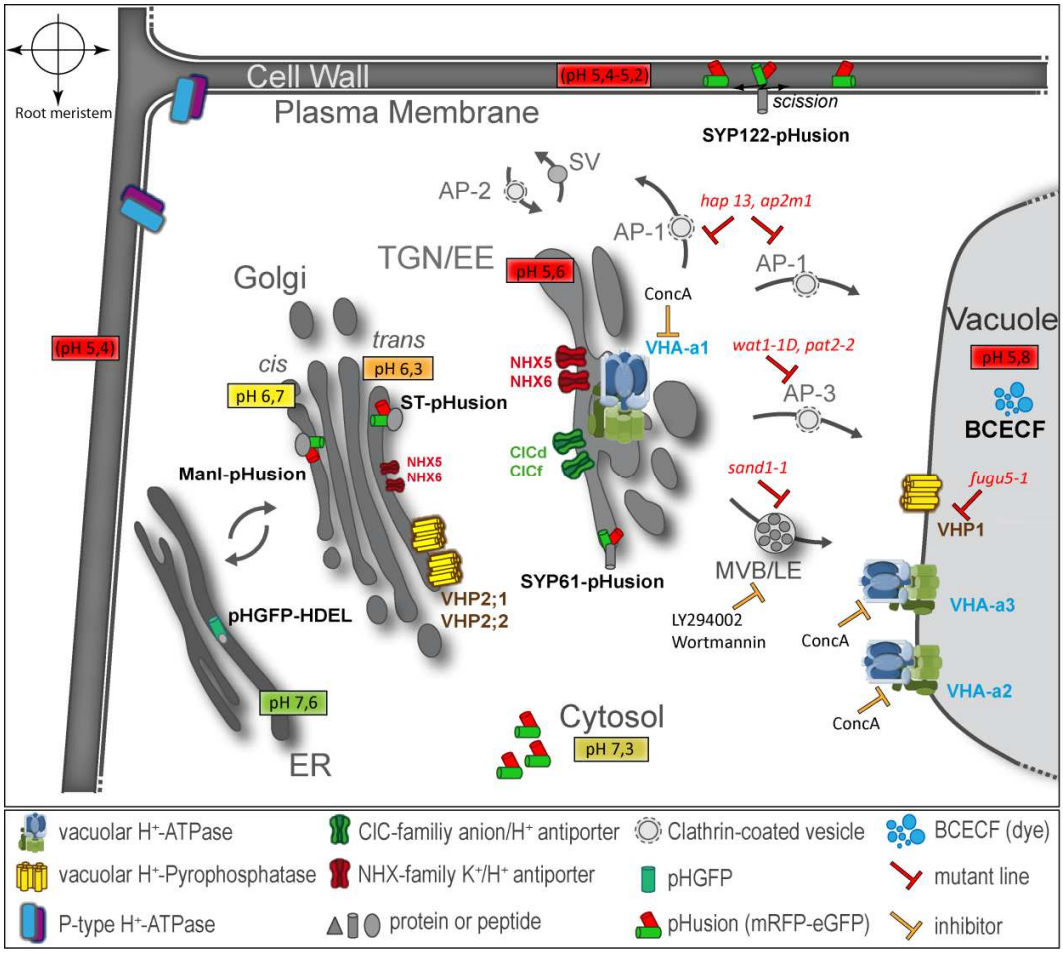

Figure 26: Determinants of pH in secretory pathway organelles and overview of compartment specific pH sensors. Generated compartment specific sensors and dyes are indicated in bold. All pH values, except pH values in brackets, are averages of three independent measurements of n=15 seedlings, measured after *in vivo* calibration in the respective compartment. Values in brackets are preliminary measurements. pHGFP-HDEL was generated and measured by Fabian Fink. Vacuolar pH: Krebs et al. 2010.

4. Conclusion

This work aimed to determine the *in vivo* TGN/EE pH in *Arabidopsis thaliana* which represents V-ATPase-mediated acidification to a large extend. Furthermore, we analysed TGN/EE to vacuole vesicular trafficking in respect to proton transport causing vacuolar acidification. Finally, this work addressed the function of ClCd and ClCf in supporting V-ATPase-mediated TGN/EE acidification by luminal charge balance. Initially, we established *in vivo* pH measurements in the TGN/EE of *Arabidopsis thaliana* seedlings using the genetically encoded pH sensor pHusion linked to the TGN/EE resident protein SYP61. Thereby, an *in vivo* steady state TGN/EE pH of 5,6 was measured, which is determined by the V-ATPase and H^+-coupled K^+ antiporter of the NHX family. TGN/EE pH of *det3* was 0,5 pH units more alkaline than WT which causes cell elongation defects. Unexpectedly, an inducible artificial micro RNA (amiR) specifically targeting VHA-a1 did result in acidification of the TGN/EE. The underlying cause of this pH decrease was not further addressed in this work. We were able to provide evidence that the V-ATPase is not responsible for Golgi stack acidification in plants, on the one hand. On the other hand, VHA-a1-containing V-ATPase activity significantly contributes to vacuolar pH probably via clathrin-coated vesicle pathways depending on AP-1 and AP-3 adaptor protein complexes. However, whether both pathways equally contribute to vacuolar acidification or whether interference with one pathway modulates other trafficking routes remains currently unknown. Finally, we verified progressive acidification along the secretory pathway reaching its lowest pH in the TGN/EE.

We showed that the ClC-family protein ClCf is located at the TGN/EE identically to ClCd. While a double knock-out caused male gametophyte lethality, an amiR-mediated knock-down demonstrated a crucial role of both ClCs in cell elongation. Nevertheless, knock-down of ClCf in *clcd* did not affect TGN/EE pH or TGN/EE-mediated trafficking. Instead, the *trans*-Golgi stack was substantially acidified due to a partial mislocalisation of the TGN/EE-localised V-ATPase to *trans*-Golgi cisternae. Therefore, further studies are required to elucidate whether cell elongation defects are caused by a lack of anions in the TGN/EE or by the altered *trans*-Golgi pH. *In silico* predictions proposed that both ClCd and ClCf operate as antiporter. However, clear predictions about anion preference were only made for ClCd, where chloride was proposed as the translocated anion. Consequently, electrophysiological measurements are required to reveal functions of ClCd and ClCf experimentally.

5. Material and Methods

5.1. Plant material and growth conditions

Following *Arabidopsis thaliana* T-DNA insertion lines and genetic backgrounds were used in this study:

Table 1: *Arabidopsis thaliana* wild-type and mutant lines used in this work.

Ecotype or line	Source/Reference
ap1m2-1	Park et al., 2013
Col-0 (Columbia-0) ecotype	Arabidopsis biological resource centre (ABRC, Ohio state university, OH)
clcd	von der Fecht-Bartenbach et al. 2007
***clcf* (SALK_112962)**	this work; purchased from SALK institute, San Diego, CA
det 3	Schumacher et al. 1999
hap13	Park et al., 2013
pat2-2	Feraru et al., 2010
sand1-1	Singh et al., 2014
wat1-1D	Niñoles et al., 2013
WS-4 (Wassilewskija) ecotype	Arabidopsis biological resource centre (ABRC, Ohio state university, OH)
vha-a2 vha-a3	Krebs et al., 2010

Arabidopsis thaliana seeds of every line and genotype were surface sterilised with 70% ethanol + 0,05% Triton X-100 for 30 min and afterwards 15 min with 95% ethanol. Seeds were dried on sterile filter paper and plated on half-strength (½) Murashige & Skroog (MS) medium (Duchefa); pH 5,8 (adjusted with KOH) and solidified with 0,4% phytoagar (Duchefa) unless stated otherwise. After 2 days stratification at 4°C and in darkness, plants were grown at long day (16h light/ 8h dark cycles) and equal light conditions (approximately 100 µE m^{-2} s^{-1}) for 6-7 days.

5.2. Cloning procedures

5.2.1. Cloning and construct generation by conventional cloning

All cloning procedures and DNA manipulations were performed according to standard and established protocols. Specification for primers used are listed in Table 2.

Backbone generation for overexpression *in planta* via P16 promoter. Overexpression of all constructs driven by the *P16 ribosomal promoter* (Schlücking et al., 2013) were based on the pTkan vector backbone (Hajdukiewicz et al., 1994; Schaaf et al., 2006). The 483 bp *P16 promoter* sequence was amplified via PCR out of a pP16Tkan plasmid (provided by Dr.

Christoph Neubert) with primers p16-KpnI-Fw and p16-KpnI-Rv, introducing two KpnI restriction sites flanking the sequence. This and all further PCR amplifications of fragments used for cloning were conducted in 50 µl total volume using “Phusion® High-Fidelity DNA-Polymerase” (Finnzymes) or "Q5® High-Fidelity DNA-Polymerase" (New England Biolabs) after manufacturers` protocol and 1 to 2 ng template DNA. Cycling conditions were chosen as suggested in the supplied protocol and 30 sec/1 kb were selected by default to calculate elongation time. PCR reactions were conducted in a “T3000 Thermocycler” (Biometra) or a “TProfessional Basic Gradient Cycler” (Biometra). After separation by agarose-gel electrophoresis stained with approx. 5 µg/ml ethidiumbromide, PCR fragments were cleaned from primers and salts with help of a “QuiaQuick® PCR Purification Kit” (Quiagen) or a "NucleoSpin® Gel and PCR Clean-up Kit" (Macherey-Nagel) according to the supplied protocol. PCR fragments were then subcloned into pJETblunt1.2 vector using the “CloneJET™ PCR cloning Kit” (Fermentas) after manufacturers` protocol. Subsequently, 5 µl of the ligation were transformed into DH5-α chemically competent *E.coli* cells (mod. after Hanahan, 1983) possessing the genotype F'φ 80ΔlacZΔM15 Δ(lacZYA-argF) U169 recA1 endA1 hsdR17(rk-, mk+) phoA supE44 λ -thi-1 gyrA96relA1. Transformed bacteria were plated on solid Luria-Both (LB) medium supplied with respective antibiotics (100 µg/ml) and grown over night at 37°C. Bacteria colonies were checked for inserts via colony PCR and positive clones were inoculated in 4 ml LB-medium containing 100 µg/ml of appropriate antibiotics. Plasmids were recovered using a “QuiaPrep® Miniprep Kit” (Quiagen) according to suppliers` protocol and insert presence as well as orientation was verified by restriction digest. After sequencing (Eurofins MWG Operon), correct fragment was cut out of the pJETblunt1.2 vector by digesting 2,5 µg plasmid DNA with KpnI (Fermentas) and ligated via “T4-Ligase” (Fermentas) into the pTkan vector (Schumacher lab), opened at the KpnI site and dephosphoryllated by “FastAP™" Thermosensitive Alkaline Phosphatase” (Fermentas) beforehand, to obtain pP16TKan(KpnI). By default, inserts were ligated in 3 M excess into 50 ng opened vectors; fragments below a size of 400 bp were applied in 4-5 M excess relative to applied vector amounts. Reaction was incubated at RT for 1h or at 4°C over weekend. 5 µl of each ligation were subsequently transformed into DH5-α cells as stated above, plated on solid LB medium with respective antibiotics and grown at 37°C over night. Correct P16 fragment orientation was verified by PCR and restriction digest. All further constructs were generated according to these principles.

P16$_{Pro}$:SYP61-pHusion. For *P16$_{Pro}$:SYP61-pHusion*, the full length *SYP61* CDS (At1g28490) was amplified from Arabidopsis Col-0 cDNA. In addition, 5 bp (CAACA) of a translation enhancer sequence were attached 5´of the start condon by primers SYP61-BamHI-fwd and SYP61-

HindIII[noSTOP]-rev. Stop codon was removed. *pHusion* pH sensor was extracted from 35S:pHusion plasmid (Gjetting et al., 2012) via PCR using pHusion-HindIII-fw and pHusion-SalI-rv primers. Fragments were sub-cloned into pJETblunt1.2 for sequencing and multiplication. After cutting with respective restriction enzymes, fragments were ligated into pP16Tkan vector via BamHI/SalI sites.

P16$_{Pro}$:pHusion-SYP61. *P16$_{Pro}$:pHusion-SYP61* was generated by amplifying *SYP61* with primers SYP61-HindIII-fwd and SYP61-SalI-rev, as well as *pHusion* (pHusion-BamHI-fwd/ pHusion[noSTOP]-HindIII-rev) from identical templates as used for *P16$_{Pro}$:SYP61-pHusion* generation. After subcloning and sequencing, correct fragments were removed from pJETblunt1.2 intermediate vectors with respective restriction enzymes and inserted into pP16TKan, pre-opened with BamHI and SalI.

UBQ10$_{Pro}$:SYP61-pHusion 2. To exchange the mRFP of pHusion with mCherry, *mCherry* sequence was amplified from a *mCherry-pJET* plasmid (Schumacher Lab) with primers mCherry-HindIII-fwd and mCherry[noSTOP]-Eco31I-rev introducing HindIII sites at 5` and a unique 4 bp overhang (TAAC) at 3`end. *eGFP* was received by PCR using *pHusion-pJET* as template and primers eGFP-Eco31I-fwd/ pHusion-SalI-rv which covered the full length *eGFP* sequence plus the 5 aa pHusion linker (AVNAS). Together with *SYP61* (cut with BamHI/HindIII; see: *P16$_{Pro}$:SYP61-pHus*ion), mCherry (HindIII/TAAC) and eGFP (TAAC/SalI) were ligated in pUTkan (Schumacher Lab), pre-opened with BamHI and SalI.

P16$_{Pro}$:ManI-pHusion. For *P16$_{Pro}$:ManI-pHusion*, the 1701 bp *α-Mannosidase I* (ManI) (At1g51590) CDS was amplified from Col-0 cDNA using primers ManI-AatII-fwd/ManI[noSTOP]-PvuI-rev. The stop codon was removed by the reverse primer. *pHusion* was received by PCR with primers pHusion-PvuI-fwd pHusion-SalI-rv from *P16$_{Pro}$:SYP61-pHusion* plasmid as template. After subcloning into pJETblunt1.2 and sequencing, *ManI* (AatII/PvuI) and *pHusion* (PvuI/SalI) fragments were ligated into pP16TKan, opened at AatII/SalI sites. Correct construct assembly was verified via test digest.

P16$_{Pro}$:ST-pHusion. *P16$_{Pro}$:ST-pHusion* was generated by PCR amplifying rat *Sialyltransferase* (ST) from a pre-existing *35S$_{Pro}$:ST-pHluorin* plasmid (Martinière et al., 2013a) by primers ST-AatII-fwd and ST[noSTOP]-PvuI-rev which also deleted the stop codon. PCR fragment was cloned in pJETblunt1.2 and correct sequence was verified by test digest and sequencing. Correct fragments were recovered by restriction digest and, together with *pHusion* (PvuI/SalI) (see: *P16$_{Pro}$:ManI-pHusion*), DNA-fragments were inserted in pP16TKan, pre-opened with AatII/SalI to receive *p16$_{Pro}$:ST-pHusion*.

UBQ10$_{Pro}$:ST-pHusion. *ST* and *pHusion* for *ST-pHusion* was identically cloned as described for *P16$_{Pro}$:ST-pHusion*. Cut fragments for *ST* (AatII/PvuI) and *pHusion* (PvuI/SalI) were finally inserted into pre-opened pUTbar (Schumacher Lab) vector (cut with AatII/PvuI) to generate *UBQ10$_{Pro}$:ST-pHusion*.

UBQ10$_{Pro}$:ClCf-mRFP. Full length coding sequence of *ClCf* (At1g55620) was amplified in a 2355 bp fragment without STOP codon from Arabidopsis Col-0 cDNA using primers ClCf-AatII-fwd and ClCf[noSTOP]-PvuI-rev. PCR fragment was subcloned into pJETblunt1.2 for sequencing and multiplication. *mRFP* was amplified form *pHusion(HindIII/SalI)-pJET* template using mRFP-PvuI-fwd/mRFP-SalI-rev. After removal out of pJETblunt1.2 with respective enzymes, both fragments were inserted in pUTkan and pUTbar, pre-cut with AatII and SalI.

P16$_{Pro}$:SYP61-e^{2}GFP-mRFP. To generate *e^{2}GFP* (Arosio et al., 2010), site directed mutagenesis of bp 610 (A to T) and bp 611 (C to A) of *eGFP* converting threonine 203 to tyrosine, was performed using primers eGFP-T203Y-fwd and eGFP-T203Y-rev with *pHusion(HindIII/SalI)-pJET* as template. Successful base exchange was verified by sequencing. The new "*e^{2}GFP-mRFP* " fragment was cut out by existing HindIII/SalI sites and together with *SYP61* cut by BamHI/HindIII, both fragments were inserted into pP16TKan, opened at BamHI/SalI sited via ligation.

5.2.2. Constructs generated using the Green Gate system

All following procedures and used plasmids were based on the GreenGate cloning system (Lampropoulos et al., 2013). To generate new entry modules, respective fragments were PCR amplified as stated above. Afterwards PCR reactions were supplemented with 5 µl "Fast Digest Buffer" (Fermentas) and 1µl Eco31I-HF (Fermentas) to open module specific overhangs in a restriction digest for 1h at 37°C. Fragments were then ligated in Eco31I-opened and purified entry vectors via T4-Ligase (Fermentas) in 3 M excess as indicated above.

For GreenGate reactions, all entry vectors were added in 1,5 µl volume independent of plasmid concentration. 100 ng of destination vector was applied in all GreenGate reactions. Plasmids were taken up in "Fast Digest Buffer" (Fermentas) supplemented with 100 µM Mg-ATP, 10 U Eco31I-HF (Fermentas) and 30 U T4-Ligase (Fermentas) in total 20 µl volume. Reactions were conducted in a thermocycler with 50 alternating cycles of 37°C and 16°C. Afterwards, 5µl of GreenGate were transformed in competent *E.coli*, bacteria were plated on solid LB medium with respective antibiotics and grown at 37°C over night. Correct assembly of fragments was confirmed via restriction digest.

UBQ10$_{Pro}$:SYP122-pHusion. Full length coding sequence of *SYP122* (Syntaxin of Plants 122; At3g52400) was amplified from *Arabidopsis thaliana* Col-0 cDNA with primers GG-SYP122-C-fwd and GG-SYP122-C-rev as "CDS" module without stop codon in a 1036 bp fragment. Fragment was cloned into pGGC000 for sequencing and multiplication before it was applied in a GreenGate reaction involving listed modules to obtain *UBQ10$_{Pro}$:SYP122-pHusion*.

"Promoter" Module	"N-Tag" Module	"CDS" Module	"C-Tag" Module	"Terminator" Module	"Resistance" Module	Destination Vector
pGGA-UBQ10	pGGB-N-decoy	GGC-SYP122	pGGD-pHusion	pGGE-rbcs	pGGF-Sulfadiazin	pGG-Z003
AG Lohmann	*AG Lohmann*	*This work*	*AG Schumacher*	*AG Lohmann*	*AG Lohmann*	*AG Lohmann*

UBQ10$_{Pro}$:ST-GFP. *ST* sequence was amplified from pre-existing *P16$_{Pro}$:ST-pHusion* plasmid using GG-ST-C-fwd and GG-ST-C-rev primers, sub-cloned in pGGC000 after Eco31I digest and finally sequenced to verify correct insert sequence. Ultimately, *pGGC-ST* was used in a GreenGate reaction to generate *UBQ10$_{Pro}$:ST-GFP* involving following modules:

"Promoter" Module	"N-Tag" Module	"CDS" Module	"C-Tag" Module	"Terminator" Module	"Resistance" Module	Destination Vector
pGGA-UBQ10	pGGB-N-decoy	pGGC-ST	pGGD-GFP	pGGE-rbcs	pGGF-Basta	pGG-Z003
AG Lohmann	*AG Lohmann*	*This work*	*AG Lohmann*	*AG Lohmann*	*AG Lohmann*	*AG Lohmann*

UBQ10$_{Pro}$:ClCd-GFP. For compatibility of *ClCd* with the GreenGate system, 2 internal Eco31I sites were removed from the wild type *ClCd* sequence. Furthermore, the entire sequence of *ClCd* Intron 1 was added due to lethal effects of the construct for bacteria. Additionally, bacteria were grown on NaCl- free LB medium due to insufficient growth on LB containing NaCl. For that purpose, 4 separate PCR reactions were performed: Firstly, with primers GG-ClCd-C-fwd/GG-ClCd-Int1-rev, a 86 bp fragment of the 5´region of *ClCd* was amplified from cDNA thereby exchanging 54 T to A (starting from "A" of ATG of the CDS) to remove the first Eco31I site. In a second PCR, a 518 bp fragment was amplified from Arabidopsis genomic DNA with primers GG-ClCd-Int2-fwd/GG-ClCd-Intron1-rev which contained *ClCd* bases 56 to 453 and full 94 bp of Intron 1. Thirdly, using primers GG-ClCd-Intron1-fwd/GG-ClCd-Int2-rev, bases 454 to 1732 were amplified in a 881 bp fragment and exchanged A with G at base position 1731 to remove a second Eco31I site. The last PCR of 677 bp product length was performed with primers ClCd-Int3-fwd/ClCd[noSTOP]-rev to amplify the *ClCd* 3´end and remove the stop codon. All PCR products were cut with Eco31I after PCR, ligated in pre-opened pGGC000 and transformed in

E.coli. Correct sequence assembly was monitored via sequencing. *pGGC-ClCd* was then applied in a standard GreenGate reaction to generate *UBQ10$_{Pro}$:ClCd-GFP*.

"Promoter" Module	"N-Tag" Module	"CDS" Module	"C-Tag" Module	"Terminator" Module	"Resistance" Module	Destination Vector
pGGA-UBQ10	pGGB-N-decoy	pGGC-ClCd	pGGD-GFP	pGGE-rbcs	pGGF-Hygromycin	pGG-Z003
AG Lohmann	*AG Lohmann*	*This work*	*AG Lohmann*	*AG Lohmann*	*AG Lohmann*	*AG Lohmann*

Dex:amiR-clcf. To determine optimal binding sequence of artificial micro RNA (amiR) against *ClCf* in the *ClCf* ORF the "WMD3" micro RNA design tool (Schwab et al., 2006) was used. Sequences with indicated hybridisation energy between "-35" and "-38" kcal/mole and binding site within the last third of the CDS were considered as candidates. A target sequence binding from bp 2928 to 2947 in the *ClCf* CDS was chosen and introduced by site directed mutagenesis in the miR319a precursor on a pRS300 plasmid (Prof. Dr. Detlef Weigel) as template using oligonucleotides amiR ClCf I, amiR ClCf II, amiR ClCf III, amiR ClCf IV according to providers` protocol (www.weigelworld.org). The amiR cassette was amplified in a 439 bp fragment using primers GG_amiR_FW_B_overhang_EcoRI/ GG_amiR_RV_C_overhang_BamHI. After digestion with Eco31I, amiR-*clcf* precursor was integrated in opened entry vector pGGI000. Plasmids were multiplied, sequenced and subsequently inserted into supermodule N via GreenGate reaction comprising following modules:

"Adaptor" Module	"Promoter" Module	"Bypass" Module	"Terminator" Module	"Resistance" Module	Destination Vector
pGGG-H-A adaptor	pGGA-6xOP	amiR-*clcf*	pGGE-rbcs	pGGF-Hygromycin	pGG-N000
AG Lohmann	*AG Lohmann*	*This work*	*AG Lohmann*	*AG Lohmann*	*AG Lohmann*

After successful assembly, 6xOP:amiR-*clcf* vectors were employed in a further GreenGate reaction to add the dexamethasone-inducible components.

"Supermodule A"	"Supermodule B"	Destination Vector
pGGM-UBQ10:Lh4GR	pGGN-6xOP:amiR-*clcf*	pGGZ003
AG Schumacher	*This work*	*AG Lohmann*

Vhp1$_{Pro}$:mClCf-GFP. To generate the amiR resistant *mClCf*, all bases differing from the wild type *ClCf* sequence were altered without changing amino acid order within the 20 bp amiR recognition site. Full m*ClCf* CDS without stop condon was then amplified in 2 separate reactions:

firstly with primers GG-ClCf-C-fwd/GG-mClCf-rev and secondly mClCf-fwd/GG-ClCf-C-rev in 1814 bp and 572 bp fragments using *UBQ10:ClCf-mRFP* as template. Both fragments were Eco31I digested, inserted into *pGGC000* and successful base exchange was confirmed by sequencing. Newly generated entry vector *pGGC-mClCf* was then assembled in a GreenGate reaction to receive the final *VHP1$_{Pro}$:mClCf-GFP* construct.

"Promoter" Module	"N-Tag" Module	"CDS" Module	"C-Tag" Module	"Terminator" Module	"Resistance" Module	Destination Vector
pGGA-Vhp1	pGGB-N-decoy	pGGC-mClCf	pGGD-GFP	pGGE-HSP18.2M	pGGF-Sulf	pGG-Z003
AG Schumacher	*AG Lohmann*	*This work*	*AG Lohmann*	*AG Lohmann*	*AG Lohmann*	*AG Lohmann*

***UBQ10$_{Pro}$:ClCa_ClCd-GFP*.** To PCR amplify the first 105 bp of *ClCa* (At5g40890), primers GG-ClCaNTerm-C-fwd and GG-ClCaNTerm-rev were used with Arabidopsis Col-0 cDNA as template. Corresponding *ClCd* sequence was PCR amplified in a 2278 bp fragment from pre-existing *pGGC-ClCd* (Eco31I sites removed) starting at aa 36 (corresponding to bp 106) without stop codon using primers GG-ClCdNtrunc-fwd and GG-ClCd[noSTOP]-C-rev. Both fragments were ligated in pGGC0000 after Eco31I digest, sequenced and afterwards assembled in a GreenGate reaction to obtain *UBQ10$_{Pro}$:ClCa_ClCd-GFP*.

"Promoter" Module	"N-Tag" Module	"CDS" Module	"C-Tag" Module	"Terminator" Module	"Resistance" Module	Destination Vector
pGGA-UBQ10	pGGB-N-decoy	pGGC-ClCa_ClCd	pGGD-GFP	pGGE-rbcs	pGGF-Basta	pGG-Z003
AG Lohmann	*AG Lohmann*	*This work*	*AG Lohmann*	*AG Lohmann*	*AG Lohmann*	*AG Lohmann*

***UBQ10$_{Pro}$:ClCa_ClCf-GFP*.** An N-truncated ClCf sequence, lacking the first 35 aa, was PCR amplified using primers GG-ClCfNtrunc-fwd/ GG-ClCf[noSTOP]-C-rev which resulted in a 2245 bp amplicon. The fragment was ligated into pGGC000 together with *ClCa* N-terminus (see: *UBQ10$_{Pro}$:ClCa_ClCd-GFP*),. After sequencing, a GreenGate reaction was performed to generate *UBQ10$_{Pro}$:ClCa_ClCf-GFP* using following entry vectors:

"Promoter" Module	"N-Tag" Module	"CDS" Module	"C-Tag" Module	"Terminator" Module	"Resistance" Module	Destination Vector
pGGA-UBQ10	pGGB-N-decoy	pGGC-ClCa_ClCf	pGGD-GFP	pGGE-rbcs	pGGF-Basta	pGG-Z003
AG Lohmann	*AG Lohmann*	*This work*	*AG Lohmann*	*AG Lohmann*	*AG Lohmann*	*AG Lohmann*

UBQ10$_{Pro}$:ClCd_Int1-GFP. To exchange the last 42 bp of *ClCd* with those of *INT1* (Inositole Transporter 1; At2g43330) a 2346 bp PCR fragment was amplified from *pGGC-ClCd* (Eco31I sites removed) using primers GG-ClCd-C-fwd and GG-ClCdCtrunc-rev. For insertion of *INT1* C-terminus, 50 µM of oligonucleotides Int1-CTerm[noSTOP]-fwd and Int1-CTerm[noSTOP]-rev were annealed by a temperature ramp of 5°C/30 sec to 37°C and phosphoryllated by "T4 Ligase" (Fermentas), afterwards. Prior to this procedure, an initial denaturation of 95°C for 5 min was conducted. Eco31I-digested *ClCd C truncated* fragment and phosphoryllated oligos were inserted in pre-opened pGGC000 via standard ligation. After sequencing, a GreenGate reaction was done to receive *UBQ10$_{Pro}$:ClCd_Int1-GFP*:

"Promoter" Module	"N-Tag" Module	"CDS" Module	"C-Tag" Module	"Terminator" Module	"Resistance" Module	Destination Vector
pGGA-UBQ10	pGGB-N-decoy	pGGC-ClCd_Int1f	pGGD-GFP	pGGE-rbcs	pGGF-Basta	pGG-Z003
AG Lohmann	*AG Lohmann*	*This work*	*AG Lohmann*	*AG Lohmann*	*AG Lohmann*	*AG Lohmann*

***UBQ10$_{Pro}$:ClCf_Int1-GFP*.** A 2311 bp fragment of ClCf lacking the last 42 bp was amplified from *UBQ10$_{Pro}$:ClCf-mRFP* as template with primers GG-ClCf-C-fwd/GG-ClCfCtrunc-rev. Fragment was digested with Eco31I and ligated in pGGC000 with annealed oligos of *Int1* C-terminus. *pGGC-ClCf_Int1* was sequenced, multiplied in *E.coli* and applied in a GreenGate reaction to generate *UBQ10$_{Pro}$:ClCf_Int1-GFP*.

"Promoter" Module	"N-Tag" Module	"CDS" Module	"C-Tag" Module	"Terminator" Module	"Resistance" Module	Destination Vector
pGGA-UBQ10	pGGB-N-decoy	pGGC-ClCf_Int1f	pGGD-GFP	pGGE-rbcs	pGGF-Basta	pGG-Z003
AG Lohmann	*AG Lohmann*	*This work*	*AG Lohmann*	*AG Lohmann*	*AG Lohmann*	*AG Lohmann*

5.2.3. Transformation of competent *Agrobacterium tumefaciens*

All constructs generated by conventional cloning were transformed into *Agrobacterium tumefaciens* strain GV3101:pMP90 featuring a rifampicin selection marker on the bacterial chromosome and a gentamicin resistance on T_i plasmid. All constructs generated with the GreenGate system were transformed into ASE strain which encodes for chloramphenicol resistance as chromosomal marker and kananmycin resistance for T_i plasmid selection. Additionally, ASE strain bacteria carry a pSOUP helper plasmid for replication of pGreen-based backbones which confer tetracycline resistance. Transformation procedure was identical for both

strains. Cells were unthawn at RT and mixed with up to 1 µg plasmid DNA. After brief and gentle suspension by tapping, bacteria were incubated on ice for 10 min. Immediately afterwards, a cold shock concluded for 5 min in $N_{2(l)}$ followed by incubation at 37°C for 5min. Then, bacteria were shaken at 28°C and 700 rpm in 800 µl LB medium for 3-4 h and plated on selective solid LB agar plates.

5.2.4. Stable transformation of *Arabidopsis thaliana*

All constructs described were used to generate stably expressing lines of *Arabidopsis thaliana* ecotype Col-0 and indicated mutants. For that purpose, 5 ml LB-medium supplied with appropriate antibiotics were inoculated with a single Agrobacterium colony harbouring the desired construct and grown over night at 28°C with continuous shaking (200 rpm). 500 µl of pre-culture were then used to start the main culture consisting of 200 ml LB plus antibiotics. After 18 h incubation at 28°C and 200 rpm, bacteria were pelleted at 5000 rpm and 4°C (“RC 5C Plus”, Sorvall), supernatant was discarded and pellet was resuspendend in 200 ml infiltration solution (5% Sucrose, traces of $MgSO_4$ and 0.05% Silvet L-77 (Lehe Seeds, USA)). This suspension was used to transform approx. 5 weeks old Arabidopsis plants via floral dip (Clough and Bent, 1998). Bolting plants with a large number of young, unopened flowers were briefly dipped in bacteria solution, covered with an autoclaving bag to maintain high humidity and placed at a light protected place for 24h. After that, plants were grown under long day conditions at 22°C.

Selection of transformed seeds was performed on sterile plant agar plates consisting of ½ MS, 0,5 % Sucrose, pH 5.8 and 0,5% phytoagar supplied with 100 µg/ ml antibiotics. Seedlings were grown for 6-8 days, resistant plants were transferred to soil and grown under long day conditions at 22°C.

5.3. Extraction of genomic DNA from *Arabidopsis thaliana* leaves

Leaf tissue of *Arabidopsis thaliana* ecotype Col-0, mutant lines *clcd*, *clcf* as well as respective complementation lines and F_1 plants of reciprocal crosses was homogenised with an Eppendorf pestle and genomic DNA (gDNA) was extracted via "Edwards` Buffer" (Edwards et al., 1991) with modifications. After debris removal via pelleting (13.000 rpm, 5 min) , gDNA was precipitated using 300 µl isopropanol (100%), followed by a washing step with 700 µl EtOH and centrifugation (5 min, 13.000 rpm). Isolated genomic DNA was vacuum dried and dissolved in 50 µl sterile *aqua bidest*.

5.4. Generation of cDNA from *Arabidopsis thaliana*

For transcript analysis, total RNA was extracted from entire leaves using the "RNeasy Plant Mini Kit" (Qiagen) after homogenisation with an Eppendorf pestle or mortar pre-cooled with $N_{2(l)}$. Afterwards, 1 µg of extracted RNA was transcribed in cDNA with help of "RevertAid™ H Minus M-MuLV Reverse Transcriptase" (Fermentas) according to manufacturers` protocol.

5.5. PCR-based genotyping of T-DNA insertions

1µl of extracted genomic DNA or cDNA (directly taken from preparations without dilution) was used in PCR-based genotyping of the SALK T-DNA line SALK_112962 (*clcf*), *clcd clcf* complementation lines and reciprocal crosses. Template was amplified together with 1x PCR-Buffer, 500 nM of forward and reverse primer, 250 µM desoxy-ribonucleotides and 0,4 µl of Taq Polymerase (out of own production) in 25 µl total volume. All PCR reactions were conducted with 35 cycles. Every reaction was executed twice to assure clear results.

5.6. Confocal laser scanning microscopy

Confocal laser scanning microscopy (CLSM) of Arabidopsis roots, leaves and protoplasts was performed on a "TCS SP5 II inverted Confocal Laser Scanning Microscope" (Leica) using a "HCX PL APO lambda blue 63.0x1,20 water immersion objective" (Leica) or a "HCX PL APO CS 20.0x0,70 IMM UV water immersion objective" (Leica). GFP was exited with the 488 nm, CFP with the 458 nm laser line of a "VIS-Argon laser" (Leica); for mRFP the 561 nm laser line generated by a "VIS-DPSS 561 laser" (Leica) was used for fluorophore excitation. Emission was detected at 460-530 nm for CFP, 500-545 nm for GFP and between 620-670 nm for mRFP using "HyD hybrid detectors" (Leica) in "Standard"-operation mode throughout all experiments. Images for non-quantitative purpose were processed in brightness and contrast using "Image J 1.51g" (National Institute of Health). All images were arranged with "Adobe Illustrator" (Adobe).

5.6.1. Inhibitor treatments

6 days old seedlings of indicated *Arabidopsis thaliana* transgenic lines were incubated in 24-well plates using liquid ½ MS, pH 5,8 (KOH) supplied with 20 µM Wortmannin (WM) (Sigma-Aldrich), 30 µM LY294002 (Sigma-Aldrich) or 50 µM Brefeldin A (BFA) (Sigma-Aldrich). As control, equal volume of DMSO was applied. Incubations for all inhibitors took place at RT and in the dark 1h prior to imaging.

Monensin A (Sigma-Aldrich) was applied in 5 µM concentration for 30 min identically as stated above with equal volumes of EtOH as control.

5.6.2. FM 4-64 staining

FM4-64 staining was performed in liquid ½ MS, pH 5,8 (KOH) with 1 µM FM 4-64 (Molecular Probes, Invitrogen) for 15 min. Seedlings were briefly washed in ½ MS, pH 5,8 (KOH) and imaged with CLSM using the 561 nm laser line for excitation and 670-750 nm range for emission detection.

For tonoplast labelling with FM 4-64, whole seedlings were incubated in 1 µM FM 4-64 dissolved in liquid ½ MS, pH 5,8 (KOH) for 30 min in the dark at 22°C. Afterwards, dye was removed and replaced by fresh ½ MS medium and seedlings were further incubated at identical conditions. Roots were imaged 100 min after FM 4-64 loading.

5.7. Quantitative measurements using confocal laser scanning microscopy

5.7.1. Co-localisation analysis

For co-localisation analysis, images of different roots zones of stably expressing Arabidopsis lines in T_2 or T_3 generation were taken using a “HCX PL APO lambda blue 63.0x1,20 water immersion objective” and "Hybrid Detectors (HyD)" in "Standard" mode on a "Leica SP5 II confocal laser scanning microscope". Resolution of 1024x1024 pixels with a zoom of 2,5x or a 512x512 pixel resolution with a 5,3x zoom was chosen to adjust a voxel size of 96 nm. CFP was excited at 458 nm and emission detected between 460-530 nm; GFP excited with 488 nm laser line and emission detected at 495-545 nm; mRFP was excited at 561 nm and detected at 610-670 nm. All microscope settings remained identical for each sample. For each line, 5 images of 10 independent seedling roots were taken. To determine maximum correlation coefficients of the current optical and experimental setup, 30 images of 10 µM TetraSpeck™ fluorescent microspheres with 1 µm or 500 µm size (Molecular Probes/Invitrogen) were taken. All images were processed in "ImageJ" using "Gaussian Blur Filter" with a "Sigma Radius" of 1,00. Pearsons` and Spearmans` correlation coefficients as well as scatterplots were calculated using the "PSC Colocalisation" plugin (French et al. 2008) with a threshold level of 10.

5.7.2. Manders` overlap coefficient determination

Manders` overlap coefficient between VHA-a1-GFP and FM 4-64 positive signals was calculated in 7 days old Arabidopsis roots stably expressing VHA-a1-GFP in Col-0, *clcd* or amiR-*clcf clcd* background (of T_2 or T_3 generations). After 4 days growth on 1/2 MS; pH 5,8; 0,4% phytoagar (Duchefa), seedlings were transferred to plates of the same medium supplied with 60 µM Dexamethasone (Dex) (Sigma-Aldrich) or plain medium as control. Plants were imaged 72h after Dex induction and after staining with 1 µM FM 4-64 in ½ MS; pH 5,8 (KOH) for 15min.

To determine Manders` overlap coefficient, images of 10 cells from 8-10 different root elongation zones per line and condition were taken with a “HCX PL APO lambda blue 63.0x1,20 water immersion objective”, a 512x512 pixel resolution and a zoom of 5,3x to receive a voxel size of 90,3 nm. GFP was exited using 488 nm laser line and emission was detected between 495-545 nm. FM 4-64 was exited at 561 nm and detected at 645-690 nm. Microscope settings were not changed while imaging all samples. Background was excluded with "ImageJ" using a "Gaussian Blur Filter" with a "Sigma Radius" of 1,00. By manual ROI selection, plasma membrane signal of FM 4-64 was excluded and subsequently, M1 and M2 Manders` overlap coefficients were calculated using the "JACoP" plugin (Bolte and Cordelières, 2006) with a threshold of 40 for both channels.

5.7.3. Quantification of average fluorescence intensities

Average intensities were determined in roots of 7 days old Arabidopsis T_3 plants expressing $UBQ10_{Pro}$:ClCf-mRFP or $Vhp1_{Pro}$:mClCf-GFP in *clcd* amiR-*clcf* backgrounds 3 days after amiR induction with 60 µM Dexamethasone (Dex) (Sigma-Aldrich). Plants were grown for 4 days on ½ MS; pH 5,8; 0,4% phytoagar (Duchefa) and afterwards transferred to identical medium as control or medium supplied with 60 µM Dex. Plants were further grown for 3 days at identical light conditions until imaging. Images were recorded with a "HCX PL APO lambda blue 63.0x1,20 water immersion objective". mRFP was excited using the 561 nm laser line and detected between 600 and 640 nm, GFP was exited at 488 nm and emission detected at 500-545 nm. For intensity measurements, images were evaluated in "Image J" with an automated macro (5.17.1.) excluding background signals by thresholding (a lower value of 20 was taken) and subsequently measuring the "mean grey value" of all pixels above threshold. Per line and condition, 15 images were taken in three independent replicates.

5.7.4. Measurement of TGN/EE size

Surface area measurements of TGN/EEs and TGN/EE clusters were performed in root epidermal cells of 7 days old Arabidopsis plants stably expressing $UBQ10_{Pro}$:SYP61-pHusion 2 in Col-0, *clcd* and *clcd* amiR-*clcf* background. Plants were grown on modified Johns` medium; pH 5,8; 5 mM MES-KOH solidified with 0,4% phytoagar for 4 days and then transferred to identical medium containing 60 µM Dex or plain medium as control. Plants were grown for 3 days after Dex or control treatment until images were taken with a "HCX PL APO lambda blue 63.0 x 1.20 UV water immersion objective" with a zoom factor of 5,5x and a pinhole size of 0,75 AU (= 83,7 µm). GFP channel images were used for size calculation. GFP was excited by the 488 nm laser line and detected at 500-545 nm. All further procedures were conducted in "Image

J". Average background value was determined on cytoplasmic and vacuolar areas (here 12,2) and subtracted from each image. Afterwards, a "Gaussian Blur Filter" with a "Sigma Radius" of 1,00 was applied and images were thresholded (30/255) to clear all unspecific background pixels. Particle size of parts, single TGN/EE or clusters was determined using the "Analyze Particles" function with parameters of 0,1-3,0 (in μm^2) for "Size" and 0,05-1,00 for "Circularity" where value 1 describes a perfect circle. Values were grouped according to area in "Microsoft Excel".

5.7.5. Determination of Golgi diameter

Images for Golgi diameter quantification were taken in root epidermal cells of 7 days old Arabidopsis lines Col-0, *clcd* and amiR-*clcf clcd* stably expressing $UBQ10_{Pro}$:ST-pHusion 72h after control or Dex treatment. Plants were grown on modified John´s medium; pH 5,8; 5 mM MES-KOH, solidified with 0,4% phytoagar. Documentation was performed with a "HCX PL APO lambda blue 63.0 x 1.20 UV water immersion objective", pinhole size of 1 AU (=111,5 µm) and 5,4x zoom. eGFP was exited at 488 nm and emission detected between 495- 545 nm. For size determination, diameter of Golgi stacks oriented parallel to the plasma membrane (in top or bottom view) were taken manually using the "straight line" tool in "Image J". Golgi stacks of 10 cells in10 individual roots were measured for each line and treatment.

5.7.6. Intracellular pH measurements using pHusion

Imaging setup. pH was determined in root cells of 6 or 7 days old T_2 and T_3-seedlings of all pHusion-based pH sensor lines. Imaging was done with a "HCX PL APO lambda blue 63.0 x 1.20 UV water immersion objective" using "HyD" detector operating in "Standard" mode. All channels, except those for free pHusion, were taken in single scans where eGFP was excited by 488 nm laser line and mRFP/mCherry was excited at 561 nm. Emission of eGFP was detected between 500-545 nm, mRFP between 620 to 670 nm or mCherry at 600-670nm. Signals of free pHusion were detected identically but in sequential scans to avoid spectral bleed-through. Pinhole and detector gain were adjusted according to signal and intensity of the respective sensor line but all imaging settings were kept constant for calibration and measurement of a sensor line.

***In vivo* calibration.** *In vivo* calibration was conducted by taking images of root epidermal cells of 6 to 7 days old seedlings after 15 min incubation in pH equilibration buffers. In calibrations of SYP61-pHusion /-pHusion 2, 1µM ConcA was added to calibration buffers before incubation. Buffers were composed out of 50 mM MES-BTP (Bis-tris-propane) (pH 5,2 to 6,4) or 50 mM

Hepes-BTP (pH 6,8 to 8,0) and 50 mM ammoniumacetate respectively. For calibration buffer pH 4,8 50 mM citrate buffer (22 mM Citric acid and 27 mM tri-sodium citrate; adjusted with HCl) and 50 mM Ammoniumacetate was used. To generate a calibration curve, pH values of applied calibration buffers were fitted against average ratios taken at the corresponding pH value using Origin Pro 9.1G (originlab.com).

Data evaluation. Images were thresholded to remove background and oversaturated pixels in "Image J". Threshold values were determined on the mRFP/mCherry channel for each sensor and kept constant for calibration and respective measurements. According to threshold values, a selection mask was generated on mRFP/mCherry signal above threshold and transferred to the respective eGFP channel image. Mean grey values within selection masks were taken for eGFP and mRFP/mCherry individually. All operations described were done automatically with an Image J macro (5.17.2.). Finally, eGFP/mRFP or eGFP/mCherry ratios were calculated in "Microsoft Excel". For all measurements, images of 15 independent seedlings were taken in three biological replicates. For calibration n=15 seedlings per pH value were imaged and measured.

5.7.7. Time-course measurement of $P16_{Pro}$:SYP61-pHusion ratios

For measurements of SYP61-pHusion ration over time, 6 days old Arabidopsis seedlings stably expressing $P16_{Pro}$:SYP61-pHusion were transferred to custom made imaging chambers connected to a peristaltic pump as described in Keinath et al., 2015. Identical settings as for standard TGN/EE pH measurements were applied (see 5.7.6). A 5 min baseline in ½ MS; pH 5,8 was taken, before treatment with pH equilibration buffers. Data was evaluated as described in 5.7.6.

5.7.8. pH measurements in SYP61-pHusion positive particles

Ratios of individual, SYP61-pHusion positive particles were taken in root epidermal cells of 7 days old Arabidopsis plants. Images were taken as described in section 5.7.6. with settings for pHusion or pHusion 2 with a HCX PL APO lambda blue 63.0 x 1.20 UV water immersion objective" with a zoom factor of at least 5,5x a pinhole size of 0,75 AU (= 83,7 µm). All further procedures were conducted in "Image J" with an automated macro (5.17.3). A "Mean" filter with a "radius of 2" was applied for background subtraction. Then images were thresholded (here: 30/255) and particle size of parts, single TGN/EE or clusters was determined using the "Analyze Particles" function with parameters of 0,05-3,0 (in μm^2) for "Size" and 0,03-1,00 for "Circularity". Particles in the mRFP/mCherry channels were used to create a selection mask which was

transferred to the eGFP channel. Intensity of both channels were taken and eGFP/mRFP or mCherry ratios were calculated in "Microsoft Excel". The final box plots were generated with "Origin Pro".

5.7.9. Measurement of vacuolar pH

Vacuolar pH was determined in root epidermal and cortex cells in differentiation zones of 6 days old seedlings using the pH sensitive fluorescent probe BCECF-AM (2',7'-Bis-(carboxyethyl)-5(6)-carboxyfluoresceinacetoxymethylester) (Molecular Probes, Invitrogen). Loading and measurements were performed as described in Krebs et al., 2010. Entire seedlings were stained with 10 µM BCECF-AM in presence of 0.02 % Pluronic F-127 (Molecular Probes, Invitrogen) for 1 h in the dark at RT and washed 2x 5 min with liquid MS medium prior to imaging. *In vivo* calibration was done as described above with pH equilibration buffer pH 5,2 to 8,0.

Measurements were done using a "HCX PL APO CS 20.0x0,70 IMM UV" water immersion objective. BCECF was excited with 458 nm and 488 nm laser lines in sequential scans. Emission was detected between 510 and 550 nm. Image evaluation was identically performed as described above using the same "Image J" macro (5.17.2.).

5.7.10. FLIM-FRET measurements

All FLIM-FRET measurements were done at a "TCS SP5 II inverted Confocal Laser Scanning Microscope" provided with a "PicoHarp 300 TCSPC" (PicoQuant). Detection was performed on a FLIM-PMT (Hamamatsu) installed in the system. Lifetime images were recorded in transition zone cells of 6 days old Arabidopsis roots of T_2 or T_3 seedlings with a "HCX PL APO lambda blue 63.0 x 1.20 UV water immersion objective" at 256 x 256 pixel resolution. eGFP donor was exited at 470 nm by a "PDL-800B" pulsed diode laser (PicoQuant) at 20 MHz repetition rate with an average photon count of 400-600 photons. eGFP donor emission was detected between 490 and 500 nm until 1000 photons were collected. Image analysis and calculation of eGFP lifetime was performed using "SymPhoTime" software (PicoQuant). Florescence decay curve was thresholded by 110/300 while fitted with a bi-exponential function. 15 seedlings per line were measured in three independent measurements.

5.8. Super resolution microscopy

For ratio images of single TGN/EEs, Z-stacks of root epidermal cells were taken in 6 days old Arabidopsis seedlings stably expressing $UBQ10_{Pro}$:SYP61-pHusion 2 on a "Zeiss LSM 800 confocal laser scanning microscope" (Zeiss) with a "Plan-Achromat 63x/1.4 Oil DIC M27 oil immersion objective" (Zeiss). Both fluorophores were excited line by line where eGFP was

irradiated by a 488 nm diode laser and mCherry by a 561 nm Laser diode. Emission was recorded at 495-545 nm for eGFP and 600-640 for mCherry in "Airyscan Processing" mode. All further image evaluation was done using "Image J". Single cells were extracted by "Rectangular Selection" tool and background intensities of both channels were taken from cytoplasmic signals within the same area. After background subtraction, images were converted to 32-bit and a "Gaussian Blur Filter" with a "Sigma Radius" of 1,00 was applied. Afterwards, a threshold of 25 was employed constantly to all images and channels. Lastly, ratio images were created by dividing eGFP with mCherry images using "Image calculator" operation. 5 independent roots were recorded and ratio images of at least three cells per root evaluated.

5.9. Electron microscopy

5.9.1. High pressure freezing and freeze substitution

Entire root tips of 6 days old Arabidopsis seedlings stably expressing P16:SYP61-pHusoin or $UBQ10_{Pro}$:ClCf-mRFP were cut and transferred to aluminium planchettes pre-filled with freezing solution (6,8 g sucrose, 0,34 g trehalose in 10 mM TRIS, pH=6,6). high pressure freezing was performed in a “Bal-Tech HPM 010” (Balzers Union AG) high pressure freezer. Concluding freeze substitution was done in a “Leica EM AFS 2” (Leica). Therefore, samples were incubated in 0,3% uranyl acetate in anhydrous acetone for 21h at -85°C and washed with 100%EtOH for 1h at -85°C. Root tips were embedded in lowicryl resin (HM-20) solved in absolute ethanol in 30%, 50%, 75% and 100% steps for 1h each at -85°C. Finally, root tips were transferred to embedding molds and UV-polymerisation was done at -50°C for 36h.

5.9.2. Immunogold labeling

Ultrathin sections of 80 – 90 nm were obtained using a “Leica Ultracut S” (Leica) ultra microtome with a diamond knife (DiAatome), stretched with chloroform and mounted on 100 hexagonal-mesh copper grids covered with a formvar film (0,6% polyvinyl formaldehyde in chloroform). Grid-mounted sections were blocked with 3% BSA in PBS for 15 min. Subsequently, sections of $P16_{Pro}$:SYP61-pHusion were incubated with and α-GFP antibody diluted 1:1000 and specimens of $UBQ10_{Pro}$:ClCf-mRFP were labelled with an α-DsRed antibody in 1:200 dilution. After 4 washing steps with 1% BSA in PBS, grids were incubated with a goat anti-rabbit (1:50 with 1% BSA in PBS) antibody linked to 10 nm colloidal gold particles for 1h. Afterwards, sections were washed twice with 1% BSA in PBS (5 min each) followed by three washing steps with *aqua bidest* (5 min each).

5.9.3. Transmission electron microscopy

Immunolabelled sections were observed with a “JEOL JEM-1400“ (JEOL, Tokio, Japan) electron microscope operating at 80 kV. Micrographs were taken with a TVIPS FastScan F214 digital camera (Gauting). Brightness and contrast was adjusted using "Image J" or "Adobe Photoshop".

5.10. Preparation and transfection of Arabidopsis mesophyll protoplasts

Mesophyll protoplasts were prepared according to Yoo et al., 2007 out of approximately 4 weeks old *Arabidopsis thaliana* Col-0 rosette leaves grown at long day conditions. 20 rosette leaves were cut in 1 mm leaf strips and immediately covered with 10 ml "enzyme solution" in a round Petri dish. Leaf strips were vacuum infiltrated for 30 min and afterwards digested for at least 3h at room temperature and in darkness with moderate shaking. Subsequently, solution was filtered with help of a "70 µm EASYstrainer" cell strainer (Greiner Bio One) to remove cell and leaf debris. Filtrate was collected in 50-ml round-bottomed centrifuge tubes pre-filled with 10 ml "W5 solution" and protoplasts were pelleted at 100 g, 22°C, 2 min in an "5804 R centrifuge" (Eppendorf). Supernatant was removed and pellet was resuspendend in remaining solution by gentle shaking. Afterwards, cells were resuspendend in 4 ml "W5 solution" to adjust an approximate concentration of 2 x 10^5protoplasts ml^{-1} and collected by settling for 30 min on ice. Then, supernatant was discarded, pellet was resuspendend in 2,5 ml "MMG solution" and protoplasts were stored at room temperature until subsequent transfection.

To transfect prepared protoplasts, 10 µl of desired plasmid DNA (approx. 10-20 µg) were added in a 14ml microfuge tube (Greiner) and 100 µl protoplasts (around 2x10^4cells) were pipetted on top and mixed by tapping. To the DNA/protoplast suspension, 110µl of "PEG transfection solution" was carefully added and immediately mixed by inversion. After 10 min incubation at room temperature, 450 µl "W5 solution" was supplied, carefully mixed by inversion and spun down at 100g and room temperature. Finally, supernatant was discarded and protoplasts were resolved in remaining supernatant. For recovery, protoplasts were taken up in 1 ml "WI solution" in a 6-well plate and stored at room temperature (23°C) in the dark. Construct expression was observed 2 days after transfection using a confocal microscope.

5.11. Concanamycin A hypersensitivity assay

All seeds of *Arabidopsis thaliana* Col-0 or mutant/transgenic lines were surface sterilized as stated above and plated on medium consisting of 1% phytoagar (Duchefa); 5 mM MES-KOH (adjusted to pH 5,8). To the medium 100 nM Concanamycin A (Santa Cruz Biotechnology) or

equal volume of DMSO was added. Seeds were stratified at 4°C for 2 days and afterwards double wrapped with aluminium foil for etiolation at 22°C for 5 days.

For hypocotyl length measurements, etiolated seedlings were positioned between transparent foil and documented with a commercial scanner. A 1 cm scale bar was added to every sample. Hypocotyl-length was measured with "Image J". Scale was defined by the applied 1 cm scale bar using the “Straight-Line” tool; root and hypocotyl lengths were determined using “Segmented Lines”. For every inhibitor concentration as well as controls, n=30 seedlings were measured and average values were calculated.

5.12. Hypocotyl length measurements of *clcd* amiR-*clcf*

Seeds of *Arabidopsis thaliana* Col-0 or mutant/transgenic lines were sterilized as stated above and sown on a sterile polyamide mesh of 100 µm mesh size fitted to a 145 x 20 mm Petri dish. Meshes were placed on 14 ml medium consisting of double-distilled H_2O; 5mM MES-TRIS (pH 5,8). For each condition, liquid medium was supplied with 30 µM Dex (Sigma-Aldrich) or equal amounts of DMSO. Plates were sealed with parafilm and stratified for 2 days at 4°C. Afterwards, plates were double-wrapped in aluminium foil and etiolated for 4 days at 22°C. Hypocotyl length was measured as stated above.

5.13. Measurement of root length and root zones

All *Arabidopsis thaliana* seeds were surface sterilized as stated above and plated on ½ MS, pH 5,8 (KOH), 1% phytoagar (Duchefa) or modified Johns` medium, 5mM MES-TRIS with varying pH values. Seeds were grown for 3 to 4 days, transferred to rectangular, vertical plates and further grown at identical light conditions for in total 7 or 12 days. Root length was measured as stated in 5.12.

For length measurements of root meristematic and elongation zone, plants were pre-grown on ½ MS, pH 5,8 (KOH) 0,4% phytoagar for 4 days and then transferred to identical medium containing 60 µM Dex or ½ MS, pH 5,8 (KOH), 0,4% phytoagar as control. Plants were further grown for 3 days after Dex or control treatment and then stained with 300 µm/ml propidium iodide for 1 min. After brief washing in fresh liquid ½ MS, pH 5,8 (KOH), images of entire root tips were taken with a "HCX PL APO CS 20.0x0,70 IMM UV” objective on a "TCS SP5 II" confocal laser scanning microscope (Leica). The dye was excited with the 561 nm laser line and emission detected between 610 - 655 nm. Length of root zones was measured using "Image J" with “Segmented Lines” tool. For each line and condition, 10 individual roots were measured.

5.14. Quantification of seed phenotypes

Mature siliques of Arabidopsis ecotype Col-0 and mutant lines *clcd*/+ *clcf*, both grown at long day conditions, were opened along the seed valves from base to tip and seeds were categorised according to shape and size under a "Zeiss SteREO Discovery V20" (Zeiss) stereo microscope. For each genotype, seeds of 10 siliques were counted.

5.15. Primers used in this study

Table 2: Primers used for construct generation. Bases in highlighted in bold comprise restriction enzyme recognition sites, underlined bases mark Eco31I cutting sites.

Gene	Alias	Internal Accession	Sequence (5´to 3´)	Tm [°C]	Generated by
α-Mannosidase I	ManI-AatII-fwd	KS-q2384	TGT**GACGTC**ATGGCGAGAAG TAGATCGAT	67,2	Stefan Scholl
	ManI[noSTOP]-PvuI-rev	KS-q2385	TGT**CGATCG**CCCAACGTTAA TCTGATGACCAA	69,4	Stefan Scholl
amiR-*clcf*	amiR-clcf I	KS-q2415	GATATTATGGTCAGGGTTCG CTATCTCTCTTTTGTATTCC	64,5	Stefan Scholl
	amiR-clcf II	KS-q2416	GATAGCGAACCCTGACCATA ATATCAAAGAGAATCAATGA	63,5	Stefan Scholl
	amiR-clcf III	KS-q2417	GATAACGAACCCTGAGCATA ATTTCACAGGTCGTGATATG	65,5	Stefan Scholl
	amiR-clcf IV	KS-q2418	GAAATTATGCTCAGGGTTCG TTATCTACATATATATTCCT	61,4	Stefan Scholl
	GG_ami_FW_B_overhang_EcoR1	KS-q2336	AACA**GGTCTC**AAACACGAAT TCCTGCAGCCCC	65,7	Falco Krüger
	GG_ami_RV_E_overhang_BamH1	KS-q2337	AACA**GGTCTC**TGCAGGGATC CCCCCATGGCGATGCC	72,4	Falco Krüger
ClCd	GG-ClCd-C-fwd	KS-q2609	AACA**GGTCTC**AGGCTCAACA ATGTTATCGAATCATCTCCA	65,5	Stefan Scholl
	GG-ClCd-Int1-rev	KS-q2633	AACA**GGTCTC**AGTGACCAGA GTAGGTTATCGGATT	64,4	Stefan Scholl
	GG-ClCd-Int2-fwd	KS-q2679	AACA**GGTCTC**TTCACGTGTC CCTGAATCCGATGAT	65,6	Stefan Scholl
	GG-ClCd-Int2-rev	KS-q2680	AACA**GGTCTC**AGCCTCGATT CAAGTAACGGAATGC	65,6	Stefan Scholl
	GG-ClCd-Intron1-fwd	KS-q3564	AACA**GGTCTC**TCATTCCTGA GATTAAGGGTTATCTC	63,3	Stefan Scholl
	GG-ClCd-Intron1-rev	KS-q3563	AACA**GGTCTC**TAATGCCAGA ACCAGCAGCAGCA	65,6	Stefan Scholl
	GG-ClCd-Int3-fwd	KS-q2681	AACA**GGTCTC**AAGGCCTAAG TATCACATGCGTCAA	64,4	Stefan Scholl
	GG-ClCd[noSTOP]-C-rev	KS-q2610	AACA**GGTCTC**TCTGATGAAC CTAAAAGATCGTCTA	62,1	Stefan Scholl
	GG-ClCdNtrunc-rev	KS-q3169	AACAGGTCTCTGAGATCTCA CCGTGACGGTGACGGAGGT	69,2	Stefan Scholl
	GG-ClCdCtrunc-rev	KS-q3153	AACA**GGTCTC**TAGAACCGCG TTGCTGTCTCACT	71,5	Stefan Scholl
ClCf	ClCf-AatII-fwd	KS-q2274	TGT**GACGTC**ATGTCATCGGG AGGAGCCGGAGAG	67,5	Stefan Scholl
	ClCf[noSTOP]-PvuI-rev	KS-q2275	TGT**CGATCG**TCCATGCCCAT TTGTACCAACCTC	63,2	Stefan Scholl
	GG-ClCf-C-fwd	KS-q2230	TGT**GGTCTC**AGGCTATGTCA TCGGGAGGAGCCGG	70,5	Stefan Scholl

Table 2 (continued)

Gene	Alias	Internal Accession	Sequence (5´to 3´)	Tm [°C]	Generated by
	GG-ClCf-C-rev	KS-q2229	TGT**GGTCTC**ACTGATCCATG CCCATTTGTACCAA	75,3	Stefan Scholl
	GG-mClCf-fwd	KS-q3211	TGT**GGTCTC**ATCCAGATCAC AACTCCTTTTTGGATG	69,2	Stefan Scholl
	GG-mClCf-rev	KS-q3212	TGT**GGTCT**CATGGATTTTCGA TGACGGTAAGCTCAA	70,2	Stefan Scholl
	GG-ClCfNtrunc-rev	KS-q3171	ACA**GGTCTC**AGAGAGAATCT CAGTCTCCGGC	69,6	Stefan Scholl
	GG-ClCfCtrunc-rev	KS-q3154	AACA**GGTCTC**TAGAAGTCGT TGATCGATCTCCTACGAC	66,6	Stefan Scholl
eGFP	eGFP-Eco31I-fwd	KS-q2199	TGT**GGTCTC**ATAACGCTAGC ATGGTGAGCAAGGGCGAGG A	70,6	Stefan Scholl
	eGFP-T203Y-fwd	KS-q2607	AACCACTACCTGAGCTACCA GTCCGCCCTGAG	72,8	Stefan Scholl
	eGFP-T203Y-rev	KS-q2608	CTCAGGGCGGACTGGTAGCT CAGGTAGTGGTT	72,8	Stefan Scholl
Int1	Int1-CTerm[noSTOP]-fwd	KS-q3155	AACAACATGGAAGGGTTACT CGAGCAGGGATCTCAATCTG AA	-	Stefan Scholl
	Int1-CTerm[noSTOP]-rev	KS-q3156	CTGATTCAGATTGAGATCCCT GCTCGAGTAACCCTTCCATG T	-	Stefan Scholl
mCherry	mCherry-HindIII-fwd	KS-q2400	TCT**AAGCTT**ATGGTGAGCAA GGGCGAGGAGG	66,6	Stefan Scholl
	mCherry[noSTOP]-Eco31I-rev	KS-q2195	TGT**GGTCTC**AGTTAACGGCT AACTTGTACAGCTCGTCCA	67,6	Stefan Scholl
mRFP	mRFP-PvuI-fwd	KS-q2276	TGT**CGATCG**ATGGCCTCCTC CGAGGACGTCATC	67,7	Stefan Scholl
	mRFP-SalI-rev	KS-q1776	**GTCGAC**TTAGGCGCCGGTG GAGTGGC	67,7	Stefan Scholl
P16	p16-KpnI-Fw	KS-q1842	GAG**GGTAC**CTGGAACCATCT TTTGGGTTCCTTTC	63,3	Dr. Melanie Krebs
	p16-KpnI-Rv	KS-q1843	GAT**GGTAC**CCCACGCCGTCG TAGATGAGAAACCC	67,1	Dr. Melanie Krebs
pHusion	pHusion-HindIII-fw	KS-2103	AAC**AAGCTT**ATGGCCTCCTC CGAGGACG	64,3	Dr. Melanie Krebs
	pHusion-SalI-rv	KS-2104	GTTGTCGACTTACTTGTACAG CTCGTCCATGCC	65,6	Dr. Melanie Krebs
	pHusion-BamHI-fw	KS-q2107	AAC**GGATCC**AACAATGGCCT CCTCCGAGGACG C	68,2	Dr. Melanie Krebs
	pHusion[noSTOP]-HindIII-rev	KS-q2108	GTT**AAGCTT**CTTGTACAGCT CGTCCATGCCGTGAGT	66,7	Dr. Melanie Krebs
Sialyl-transferase	ST-AatII-fwd	KS-q2382	CGGT**GACGTC**ATGATTCATA CCAACTTGAAGAAA	67,0	Stefan Scholl
	ST-PvuI-rev	KS-q2383	TGT**CGATCG**CATGGCCACTT TCTCCTGGC	72,0	Stefan Scholl
	GG-ST-C-fwd	KS-q2634	AACA**GGTCTC**AGGCTCAACA ATGATTCATACCAACTTGAA	64,5	Stefan Scholl
	GG-ST-C-rev	KS-q3635	AACA**GGTCTC**TCTGACATGG CCACTTTCTCCTGGC	67,9	Stefan Scholl
SYP61	SYP61-BamHI-fwd	KS-2099	AAC**GGATCC**AACAATGTCTT CAGCTCAAGATCC	63,2	Dr. Melanie Krebs
	SYP61-HindIII-fwd	KS-2111	AAC**AAGCTT**ATGTCTTCAGCT CAAGATCCATTCTACAT	62,3	Dr. Melanie Krebs
	SYP61[noSTOP]HindIII-rev	KS-2100	GTT**AAGCTT**GGTCAAGAAGA CAAGAACGAATAGGATG	63,3	Dr. Melanie Krebs
	SYP61-SalI-rev	KS-2112	GTT**GTCGAC**TTAGGTCAAGA AGACAAGAACGAATAGGATG	65,5	Dr. Melanie Krebs
SYP122	GG-SYP122-C-fwd	KS-q2746	ACA**GGTCTC**AGGCTCAACAA TGAACGATCTTCTCTCC	66,7	Stefan Scholl
	GG-SYP122-C-Rev	KS-q2747	ACA**GGTCTC**TCTGAGCGTAG TAGCCGCCGATT	67,0	Stefan Scholl

Table 3 : Primers used for PCR-based genotyping.

Gene	Alias	Internal Accession	Sequence (5´to 3´)	Tm [°C]	Generated by
Actin2	ActinRV	KS-P460	GAGGGCTGGAACAAGACTTC	53,8	Dr. Esther Jawurek
	ActinFW	KS-P461	TCCAAGCTGTTCTCTCCTTG	51,8	Dr. Esther Jawurek
ClCd	ClC**d-rev**	KS-P971	CTCCGATAACTCCTATTACAGC	53,0	Dr.Tsu-Yin Liu
	ClC**d-fwd**	KS-P972	CCCGGCACCTTGCTCTTTAGAAC	58,8	Dr.Tsu-Yin Liu
ClCf	GT-ClC**f-fwd**	KS-q2174	TCGATATCTATGAACAGGGAGCA GTTGG	59,9	Stefan Scholl
	GT-ClC**f-rev**	KS-q2175	TGCCCATTTGTACCAACCTCTTT GTCT	58,2	Stefan Scholl
	GT-ClC**f-rev2**	KS-q2221	ATCTAAGATTGTAGAGGCGTTAT TGGACAA	57,5	Stefan Scholl
SALK T-DNA	TL1-**LB**	KS-P015	GCGTGGACCGCTTGCTGCAACT	60,4	Dr. Melanie Krebs

5.16. Media and Buffers

Table 4: Murashige & Skroog medium used for plant growth

liquid MS-Medium, 500 ml	amount in [g]
MS basal salt mixture (Duchefa) (½)	1,0755
H_2O dd	up to 500 ml

→ adjust pH to 5,8 (KOH) and autoclave

solid MS-Medium, 500 ml	amount in [g]
MS basal salt mixture (Duchefa) (½)	1,0755
Phytoagar (0,4%)	2
H_2O dd	up to 500 ml

→ adjust pH to 5,8 (KOH) and autoclave

Table 5: Modified Johns` medium without Cl^- and NO_3^- for plant growth

Modified Johns` Medium, 500 ml	amount in [ml]
100 mM-Glutamine (1,5 mM)	7,5
100 mM KH_2PO_4 (1mM)	5
50 mM $MgSO_4$ x $7H_2O$ (0,5 mM)	5
$CaSO_4$ x 2 H_2O (1,25 mM)	0,1076 g
100 mM Na_2SiO_3x5 H_2O (100 µM)	0,5
50 mM Na-Fe-EDTA (50 µM)	0,5
Micronutrient Stock	0,5
50 mM H_3BO_3 (50 µM)	
3 mM $MnSO_4$ x H_2O (3 µM)	
1,3 mM $CuSO_4$ x $5H_2O$ (1,3 µM)	
1 mM $ZnSO_4$ x $7H_2O$ (1µM)	
0,03 mM $Mo_7O_{24}(NH_4)_6$ (0,03 µM)	
1 M MES (5 mM)	2,5

→ adjust pH to 5,8 (TRIS or KOH) and autoclave

Table 6: Luria-Both (LB) bacteria medium used for *Escherichia coli* and *Agrobacterium tumefaciens* cultivation

liquid LB-Medium, 1000 ml	amount in [g]
Bacto tryptone	10
Bacto yeast extract	5
NaCl	10
H_2O dd	up to 1000 ml

solid LB-Medium, 1000 ml	amount in [g]
Bacto tryptone	10
Bacto yeast extract	5
NaCl	10
Bacto agar	15
H_2O dd	up to 1000 ml

Table 7: pH calibration buffers for intracellular pH measurements

Buffer range pH 4,8; for 25 ml	amount in [ml]
1 M citric acid (50 mM)	1,25
1M trisodium citrate (50 mM)	1,25
1M Ammoniumacetate (50 mM)	1,25
HCl	adjust pH 4,8
H_2O dd	up to 25 ml

→ sterile filter and store at 4°C

Buffer range pH 5,2 to 6,4; for 25 ml	amount in [ml]
1 M MES (50 mM)	1,25
1M Ammoniumacetate (50 mM)	1,25
1M Bis-Tris-Propane	adjust desired pH
H_2O dd	up to 25 ml

→ sterile filter and store at 4°C

Buffer range pH 6,8 to 8,0; for 25 ml	amount in [ml]
1 M Hepes (50 mM)	1,25
1M Ammoniumacetate (50 mM)	1,25
1M Bis-Tris-Propane (50 mM)	adjust desired pH
H_2O dd	up to 25 ml

→ sterile filter and store at 4°C

Table 8: Solutions for mesophyll protoplast preparation

Enzyme Solution; for 10 ml	amount in [ml]
1 M MES-KOH pH 5,7 (20 mM)	0,22
Cellulase R10 (1,5%)	0,15 g
Mazerozyme R10 (0,4%)	0,04g
1 M Mannitol (400 mM)	4
1 M KCl (20 mM)	0,2
1 M $CaCl_2$ (10 mM)	0,1
BSA (0,1%)	0,01 g
ddH_2O	up to 10 ml

→ mix enzymes with Mannitol and MES, incubate at 55°C for 10 min; cool down to RT

→ add other components, sterile filter and store at 4°C

W5 Solution; for 250 ml	amount in [ml]
1 M MES-KOH pH 5,7 (2 mM)	0,5
1M NaCl (154 mM)	38,5
1M $CaCl_2$ $2H_2O$ (125 mM)	31,25
1M KCl (5 mM)	1,25
H_2O dd	up to 250 ml

→ autoclave

MMG-Solution; for 250 ml	amount in [ml]
1 M MES-KOH pH 5,7 (4 mM)	1
1M $MgCl_2$ $2H_2O$ (15 mM)	3,75
1M Mannitol 400 mM)	100
H_2O dd	up to 250 ml

→ autoclave

PEG-Solution; for 2 ml	amount in [ml]
Polyethylenglycol, PEG 4000 (40%)	0,8 g
1M Mannitol (200 mM)	0,4
1M $Ca(NO_3)_2$ $4H_2O$ (100 mM)	0,2
H_2O dd	up to 2 ml

→ prepare freshly at day of transfection

WI Solution; for 250 ml	amount in [ml]
1 M MES-KOH pH 5,7 (4 mM)	1
1M Mannitol (500 mM)	125
1 M KCl (20 mM)	5
H_2O dd	up to 250 ml

→ autoclave

Table 9: Edwards` Buffer for genomic DNA extraction

Edwards` Buffer ; for 100 ml	amount in [ml]
1 M TRIS-HCl pH 7,5 (200 mM)	20
0,5 M EDTA (25 mM)	5
1 M NaCl (250 mM)	25
10% SDS (w/v) (0,5%)	5
H_2O dd	up to 100 ml

5.17. Macros for Image J

5.17.1. Quantification of average fluorescence intensities

```
1 for (i=1; i<=nSlices; i++)
2 {selectWindow("561");
3 setThreshold(20,254);
4 run("Measure");
5 run("Next Slice [>]");}
6 run("Close All")
```

5.17.2. Intracellular pH measurements using pHusion or BCECF

```
1 for (i=1; i<=nSlices; i++)
2 {selectWindow("561"); → Channel of pH independent wavelength
3 setThreshold(40, 254); → depends on signal strength
4 run("Create Selection");
5 resetThreshold();
6 run("Measure");
7 roiManager("Add");
8 selectWindow("488");→ Channel of pH dependent wavelength
9 roiManager("Select", 0);
10 run("Measure");
11 roiManager("Delete");
12 run("Select None");
13 selectWindow("561");
14 run("Select None");
15 run("Next Slice [>]");
16 selectWindow("488");
17 run("Next Slice [>]");}
18 run("Close All");
```

5.17.3. pH measurement of individual SYP61-pHusion positive particles

```
1 selectWindow("RFP");
2 run("Duplicate...", "title=RFP-1");
3 run("Mean...", "radius=2");
4 setAutoThreshold("Default dark");
5 //run("Threshold...");
6 setThreshold(30, 254); → depends on signal strength
7 run("Analyze Particles...", "size=0.05-3.00 circularity=0.30-1.00 show=Nothing add");
8 selectWindow("RFP");
9 roiManager("Show All");
10 roiManager("Measure");
11 IJ.renameResults("rfp");
12 saveAs("Results", "Insert path where data should be saved ");
13 selectWindow("GFP");
14 roiManager("Show None");
15 roiManager("Show All");
16 roiManager("Measure");
17 IJ.renameResults("gfp");
18 saveAs("Results", "Insert path where data should be saved")
19 selectWindow("RFP-1");
20 close();
```

6. Supplementary Information

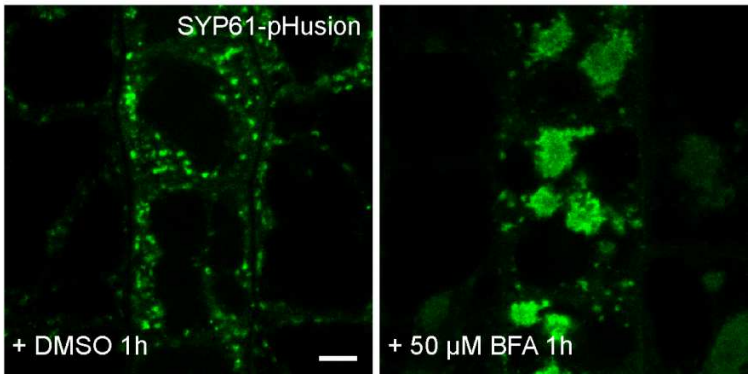

Supplementary Figure S1: SYP61-pHusion accumulates in core BFA compartments. Confocal laser scanning microscopy images of root epidermal cells of 6 days old Arabidopsis seedlings expressing $P16_{Pro}$:SYP61-pHusion. Whole seedlings were treated with 50 µM Brefeldin A (BFA) or equal amount of DMSO 1h prior to imaging. After treatment with DMSO signals appeared as in WT whereas after 50 µM BFA SYP61-pHusion signals concentrated in the core of BFA compartments. Bar = 5 µm.

Results are published in Luo et al., 2015.

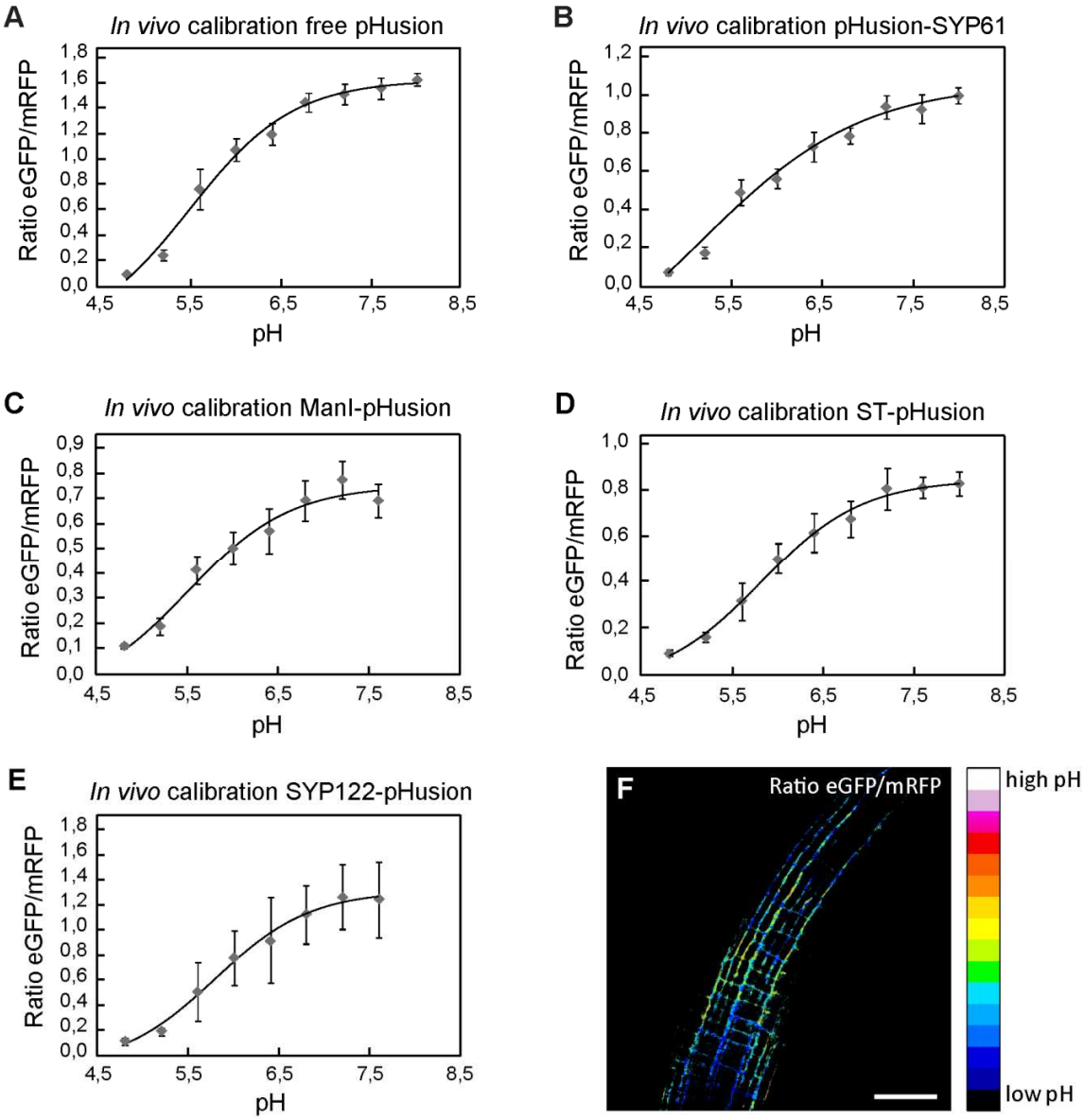

Supplementary Figure S2: pH sensors for Golgi apparatus and apoplast and *in vivo* calibration curves of pHusion-based intracellular pH sensors. (A) *In vivo* calibration curve of $35S_{Pro}$:pHusion. (**B)** *In vivo* calibration curve of $P16_{Pro}$:pHusion-SYP61. **(C)** CLSM images of *cis*-Golgi pH sensor $P16_{Pro}$:ManI-pHusion and **(D)** *In vivo* calibration of $P16_{Pro}$:ManI-pHusion. **(E)** CLSM micrograph of $P16_{Pro}$:ST-pHusion *trans*-Golgi pH sensor lines. **(F)** *In vivo* calibration curve of $P16_{Pro}$:ST-pHusion. **(G)** Root elongation zone cells of $UBQ10_{Pro}$:SYP122-pHusion expressing plants. and **(H)** *In vivo* calibration curve of the apoplastic pH sensor in the root elongation zone. All images and data for *in vivo* calibrations were acquired in root elongation zone cells of stably expressing Arabidopsis lines. Error bars = SD of n=15 seedlings per pH value. Bars= 5µm.

Results in **(A, B, D)** are published in Luo et al. 2015.

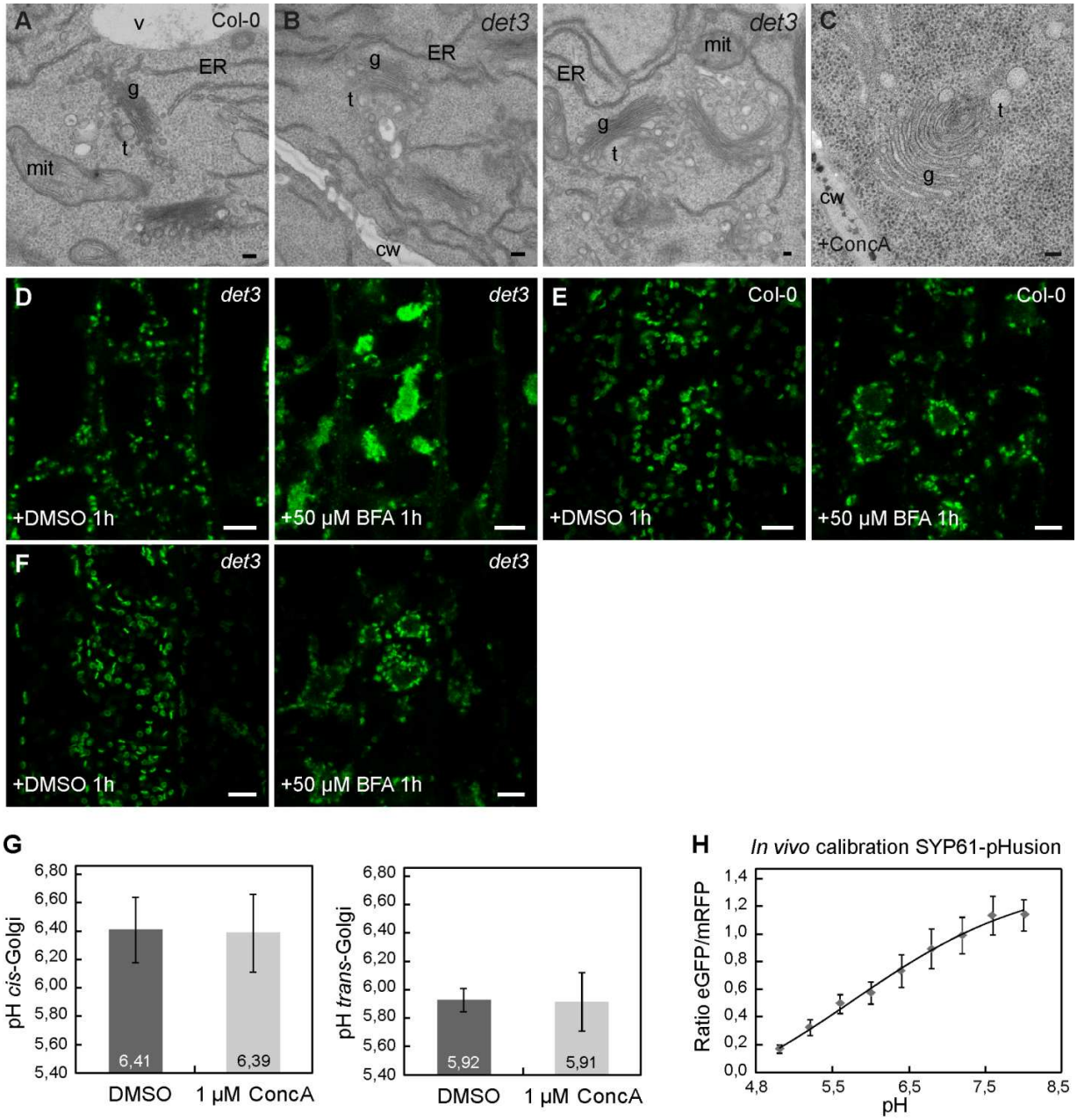

Supplementary Figure S3: Golgi stack morphology in *det3*, pH sensor signals in *det3,* and Golgi pH measurements. All images were taken in root cells of 6 days old Arabidopsis seedlings. **(A)** TEM micrograph of Golgi stacks and TGN/EE in high pressure frozen, freeze-substituted root cell of Col-0 and **(B)** *det 3*. **(C)** Detail of TGN-Golgi hybrid compartment with a cup-shaped Golgi stack in 1 µM ConcA treated roots for 24h. **(D)** CLSM images of $P16_{Pro}$:SYP61-pHusion expressing plants 1h with DMSO or 50 µM BFA. **(E)** Signals of $P16_{Pro}$:ST-pHusion in Col-0 plants after 1h treatment with 50 µM BFA or DMSO. **(F)** $P16_{Pro}$:ST-pHusion in *det3* shows identical localisation in DMSO or 50 µM BFA treated cells as WT Col-0. **(G)** pH measurement of *cis*-Golgi with $P16_{Pro}$:ManI-pHusion and *trans*-Golgi using $P16_{Pro}$:ST-pHusion after 3h treatment with ConcA. Error bars = SD of n=15 seedlings.

Supplementary Figure S3 (continued)

(H) *In vivo* calibration curve of $P16_{Pro}$:SYP61-pHusion. All values were acquired in root elongation zone cells of $P16_{Pro}$:SYP61-pHusion expressing *Arabidopsis thaliana* seedlings 6 days after germination. Calibration was done for 15 min per buffer in presence of 1µM ConcA. Error bars = SD of n=15. Abbrevations: cw = cell wall, ER = Endoplasmic Reticulum, g = Golgi apparatus, mit = mitochodrium, t = TGN/EE, v = vacuole. Bars = 200 nm **(A-D)** or 5 µM **(E-G)**.

Results **(A-F)** are published in Luo et al., 2015.

Images **(A, B)**: Courtesy of Dr. York-Dieter Stierhoff.

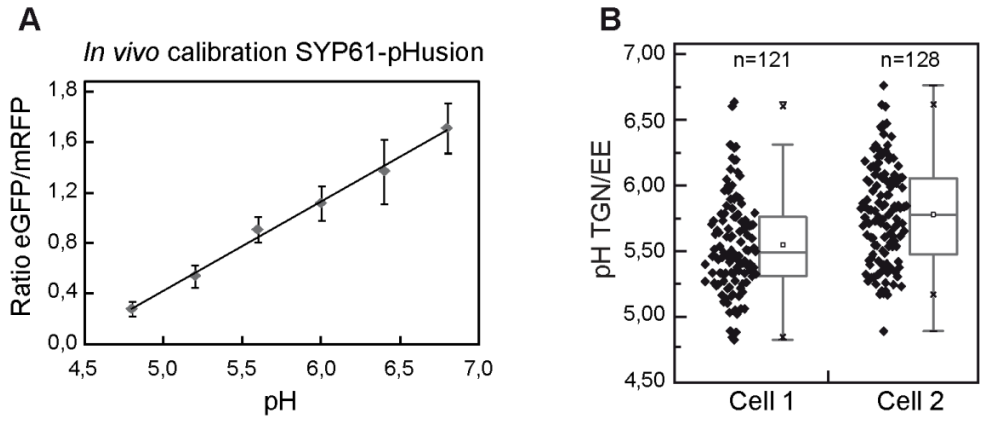

Supplementary Figure S4: pH measurements in SYP61-pHusion positive particles. (A) *In vivo* calibration of $P16_{Pro}$:SYP61-pHusion. All values were taken in single root epidermal cells of 6 days old Arabidopsis seedlings after 15 min incubation with respective calibration buffers. Error bars = SD of n=15 cells for every pH value. **(B)** pH values of SYP61-pHusion positive particles. Data was extracted using "particle analyzer" function of Image J and ratios for each particle were calculated. Note that a particle represents either a single TGN/EE, a cluster of two or three TGN/EE or a TGN/EE subdomain. Data in brackets represent number of analysed particles.

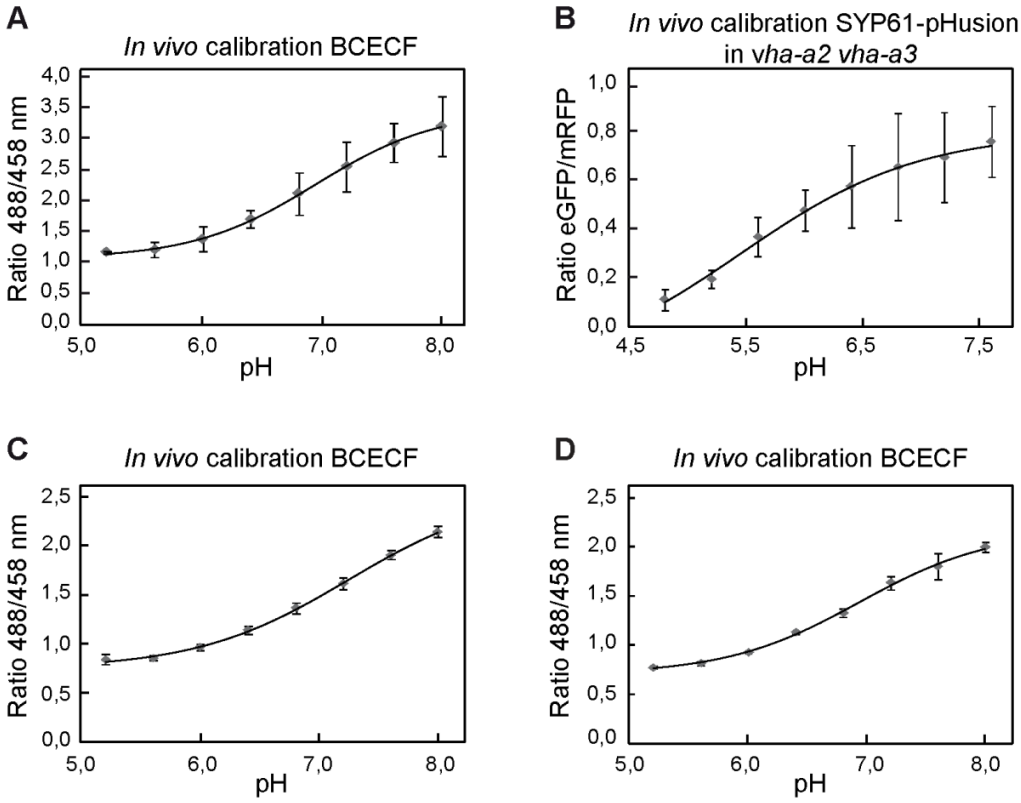

Supplementary Figure S5: *In vivo* calibration curves of P16$_{Pro}$:SYP61-pHusion in *vha-a2 vha-a3* background and of BCECF. (A) *In vivo* calibration curve of BCECF loaded vacuoles of WT Col-0, Error bars = SD of n=15 seedlings per pH value. **(B)** *In vivo* calibration of P16$_{Pro}$:SYP61-pHusion 2 in *vha-a2 vha-a3* background. **(C)**, **(D)** *In vivo* calibration curves of BCECF loaded vacuoles of WT Col-0. All error bars = SD of n=15 seedlings per pH value.

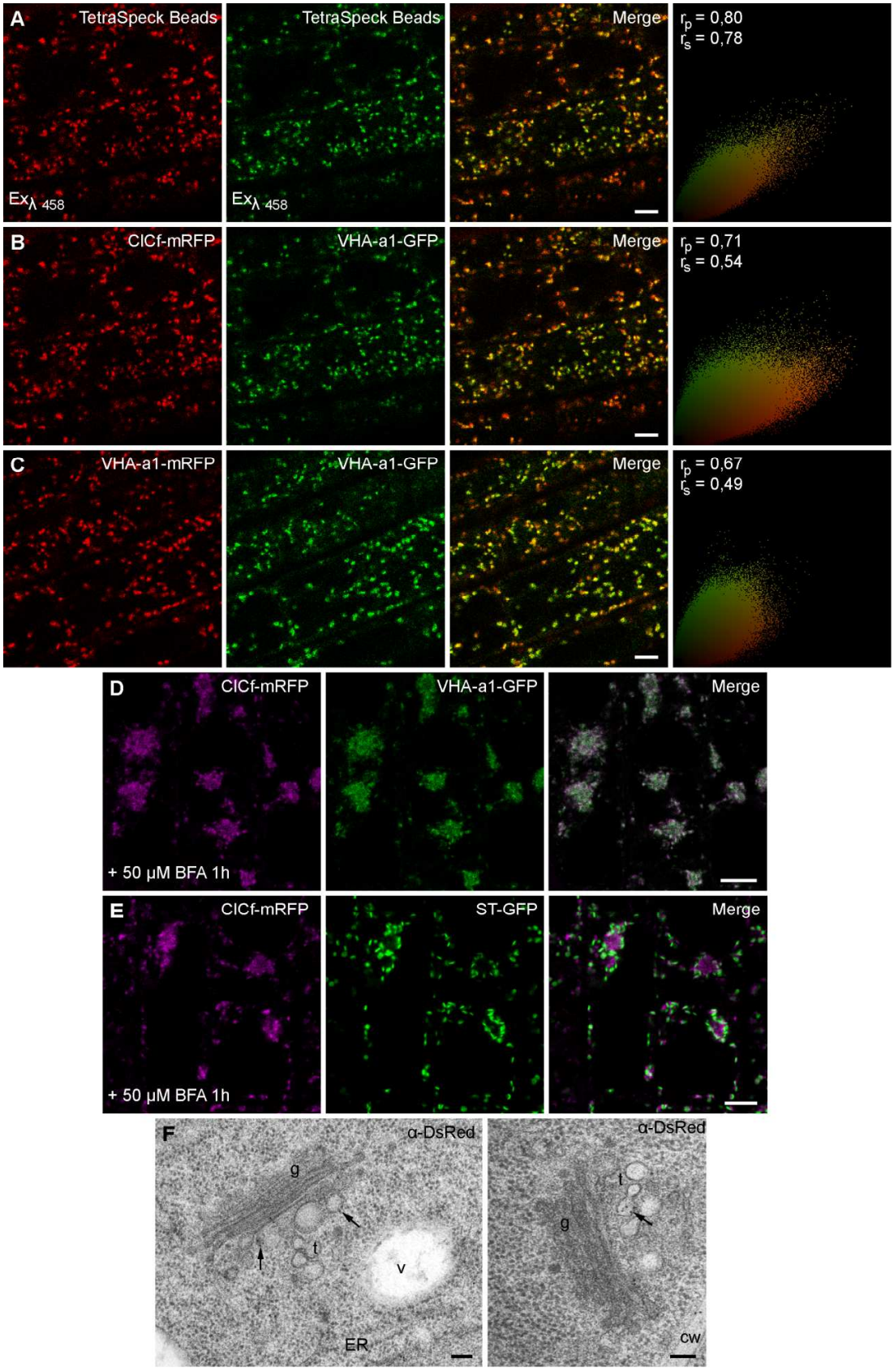
A
TetraSpeck Beads
Ex λ 458
TetraSpeck Beads
Ex λ 458
Merge
r_p = 0,80
r_s = 0,78
B
ClCf-mRFP
VHA-a1-GFP
Merge
r_p = 0,71
r_s = 0,54
C
VHA-a1-mRFP
VHA-a1-GFP
Merge
r_p = 0,67
r_s = 0,49
D
ClCf-mRFP
VHA-a1-GFP
Merge
+ 50 µM BFA 1h
E
ClCf-mRFP
ST-GFP
Merge
+ 50 µM BFA 1h
F
α-DsRed
g
t
f
v
ER
α-DsRed
t
g
cw

Supplementary Figure S6: ClCf-mRFP is mainly located at the TGN/EE. CLSM images of 6 days old Arabidopsis root cells and quantification of co-localisation using Pearson (r_p) and Spearman (r_s) correlation coefficient. Correlations range from +1 for positive, and -1 for negative correlation. r_p and r_s with respective scatterplots are shown on the right of series **(A-C)**. **(A)** TetraSpeck^{TM} fluorescent microspheres of 500 nm in diameter. **(B)** ClCf-mRFP and VHA-a1-GFP localise in overlapping dot-like patterns. **(C)** Arabidopsis lines stably co-expressing VHA-a1GFP and VHA-a1-mRFP. **(D)** CLSM image of ClCf-mRFP and VHA-a1-GFP co-expressing plants treated with 50 µM BFA for 1h. Both markers localise at BFA compartment core. **(E)** ST-GFP does not co-localise with ClCf-mRFP after 50 µM BFA treatment for 1h. **(F)** Immunogold labelling of high-pressure frozen, freeze substituted root cells expressing ClCf-mRFP. Sections were labelled with α-DsRed detection primary antibody and secondary antibody linked to 10 nm colloidal gold. Arrows depict colloidal gold particles. Abbreviations: cw = cell wall, ER = Endoplasmic Reticulum, g = Golgi apparatus, t = TGN/EE, v = vacuole. Bars = 5 µm **(A)**; 10 µM **(B, C, D)**. Scatterplots and correlations were generated from n=5 images of 10 roots for **(B,D)** or 30 images for **(C)**.

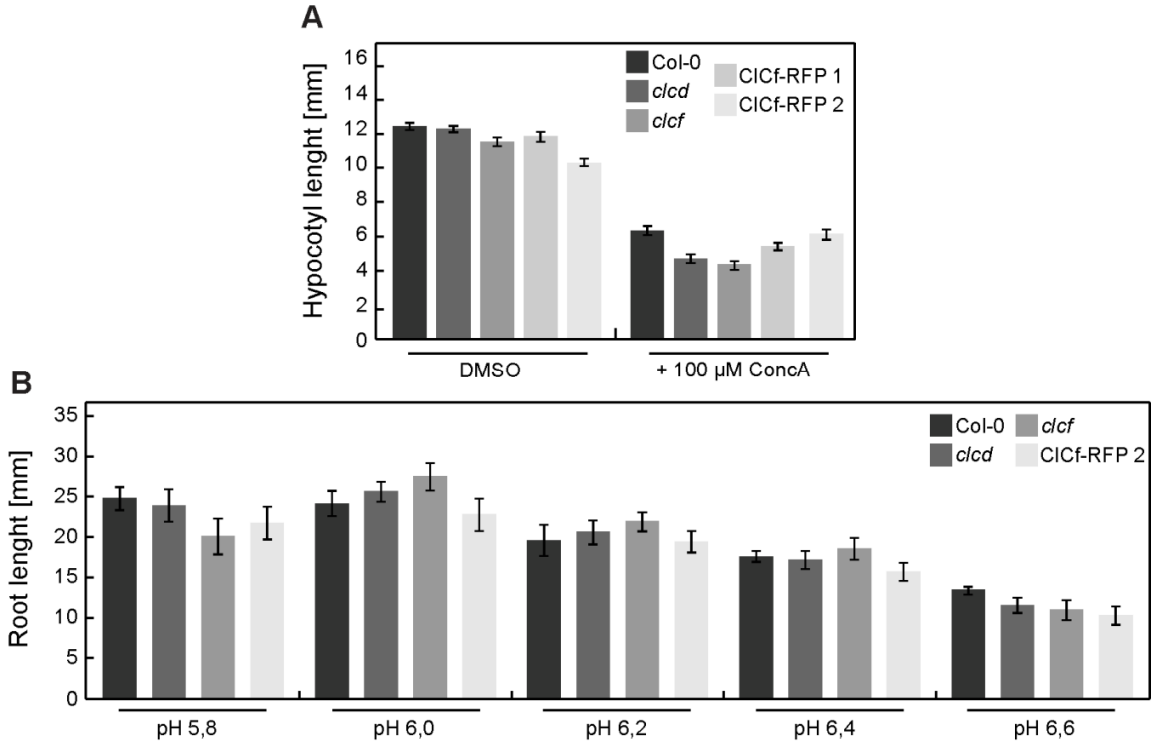

Supplementary Figure S7: Hypocotyl and root length measurements of *clcd* and *clcf*. **(A)** Absolute values of hypocotyl length measurements in Figure 13 D. Error bars = SE of n=30 hypocotyls for each. **(B)** Root length measurements of 7 days old Arabidopsis seedlings grown on chloride- and nitrate-free Johns` Medium, 5 mM MES-TRIS with different pH values (indicated on X-axis). Error bars = SE of n=16 roots, each.

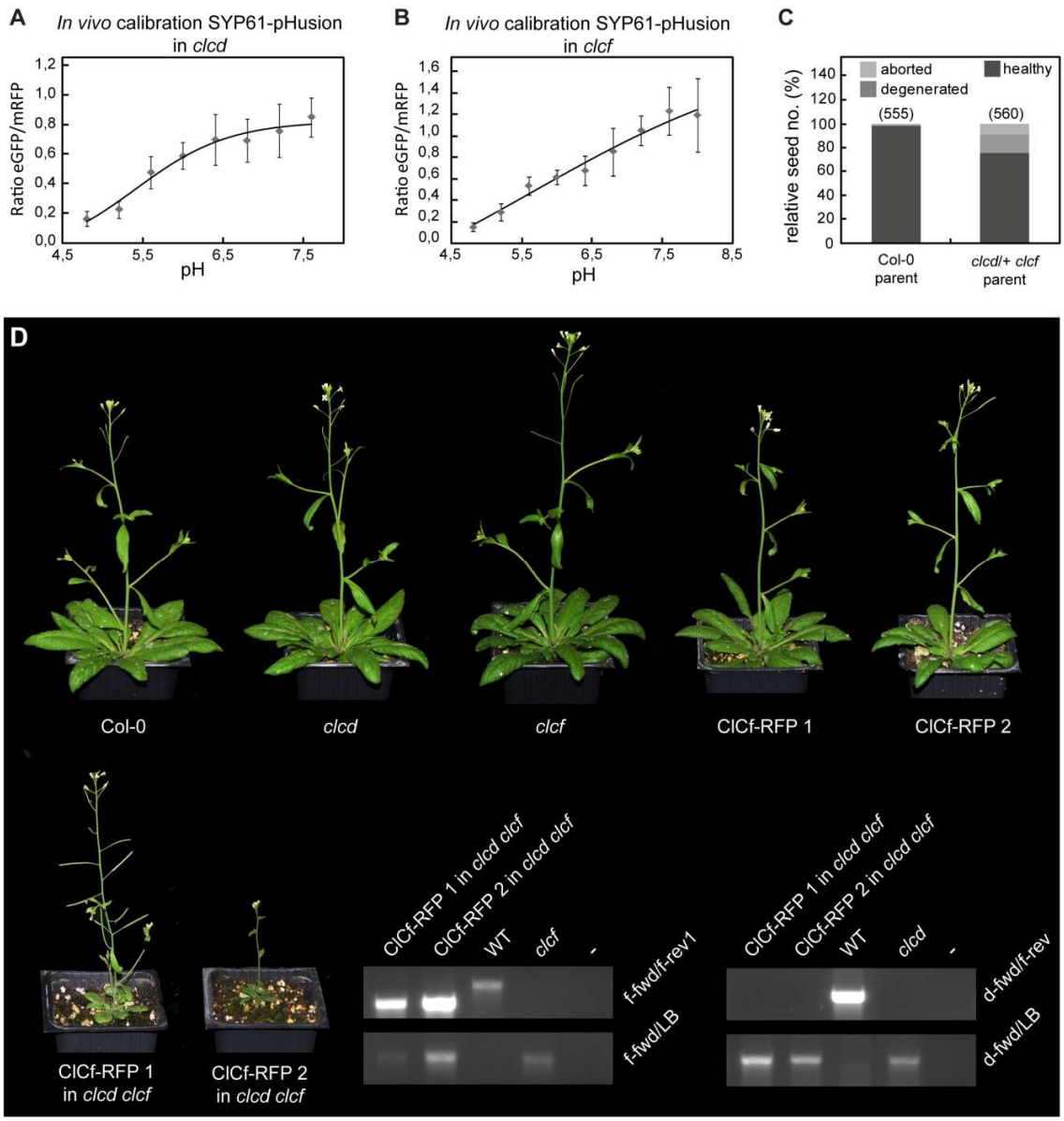

Supplementary Figure S8:.**Calibration of TGN/EE pH sensor and complementation of a *clcd clcf* mutant. (A)** *In vivo* calibration of $P16_{Pro}$:SYP61-pHusion in *clcd* background. Error bars = SD of n=15 seedlings per pH value. **(B)** *In vivo* calibration of $P16_{Pro}$:SYP61-pHusion in *clcf* background. Error bars = SD of n=15 seedlings per pH value. **(C)** Seed count of mature siliques of WT Col-0 and *clcd*/+ *clcf* parent plants. Seeds of 10 siliques were counted and percentage was calculated by dividing observed seed phenotypes with total seed number (in brackets above bars). **(D)** Arabidopsis plants grown at long day conditions, 31 days after stratification and respective PCR reactions for genotyping of both *clcd clcf* complementation lines ClCf-mRFP1 in *clcd clcf* and ClCf-mRFP2 in *clca clcf.*

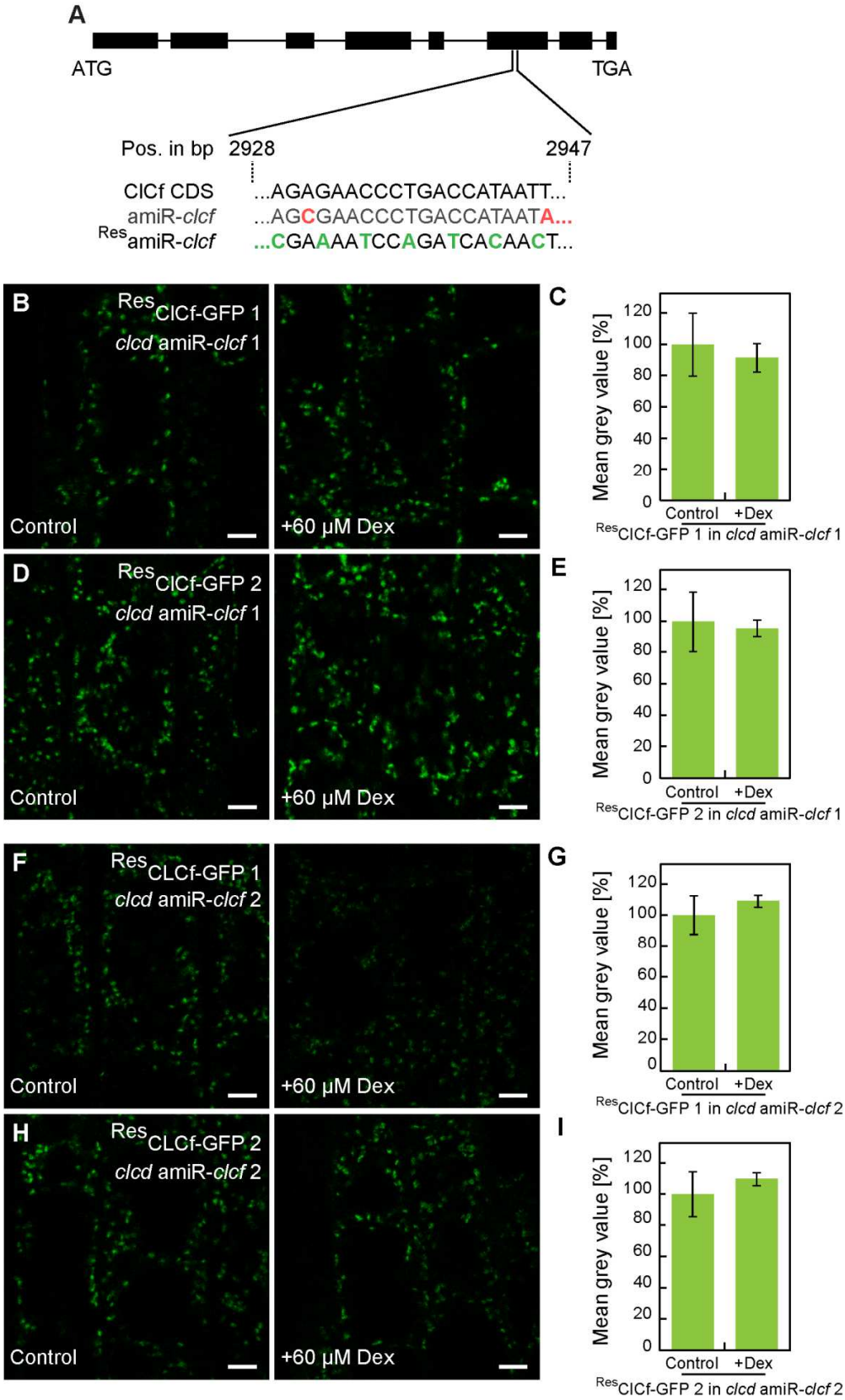
A
ATG
TGA
Pos. in bp 2928 2947
ClCf CDS ...AGAGAACCCTGACCATAATT...
amiR-clcf ...AGCGAACCCTGACCATAATA...
Res amiR-clcf ...CGAAAATCCAGATCACAACT...
B
Res ClCf-GFP 1
clcd amiR-clcf 1
Control
+60 µM Dex
C
Mean grey value [%]
Control +Dex
Res ClCf-GFP 1 in clcd amiR-clcf 1
D
Res ClCf-GFP 2
clcd amiR-clcf 1
Control
+60 µM Dex
E
Mean grey value [%]
Control +Dex
Res ClCf-GFP 2 in clcd amiR-clcf 1
F
Res CLCf-GFP 1
clcd amiR-clcf 2
Control
+60 µM Dex
G
Mean grey value [%]
Control +Dex
Res ClCf-GFP 1 in clcd amiR-clcf 2
H
Res CLCf-GFP 2
clcd amiR-clcf 2
Control
+60 µM Dex
I
Mean grey value [%]
Control +Dex
Res ClCf-GFP 2 in clcd amiR-clcf 2

Supplementary Figure S9: Mutation of the amiR-*clcf* binding site is sufficient to render ClCf amiR resistant. **(A)** Schematic overview over *ClCf* ORF. Exchange of bp in the amiR binding site in green. **(B-E)** GFP fluorescence was not altered after Dex treatment when ^{Res}ClCf-GFP constructs were introduced in *clcd* amiR-*clcf* 1 background. **(F-I)** Reduction of ClCf-RFP in *clcd* amiR-*clcf* 2 after Dex could be restored by introduction of ^{Res}ClCf-GFP constructs. **(C)**, **(E)**, **(G)**, **(I)** average of 3 ind. measurements with n=15 seedlings, each. Error bars=SD. Bars=5µm.

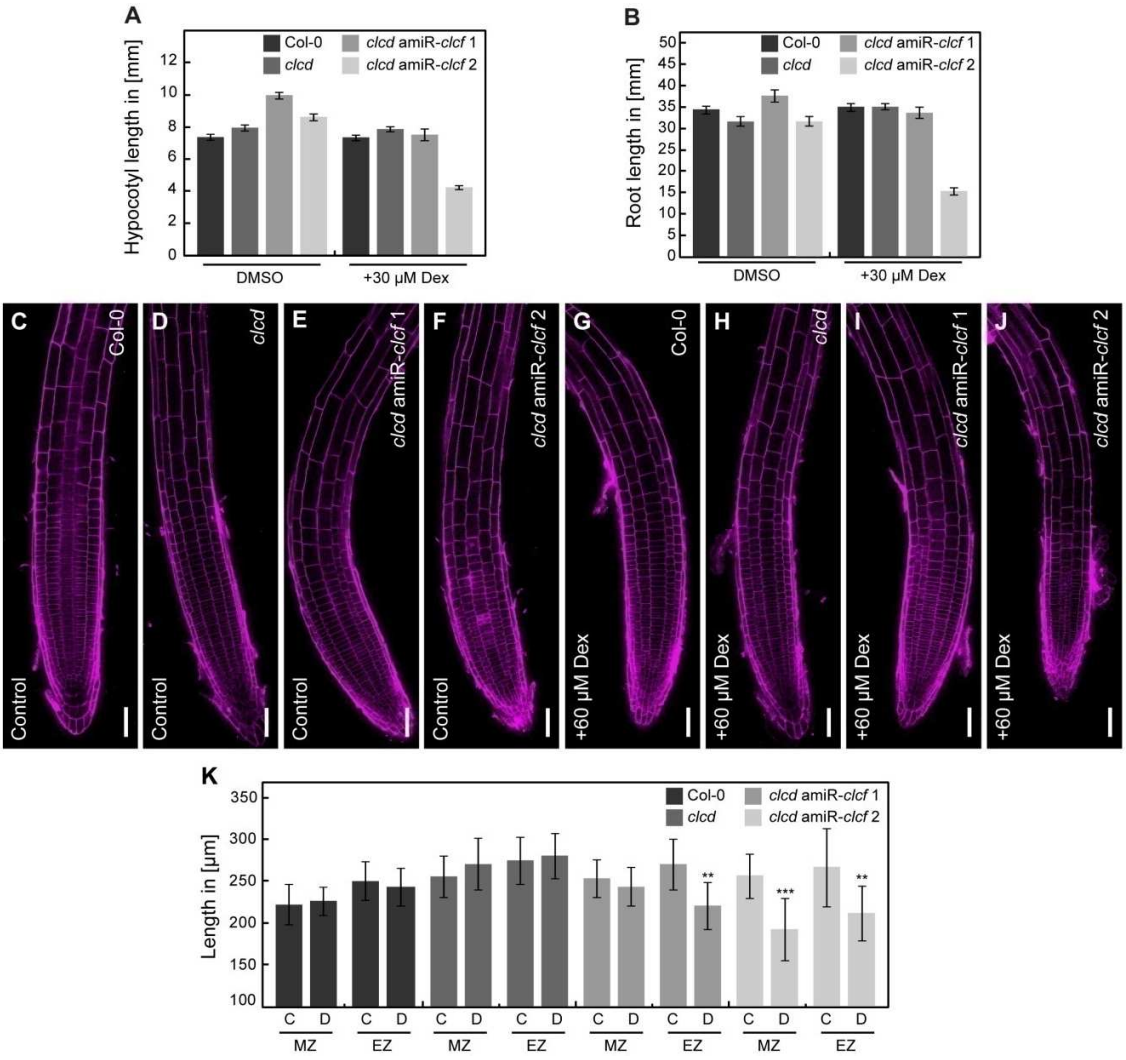

Supplementary Figure S10: Measurement of hypocotyl, root and root zone length in *clcd* amiR-*clcf* (A) Absolute values of hypocotyl length measurements in Figure 16 A. Error bars = SE of n=30 hypocotyls for each genotype and condition. **(B)** Absolute values of root length measurements in Figure 16 B. Error bars = SE of n=30 roots for each genotype and condition. **(C)** Root of WT, **(D)** *clcd*, **(E)** *clcd* amiR-*clcf* 1 or **(F)** *clcd* amiR-*clcf* 2, 7days after stratification, 3 days control conditions, stained with 3 µg/ml propidium iodide. **(G-J)** Roots of respective genotypes 72h after growth on 60 µM Dex-containing medium and propidium iodide staining (3 µg/ml). **(K)** Measurement of root meristematic zone (MZ) or elongation zone (EZ) at 72h control (C) or 60 µM Dex treatment (D). Error bars = SD of n=10 roots. Bars = 50 µm. Asterisks indicate P-values with *=P<0,05; **=P<0,01; ***=P<0,001 or n.s. = P≥ 0,05, P Student´s t-test.

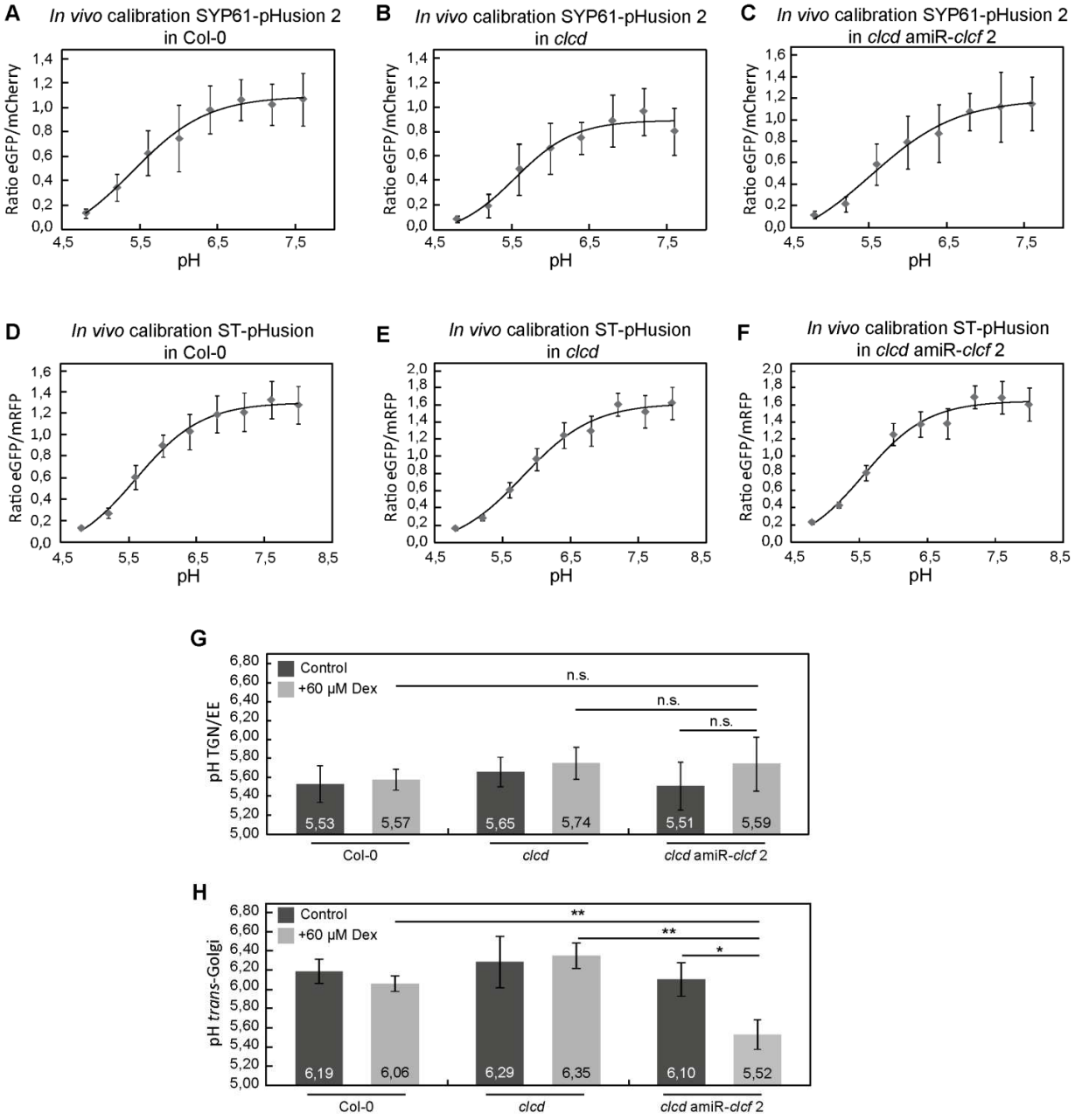

Supplementary Figure S11: TGN/EE and *trans*-Golgi stack pH measurements in *clcd* amiR-*clcf*. *In vivo* calibration of $UBQ10_{Pro}$:SYP61-pHusion 2 in **(A)** Col-0, **(B)**, *clcd* or **(C)** *clcd* amiR-*clcf* 2 background. Error bars=SD of n=15 seedlings per pH value. *In vivo* calibration of $UBQ10_{Pro}$:ST-pHusion in **(E)** Col-0, **(E)**, *clcd* or **(F)** *clcd* amiR-*clcf* 2 background. Error bars = SD of n=15 seedlings per pH value. **(G)** *In vivo* pH measurements after 72h of Dex treatment using $UBQ10_{Pro}$:SYP61-pHusion 2. Average pH of 3 independent measurements with n=15 seedlings, each. Error bars = SD. **(H)** *In vivo* pH measurements after 72h of Dex treatment using $UBQ10_{Pro}$:ST-pHusion. Average of 3 independent measurements with n=15 seedlings. Error bars = SD. Asterisks indicate P-values with *=P<0,05; **=P<0,01; ***=P<0,001 or n.s. = P≥ 0,05, P Student´s t-test.

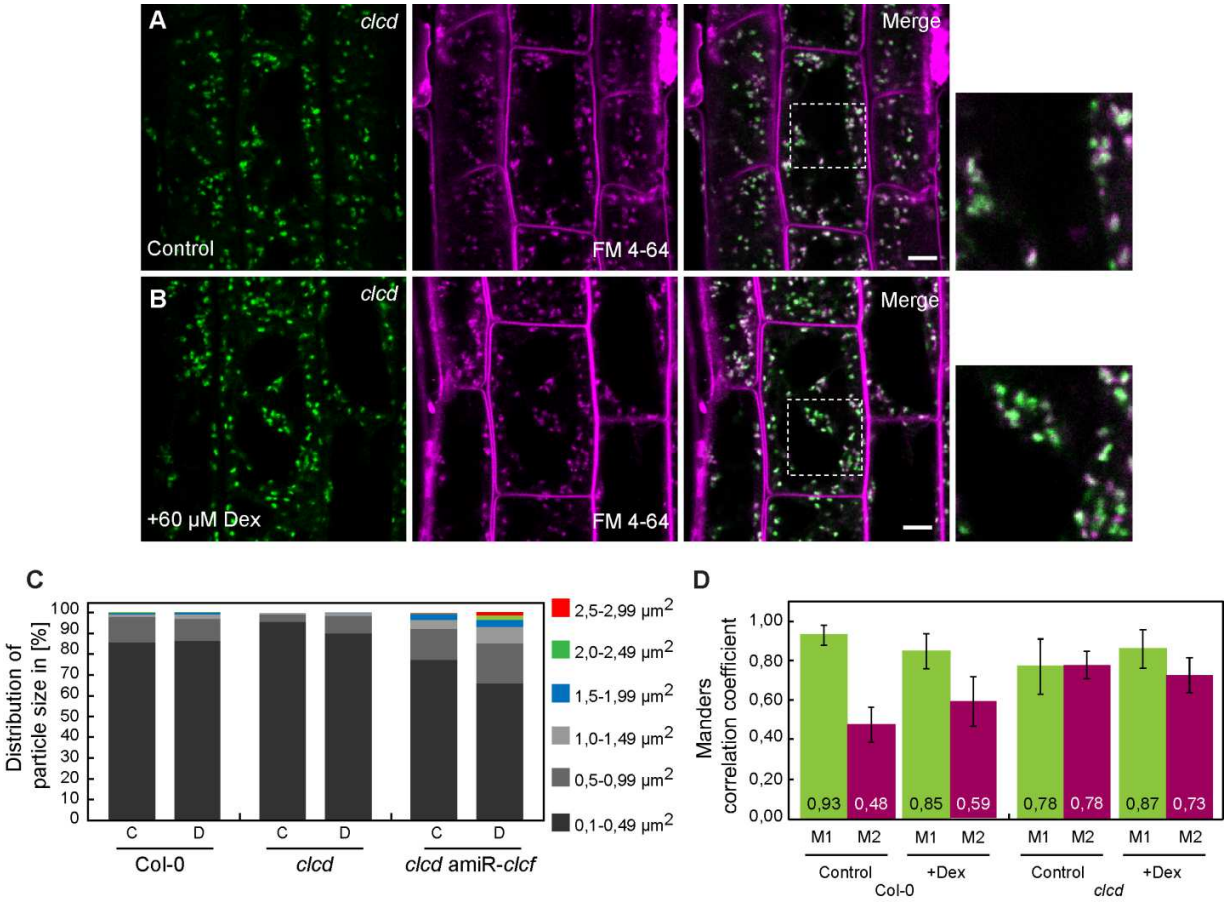

Supplementary Figure S12: VHA-a1 co-localisation with FM 4-64 in *clcd* and TGN/EE particle size. (A) CLSM images elongation zone cells of 6 days old Arabidopsis roots, expressing VHA-a1 (green), co-stained with FM 4-64 for 15 min (magenta) in *clcd* control or **(B)** 60 µM Dex treated *clcd* roots. **(C)** Distribution of particle size in Col-0, *clcd* or in *clcd* amiR-*clcf* in mock or Dex treatments after 72h. Data were collected in $UBQ10_{Pro}$:SYP61-pHusion 2 expressing lines from n=15 seedlings for each genotype and treatment and analysed via particle analyzer in ImageJ. **(D)** Manders correlation coefficient of M1 VHA-a1 to FM 4-64 and M2 FM 4-64 to VHA-a1. Data was taken from 10 cells of 10 different roots Error bars = SD. Bars = 5 µm.

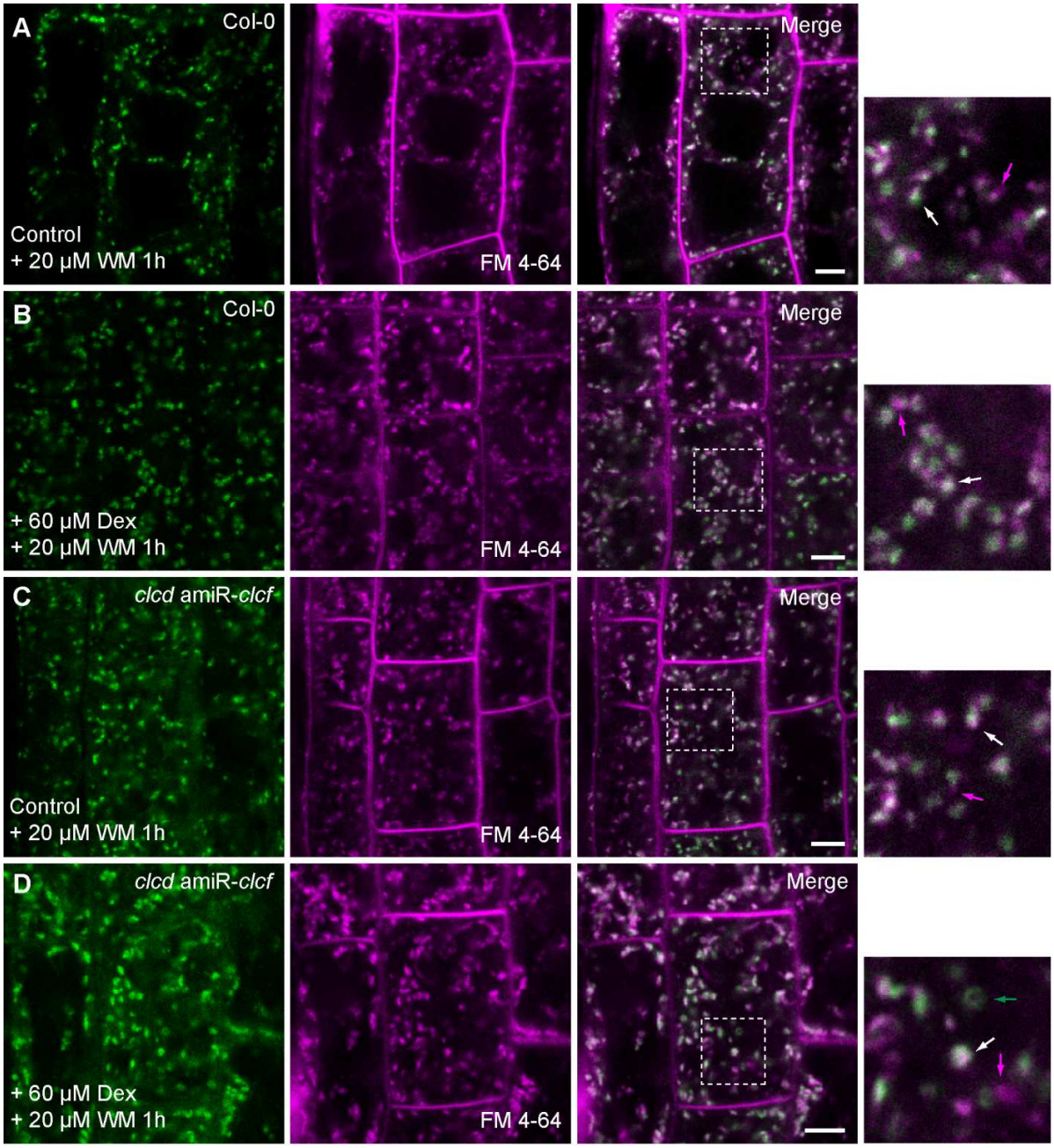
A
Col-0
Control
+ 20 µM WM 1h
FM 4-64
Merge
B
Col-0
+ 60 µM Dex
+ 20 µM WM 1h
FM 4-64
Merge
C
clcd amiR-clcf
Control
+ 20 µM WM 1h
FM 4-64
Merge
D
clcd amiR-clcf
+ 60 µM Dex
+ 20 µM WM 1h
FM 4-64
Merge

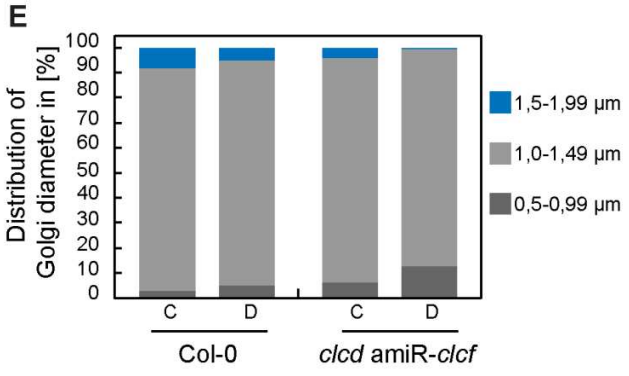
E
Distribution of Golgi diameter in [%]
100
90
80
70
60
50
40
30
20
10
0
C
D
C
D
Col-0
clcd amiR-clcf
1,5-1,99 µm
1,0-1,49 µm
0,5-0,99 µm

Supplementary Figure S13: ***trans*-Golgi like structures in induced *clcd* amiR-*clcf* are not stained with FM 4-64.** **(A)** CLSM images of elongation zone cells of 6 days old Arabidopsis Col-0 roots, expressing VHA-a1-GFP (green), co-stained with FM 4-64 for 60 min (magenta) and treated with 20 µM Wortmannin (WM) for 1h, and **(B)** 60 µM Dex treated Col-0 roots of identical conditions. **(C)** CLSM micrographs of *clcd* amiR-*clcf* controls, expressing VHA-a1-GFP (green) and stained with FM 4-64 for 60 min (magenta). Seedlings were treated 1h with 20 µM WM prior to imaging, **(D)** *clcd* amiR-*clcf* induced with 60 µM Dex. **(E)** Distribution of Golgi diameter in Col-0, or *clcd* amiR-*clcf* in mock or Dex treatments after 72h. Data were collected in $UBQ10_{Pro}$:ST-pHusion expressing lines from n=15 seedlings for each genotype and treatment. Bars = 5 µm.

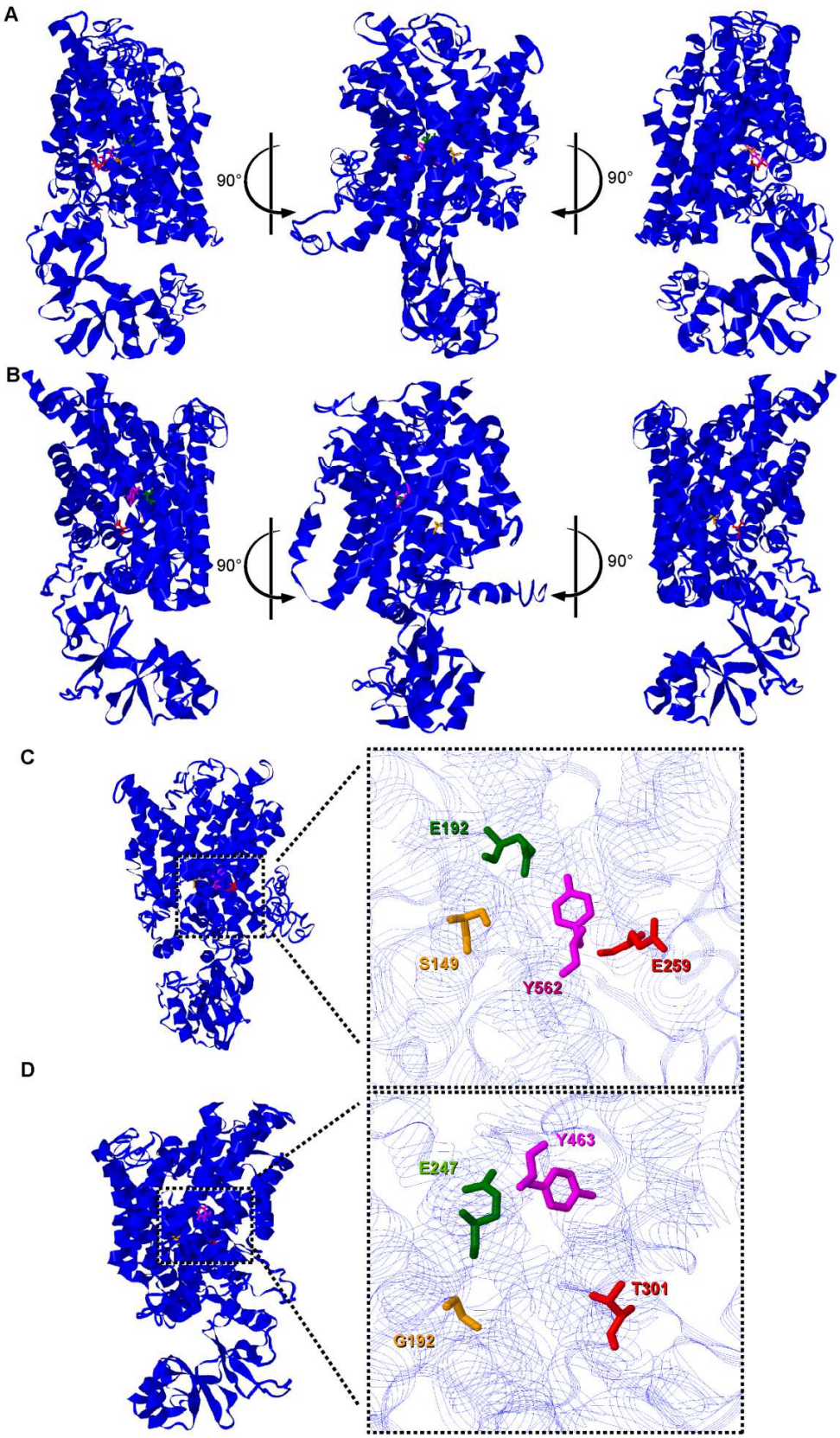
A
90°
90°
B
90°
90°
C
E192
S149
Y562
E259
D
Y463
E247
T301
G192

Supplementary Figure S14: Structural model of and critical amino acids of ClCd and ClCf. All structures were generated using the online tool I Tasser based on the crystal structure of the eukaryotic CmClC from the red algae *Cyanidioschyzon merolae*. All models were rotated 90° to left and 90° to the right from centered view. **(A)** Ribbon fold of ClCd model with highest confidence score. **(B)** Ribbon fold of ClCf model with highest confidence score. **(C)** Overview of ClCd structure in ribbon model and detail of critical amino acids depicted as stick models. **(D)** Overview of ClCf structure in ribbon model and detail of critical amino acids depicted as stick models. Critical amino acids are highlighted as follows: "gating glutamate" (green), "proton residue" (red) and "selectivity filter" residues (orange and magenta).

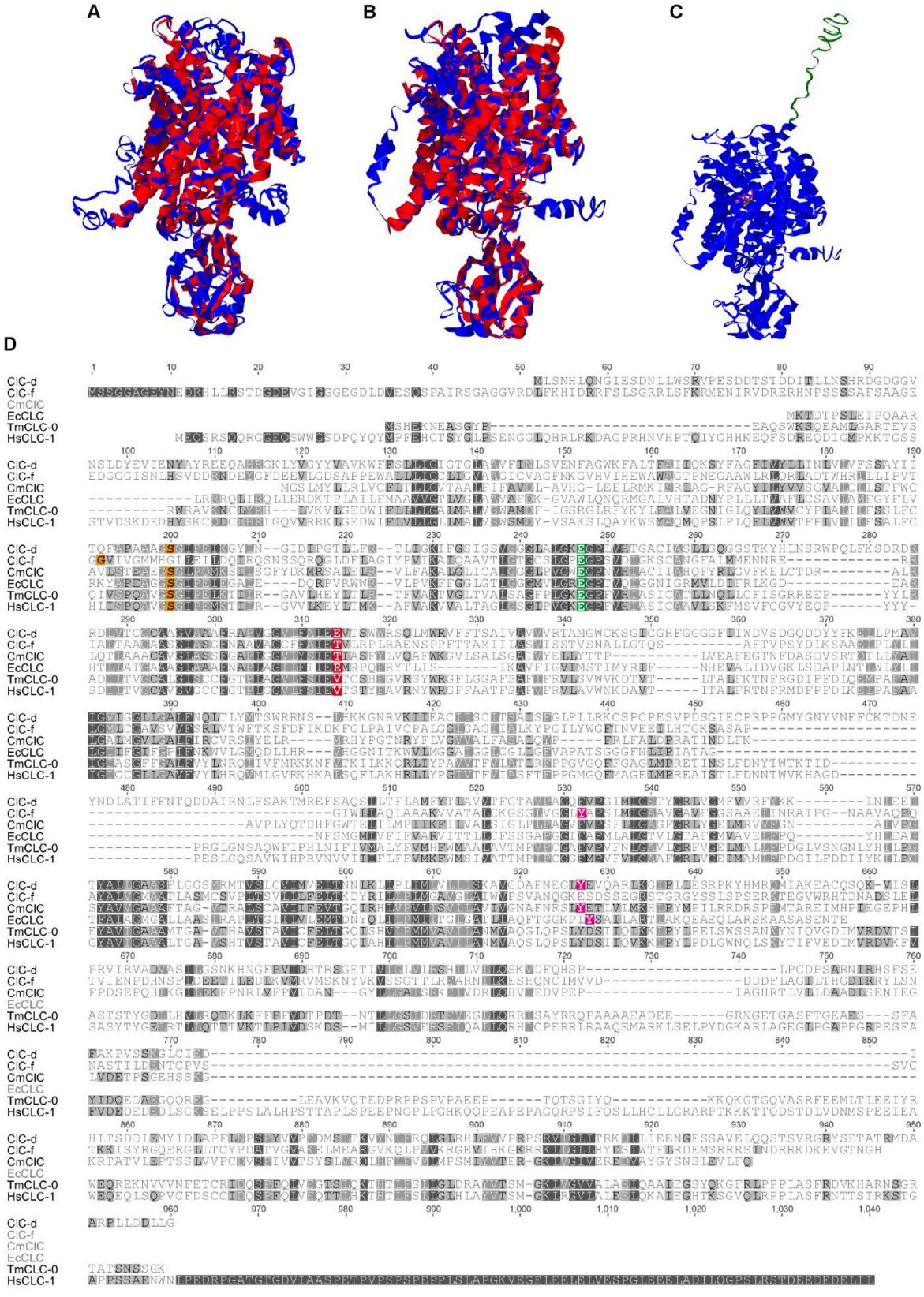
A
B
C
D
ClC-d
ClC-f
CmClC
EcCLC
TmCLC-0
HsCLC-1

Supplementary Figure S15: Structure and sequence alignment of ClCd and ClCf. (A) Structure alignment of ClCd (blue) with CmClC (red). **(B)** Structure alignment of ClCf (blue) with CmClC (red). **(C)** Full ribbon model of ClCf (blue) including the 35 amino acid N-terminus (green) which was excluded in all models and alignments. **(D)** Clustal W alignment of ClCd, ClCf, CmClC ClC-ec1, TmClC-0 and HsClC-1 protein sequences using a BLOSUM matrix with gap open cost 14, gap extend const 0,1. Critical amino acids are highlighted as follows: "gating glutamate" (green), "proton residue" (red) and "selectivity filter" residues (orange and magenta).

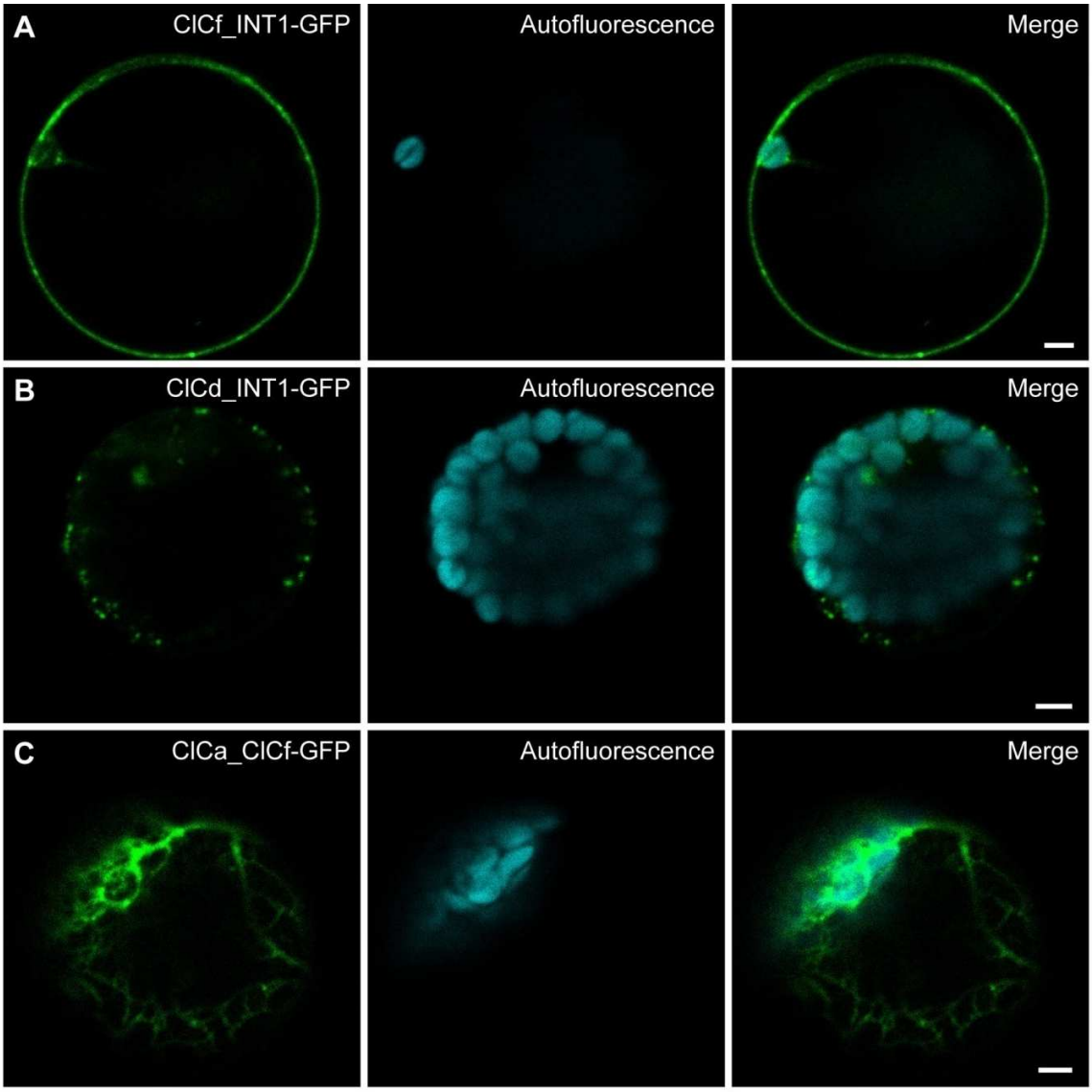

Supplementary Figure S16: Redirection of ClCd and ClCf to the tonoplast. CLSM images of Arabidopsis mesophyll protoplasts 3 days after transfection. **(A)** $UBQ10_{Pro}$:ClCf_INT1-GFP localises to cytosol or plasma membrane. **(B)** Dot-like, motile signals were observed at transfection of $UBQ10_{Pro}$:ClCd_INT1-GFP. **(C)** $UBQ10_{Pro}$:ClCa_ClCf-GFP signal was present in reticulate structures typical of the endoplasmic reticulum. Bars=5µm.

Experiments were done jointly with Franziska Lesche.

7. References

Accardi, A. (2015). Structure and gating of CLC channels and exchangers. J. Physiol. **593**: 4129–4138.

Anderson, C.T. (2016). We be jammin': An update on pectin biosynthesis, trafficking and dynamics. J. Exp. Bot. **67**: 495–502.

Arosio, D., and Ratto, G.M. (2014). Twenty years of fluorescence imaging of intracellular chloride. Front. Cell. Neurosci. **8**: 258.

Arosio, D., Ricci, F., Marchetti, L., Gualdani, R., Albertazzi, L., and Beltram, F. (2010). Simultaneous intracellular chloride and pH measurements using a GFP-based sensor. Nat. Methods **7**: 516–518.

Arosio, D., Garau, G., Ricci, F., Marchetti, L., Bizzarri, R., Nifosì, R., and Beltram, F. (2007). Spectroscopic and structural study of proton and halide ion cooperative binding to GFP. Biophys. J. **93**: 232–244.

Askwith, C., and Kaplan, J. (1997). An oxidase-permease-based iron transport system in *Schizosaccharomyces pombe* and its expression in *Saccharomyces cerevisiae*. J. Biol. Chem. **272**: 401–405.

Bassil, E., Coku, A., and Blumwald, E. (2012). Cellular ion homeostasis: Emerging roles of intracellular NHX Na^+/H^+ antiporters in plant growth and development. J. Exp. Bot. **63**: 5727–5740.

Bassil, E., Ohto, M., Esumi, T., Tajima, H., Zhu, Z., Cagnac, O., Belmonte, M., Peleg, Z., Yamaguchi, T., and Blumwald, E. (2011a). The Arabidopsis intracellular Na^+/H^+ antiporters NHX5 and NHX6 are endosome associated and necessary for plant growth and development. Plant Cell **23**: 224–239.

Bassil, E., Tajima, H., Liang, Y., Ohto, M., Ushijima, K., Nakano, R., Esumi, T., Coku, A., Belmonte, M., and Blumwald, E. (2011b). The Arabidopsis Na^+/H^+ antiporters NHX1 and NHX2 control vacuolar pH and K^+ homeostasis to regulate growth, flower development, and reproduction. Plant Cell **23**: 3482–3497.

Batoko, H., Zheng, H., Hawes, C., and Moore, I. (2000). A Rab1 GTPase is required for transport between the Endoplasmic Reticulum and Golgi apparatus and for normal Golgi movement in plants. Plant Cell **12**: 2201–2218.

Benková, E., Michniewicz, M., Sauer, M., Teichmann, T., Seifertová, D., Jürgens, G., and Friml, J. (2003). Local, efflux-dependent auxin gradients as a common module for plant organ formation. Cell **115**: 591–602.

Bergsdorf, E.-Y., Zdebik, A.A., and Jentsch, T.J. (2009). Residues important for nitrate/proton coupling in plant and mammalian CLC transporters. J. Biol. Chem. **284**: 11184–11193.

Binder, B.M., Rodríguez, F.I., and Bleecker, A.B. (2010). The copper transporter RAN1 is essential for biogenesis of ethylene receptors in Arabidopsis. J. Biol. Chem. **285**: 37263–37270.

Bolte, S., and Cordelières, F.P. (2006). A guided tour into subcellular colocalization analysis in light microscopy. J. Microsc. **224**: 213–232.

Boutté, Y., Jonsson, K., McFarlane, H.E., Johnson, E., Gendre, D., Swarup, R., Friml, J., Samuels, L., Robert, S., and Bhalerao, R.P. (2013). ECHIDNA-mediated post-Golgi trafficking of auxin carriers for differential cell elongation. Proc. Natl. Acad. Sci. USA **110**: 16259–16264.

Braun, N., Morgan, B., Dick, T., and Schwappach, B. (2010). The yeast CLC protein counteracts vesicular acidification during iron starvation. J. Cell Sci. **123**: 2342–2350.

Brüx, A., Liu, T.-Y., Krebs, M., Stierhof, Y.-D., Lohmann, J.U., Miersch, O., Wasternack, C., and Schumacher, K. (2008). Reduced V-ATPase activity in the *trans*-Golgi network causes oxylipin-dependent hypocotyl growth inhibition in Arabidopsis. Plant Cell **20**: 1088–1100.

Caño-Delgado, A., Penfield, S., Smith, C., Catley, M., and Bevan, M. (2003). Reduced cellulose synthesis invokes lignification and defense responses in *Arabidopsis thaliana*. Plant J. **34**: 351–362.

Casey, J.R., Grinstein, S., and Orlowski, J. (2010). Sensors and regulators of intracellular pH. Nat. Rev. Mol. Cell Biol. **11**: 50–61.

Chang, C., Kwok, S.F., Bleecker, A.B., and Meyerowitz, E.M. (1993). Arabidopsis ethylene-response gene ETR1: Similarity of product to two-component regulators. Science **262**: 539–544.

Clough, S.J., and Bent, A.F. (1998). Floral dip: A simplified method for Agrobacterium-mediated transformation of *Arabidopsis thaliana*. Plant J. **16**: 735–743.

Contento, A.L., and Bassham, D.C. (2012). Structure and function of endosomes in plant cells. J. Cell Sci. **125**: 3511–3518.

Craft, J., Samalova, M., Baroux, C., Townley, H., Martinez, A., Jepson, I., Tsiantis, M., and Moore, I. (2005). New pOp/LhG4 vectors for stringent glucocorticoid-dependent transgene expression in Arabidopsis. Plant J. **41**: 899–918.

Davis-Kaplan, S.R., Askwith, C.C., Bengtzen, A.C., Radisky, D., and Kaplan, J. (1998). Chloride is an allosteric effector of copper assembly for the yeast multicopper oxidase Fet3p: An unexpected role for intracellular chloride channels. Proc. Natl. Acad. Sci. USA **95**: 13641–13645.

De Angeli, A., Monachello, D., Ephritikhine, G., Frachisse, J.-M., Thomine, S., Gambale, F., and Barbier-Brygoo, H. (2009). CLC-mediated anion transport in plant cells. Philos. Trans. R. Soc. Lond. B. Biol. Sci. **364**: 195–201.

De Angeli, A., Monachello, D., Ephritikhine, G., Frachisse, J., Thomine, S., Gambale, F., and Barbier-Brygoo, H. (2006). The nitrate/proton antiporter AtCLCa mediates nitrate accumulation in plant vacuoles. Nature **442**: 939–942.

Demaurex, N., Furuya, W., D'Souza, S., Bonifacino, J.S., and Grinstein, S. (1998). Mechanism of acidification of the *trans*-Golgi network (TGN). J. Biol. Chem. **273**: 2044–2051.

Dettmer, J., Hong-Hermesdorf, A., Stierhof, Y.-D., and Schumacher, K. (2006). Vacuolar H^+-ATPase activity is required for endocytic and secretory trafficking in Arabidopsis. Plant Cell **18**: 715–730.

Dettmer, J., Schubert, D., Calvo-Weimar, O., Stierhof, Y.-D., Schmidt, R., and Schumacher, K. (2005). Essential role of the V-ATPase in male gametophyte development. Plant J. **41**: 117–124.

Di Rubbo, S., Irani, N.G., Kim, S.Y., Xu, Z.Y., Gadeyne, A., Dejonghe, W., Vanhoutte, I., Persiau, G., Eeckhout, D., Simon, S., Song, K., Kleine-Vehn, J., Friml, J., De Jaeger, G., Van Damme, D., Hwang, I., and Russinova E. (2013). The clathrin adaptor complex AP-2 mediates endocytosis of brassinosteroid insensitive1 in Arabidopsis. Plant Cell **25**: 2986–2997.

Dutzler, R., Campbell, E.B., and MacKinnon, R. (2003). Gating the selectivity filter in ClC chloride channels. Science **300**: 108–112.

Edwards, K., Johnstone, C., and Thompson, C. (1991). A simple and rapid method for the preparation of plant genomic DNA for PCR analysis. Nucleic Acids Res. **19**: 1349.

Esposito, A., Gralle, M., Dani, M.A.C., Lange, D., and Wouters, F.S. (2008). pHlameleons: A family of FRET-based protein sensors for quantitative pH imaging. Biochemistry **47**: 13115–13126.

Fendrych, M., Leung, J., and Friml, J. (2016). TIR1/AFB-Aux/IAA auxin perception mediates rapid cell wall acidification and growth of Arabidopsis hypocotyls. eLlife **5**: 1–18.

Feng, L., Campbell, E.B., Hsiung, Y., and MacKinnon, R. (2010). Structure of a eukaryotic CLC transporter defines an intermediate state in the transport cycle. Science **330**: 635–641.

Feraru, E., Paciorek, T., Feraru, M., Zwiewka, M., Groodt, R., Rycke, R., Kleine-Vehn, J., and Friml, J. (2010). The AP-3 adaptin mediates the biogenesis and function of lytic vacuoles in Arabidopsis. Plant Cell **22**: 2812–2824.

Ferjani, A., Segami, S., Horiguchi, G., Muto, Y., Maeshima, M., and Tsukaya, H. (2011). Keep an eye on PP_i: The vacuolar-type H^+-pyrophosphatase regulates postgerminative development in Arabidopsis. Plant Cell **23**: 2895–2908.

Fink, F. (2012). The V-ATPase in *Arabidopsis thaliana*: A closer look to targeting, new interaction partners and its role for ER acidification. [Master Thesis] University of Heidelberg.

Friedrichsen, D.M., Joazeiro, C.A., Li, J., Hunter, T., and Chory, J. (2000). Brassinosteroid-insensitive-1 is a ubiquitously expressed leucine-rich repeat receptor serine/threonine kinase. Plant Physiol. **123**: 1247–1256.

Gaxiola, R.A., Yuan, D.S., Klausner, R.D., and Fink, G.R. (1998). The yeast CLC chloride channel functions in cation homeostasis. Proc. Natl. Acad. Sci. USA **95**: 4046–4050.

Geldner, N., Anders, N., Wolters, H., Keicher, J., Kornberger, W., Muller, P., Delbarre, A., Ueda, T., Nakano, A., and Jürgens, G. (2003). The Arabidopsis GNOM ARF-GEF mediates endosomal recycling, auxin transport, and auxin-dependent plant growth. Cell **112**: 219–230.

Geldner, N., Hyman, D.L., Wang, X., Schumacher, K., and Chory, J. (2007). Endosomal signaling of plant steroid receptor kinase BRI1. Genes Dev. **21**: 1598–1602.

Gendre, D., Oh, J., Boutté, Y., Best, J.G., Samuels, L., Nilsson, R., Uemura, T., Marchant, A., Bennett, M.J., Grebe, M., and Bhalerao, R.P. (2011). Conserved Arabidopsis ECHIDNA protein mediates *trans*-Golgi-network trafficking and cell elongation. Proc. Natl. Acad. Sci. USA **108**: 8048–8053.

Gjetting, S., Ytting, C., Schulz, A., and Fuglsang, A. (2012). Live imaging of intra- and extracellular pH in plants using pHusion, a novel genetically encoded biosensor. J. Exp. Bot. **63**: 3207–3218.

Grefen, C., and Blatt, M.R. (2008). SNAREs - molecular governors in signalling and development. Curr. Opin. Plant Biol. **11**: 600–609.

Hechenberger, M., Schwappach, B., Fischer, W.N., Frommer, W.B., Jentsch, T.J., and Steinmeyer, K. (1996). A family of putative chloride channels from Arabidopsis and functional complementation of a yeast strain with a CLC gene disruption. J. Biol. Chem. **271**: 33632–33638.

Herdean, A., Nziengui, H., Zsiros, O., Solymosi, K., Garab, G., Lundin, B., and Spetea, C. (2016). The Arabidopsis thylakoid chloride channel AtCLCe functions in chloride homeostasis and regulation of photosynthetic electron transport. Front. Plant Sci. **7**: 115.

Himelblau, E., and Amasino, R.M. (2000). Delivering copper within plant cells. Curr. Opin. Plant Biol. **3**: 205–210.

Huotari, J., and Helenius, A. (2011). Endosome maturation. EMBO J. **30**: 3481–3500.

Huss, M., Ingenhorst, G., König, S., Gassel, M., Dröse, S., Zeeck, A., Altendorf, K., and Wieczorek, H. (2002). Concanamycin A, the specific inhibitor of V-ATPases, binds to the Vo subunit c. J. Biol. Chem. **277**: 40544–40548.

Jossier, M., Kroniewicz, L., Dalmas, F., Thiec, D., Ephritikhine, G., Thomine, S., Barbier-Brygoo, H., Vavasseur, A., Filleur, S., and Leonhardt, N. (2010). The Arabidopsis vacuolar anion transporter, AtCLCc, is involved in the regulation of stomatal movements and contributes to salt tolerance. Plant J. **64**: 563–576.

Jung, J.-Y., Kim, Y.-W., Kwak, J.M., Hwang, J.-U., Young, J., Schroeder, J.I., Hwang, I., and Lee, Y. (2002). Phosphatidylinositol 3- and 4-phosphate are required for normal stomatal movements. Plant Cell **14**: 2399–2412.

Kang, B.-H., Nielsen, E., Preuss, M.L., Mastronarde, D., and Staehelin, L.A. (2011). Electron tomography of RabA4b- and PI-4Kβ1-labeled *trans*-Golgi network compartments in Arabidopsis. Traffic **12**: 313–329.

Keinath, N.F., Waadt, R., Brugman, R., Schroeder, J.I., Grossmann, G., Schumacher, K., and Krebs, M. (2015). Live cell imaging with R-GECO1 sheds light on flg22- and chitin-induced transient $[Ca^{2+}]_{cyt}$ patterns in Arabidopsis. Mol. Plant **8**: 1188–1200.

Kim, S.-J., and Brandizzi, F. (2014). The plant secretory pathway: An essential factory for building the plant cell wall. Plant Cell Physiol. **55**: 687–693.

Krebs, M., Beyhl, D., Gorlich, E., Al-Rasheid, K.A.S., Marten, I., Stierhof, Y.-D., Hedrich, R., and Schumacher, K. (2010). Arabidopsis V-ATPase activity at the tonoplast is required for efficient nutrient storage but not for sodium accumulation. Proc. Natl. Acad. Sci. USA **107**: 3251–3256.

Kriegel, A., Andrès, Z., Medzihradszky, A., Krüger, F., Scholl, S., Delang, S., Patir-Nebioglu, M.G., Gute, G., Yang, H., Murphy, A.M., Peer, W.A., Pfeiffer, A., Krebs, M., Lohmann, J.U., and Schumacher, K. (2015). Job sharing in the endomembrane system: Vacuolar acidification requires the combined activity of V-ATPase and V-PPase. Plant Cell **27**: 3383–3396.

Kriegel, A. (2015): Vacuolar acidification relies on the combined activity of endomembrane proton pumps. [Dissertation] University of Heidelberg.

Kuner, T., and Augustine, G.J. (2000). Neurotechnique indicator for chloride : Capturing chloride transients in cultured hippocampal neurons. Neuron **27**: 447–459.

Künzl, F., Früholz, S., Fäßler, F., Li, B., and Pimpl, P. (2016). Receptor-mediated sorting of soluble vacuolar proteins ends at the *trans*-Golgi network/early endosome. Nat. Plants **2**: 16017.

Lam, S.K., Siu, C.L., Hillmer, S., Jang, S., An, G., Robinson, D.G., and Jiang, L. (2007). Rice SCAMP1 defines clathrin-coated, *trans*-Golgi-located tubular-vesicular structures as an early endosome in tobacco BY-2 cells. Plant Cell **19**: 296–319.

Lampropoulos, A., Sutikovic, Z., Wenzl, C., Maegele, I., Lohmann, J.U., and Forner, J. (2013). GreenGate - a novel, versatile, and efficient cloning system for plant transgenesis. PLoS One **8**: e83043.

Lee, Y., Bak, G., Choi, Y., Chuang, W.-I., Cho, H.-T., and Lee, Y. (2008). Roles of phosphatidylinositol 3-kinase in root hair growth. Plant Physiol. **147**: 624–635.

Liang, M., Davis, E., Gardner, D., Cai, X., and Wu, Y. (2006). Involvement of AtLAC15 in lignin synthesis in seeds and in root elongation of Arabidopsis. Planta **224**: 1185–1196.

Luo, Y. Scholl, S., Doearing, A., Zhang, Y., Irani, N.G., Di Rubbo, S., Neumetzler, L., Krishnamoorthy, P., Van Houtte, I., Mylle, E., Bischoff, V., Vernhettes, S., Winne, J., Friml, J., Stierhoff, Y.-D., Schumacher, K., Persson, S., and Russinova, J. (2015). V-ATPase activity in the TGN/EE is required for exocytosis and recycling in Arabidopsis. Nat. Plants **1**: 15094.

Lupanga, U. (2017). The role of subunit a in targeting and regulation of the V-ATPase in *Arabidopsis thaliana*. [Dissertation] University of Heidelberg.

Maeshima, M. (2001). Tonoplast transporters: Organisation and function. Annu. Rev. Plant Biol.: 469–497.

Marmagne, A., Vinauger-Douard, M., Monachello, D., Longevialle, A., Charon, C., Allot, M., Rappaport, F., Wollman, F., Barbier-Brygoo, H., and Ephritikhine, G. (2007). Two members of the Arabidopsis CLC (chloride channel) family, AtCLCe and AtCLCf, are associated with thylakoid and Golgi membranes, respectively. J. Exp. Bot. **58**: 3385–3393.

Martinière, A., Bassil, E., Jublanc, E., Alcon, C., Reguera, M., Sentenac, H., Blumwald, E., and Paris, N. (2013a). *In vivo* intracellular pH measurements in Tobacco and Arabidopsis reveal an unexpected pH gradient in the endomembrane system. Plant Cell **25**: 4028–4043.

Martinière, A., Desbrosses, G., Sentenac, H., and Paris, N. (2013b). Development and properties of genetically encoded pH sensors in plants. Front. Plant Sci. **4**: 523.

Miesenböck, G., De Angelis, D.A., and Rothman, J.E. (1998). Visualizing secretion and synaptic transmission with pH-sensitive green fluorescent proteins. Nature **394**: 192–195.

Miller, C. (2006). ClC chloride channels viewed through a transporter lens. Nature **440**: 484–489.

Mitsuda, N., Enami, K., Nakata, M., Takeyasu, K., and Y, M.H.S. (2001). Novel type *Arabidopsis thaliana* H^+-PPase is localized to the Golgi apparatus. FEBS Lett. **488**: 29–33.

Mollenhauer, H.H., Morré, D.J., and Rowe, L.D. (1990). Alteration of intracellular traffic by monensin; mechanism, specificity and relationship to toxicity. Biochim. Biophys. Acta **1031**: 225–246.

Nakanishi-Matsui, M., Sekiya, M., Nakamoto, R.K., and Futai, M. (2010). The mechanism of rotating proton pumping ATPases. Biochim. Biophys. Acta **1797**: 1343–1352.

Neubert, C., Graham, L.A., Black-Maier, E.W., Coonrod, E.M., Liu, T.-Y., Stierhof, Y.-D., Seidel, T., Stevens, T.H., and Schumacher, K. (2008). Arabidopsis has two functional orthologs of the yeast V-ATPase assembly factor Vma21p. Traffic **9**: 1618–1628.

Nguyen, C.T., Agorio, A., Jossier, M., Depre, S., and Filleur, S. (2016). Characterization of the chloride channel-like, AtCLCg, involved in chloride tolerance in *Arabidopsis thaliana*. Plant Cell Physiol. **57**: 764-775.

Niñoles, R., Rubio, L., García-Sánchez, M.J., Fernández, J. A., Bueso, E., Alejandro, S., and Serrano, R.R. (2013). A dominant-negative form of Arabidopsis AP-3 β-adaptin improves intracellular pH homeostasis. Plant J. **74**: 557–568.

Norris, S.R., Meyer, S.E., and Callis, J. (1993). The intron of *Arabidopsis thaliana* polyubiquitin genes is conserved in location and is a quantitative determinant of chimeric gene expression. Plant Mol. Biol. **21**: 895–906.

Novarino, G., Weinert, S., Rickheit, G., and Jentsch, T.J. (2010). Endosomal chloride-proton exchange rather than chloride conductance is crucial for renal endocytosis. Science **328**: 1398–1401.

Orlowski, J., and Grinstein, S. (2007). Emerging roles of alkali cation/proton exchangers in organellar homeostasis. Curr. Opin. Cell Biol. **19**: 483–492.

Park, E., Campbell, E.B., and MacKinnon, R. (2017). Structure of a CLC chloride ion channel by cryo-electron microscopy. Nature **541**: 500–505.

Park, M., Song, K., Reichardt, I., Kim, H., Mayer, U., Stierhof, Y.-D.Y.-D., Hwang, I., Jurgens, G., and Jürgens, G. (2013). Arabidopsis μ-adaptin subunit AP1M of adaptor protein complex 1 mediates late secretory and vacuolar traffic and is required for growth. Proc. Natl. Acad. Sci. USA **110**: 10318–10323.

Paroutis, P., Touret, N., and Grinstein, S. (2004). The pH of the secretory pathway: Measurement, determinants, and regulation. Physiology **19**: 207–215.

Pedrazzini, E., Komarova, N.Y., Rentsch, D., and Vitale, A. (2013). Traffic routes and signals for the tonoplast. Traffic **14**: 622–628.

Pittman, J.K. (2012). Multiple transport pathways for mediating intracellular pH homeostasis: The contribution of H+/ion exchangers. Front. Plant Sci. **3**.: 11.

Poëa-Guyon, S., Ammar, M.R., Erard, M., Amar, M., Moreau, A.W., Fossier, P., Gleize, V., Vitale, N., and Morel, N. (2013). The V-ATPase membrane domain is a sensor of granular pH that controls the exocytotic machinery. J. Cell Biol. **203**: 283–298.

Reguera, M., Bassil, E., Tajima, H., Wimmer, M., Chanoca, A., Otegui, M.S., Paris, N., and Blumwald, E. (2015). pH Regulation by NHX-type antiporters is required for receptor-mediated protein trafficking to the vacuole in Arabidopsis. Plant Cell **27**: 1200–1217.

Reyes, F.C., Buono, R., and Otegui, M.S. (2011). Plant endosomal trafficking pathways. Curr. Opin. Plant Biol. **14**: 666–673.

Robinson, D.G., Jiang, L., and Schumacher, K. (2008). The endosomal system of plants: Charting new and familiar territories. Plant Physiol. **147**: 1482–1492.

Robinson, D.G. and Pimpl, P. (2014). Clathrin and post-Golgi trafficking: A very complicated issue. Trends Plant Sci. **19**: 134–139.

Robinson, M.S. (2004). Adaptable adaptors for coated vesicles. Trends Cell Biol. **14**: 167–174.

Sanderfoot, A.A., Kovaleva, V., Bassham, D.C., and Raikhel, N. V. (2001). Interactions between syntaxins identify at least five SNARE complexes within the Golgi/prevacuolar system of the Arabidopsis cell. Mol. Biol. Cell **12**: 3733–3743.

Scheuring, D., Viotti, C., Krüger, F., Künzl, F., Sturm, S., Bubeck, J., Hillmer, S., Frigerio, L., Robinson, D.G., Pimpl, P., and Schumacher, K. (2011). Multivesicular bodies mature from the *trans*-Golgi network/early endosome in Arabidopsis. Plant Cell **23**: 3463–3481.

Schlücking, K., Edel, K.H., Köster, P., Drerup, M.M., Eckert, C., Steinhorst, L., Waadt, R., Batistic, O., Kudla, J., Batistič, O., and Kudla, J. (2013). A new β-estradiol-inducible vector set that facilitates easy construction and efficient expression of transgenes reveals CBL3-dependent cytoplasm to tonoplast translocation of CIPK5. Mol. Plant **6**: 1814–1829.

Schulte, A., Lorenzen, I., Böttcher, M., and Plieth, C. (2006). A novel fluorescent pH probe for expression in plants. Plant Methods **2**: 7.

Schumacher, K. (2014). pH in the plant endomembrane system - an import and export business. Curr. Opin. Plant Biol. **22**: 71–76.

Schumacher, K., and Krebs, M. (2010). The V-ATPase: Small cargo, large effects. Curr. Opin. Plant Biol. **13**: 724–730.

Schumacher, K., Vafeados, D., McCarthy, M., Sze, H., Wilkins, T., and Chory, J. (1999). The Arabidopsis det3 mutant reveals a central role for the vacuolar H^+-ATPase in plant growth and development. Genes Dev. **13**: 3259–3270.

Schwab, R., Ossowski, S., Riester, M., Warthmann, N., and Weigel, D. (2006). Highly specific gene silencing by artificial microRNAs in Arabidopsis. Plant Cell **18**: 1121–1133.

Segami, S., Nakanishi, Y., Sato, M.H., and Maeshima, M. (2010). Quantification, organ-specific accumulation and intracellular localization of type II H^+-pyrophosphatase in *Arabidopsis thaliana*. Plant Cell Physiol. **51**: 1350–1360.

Shaner, N.C., Steinbach, P.A., and Tsien, R.Y. (2005). A guide to choosing fluorescent proteins. Nat. Methods **2**: 905–909.

Shen, J., Zeng, Y., Zhuang, X., Sun, L., Yao, X., Pimpl, P., and Jiang, L. (2013). Organelle pH in the Arabidopsis endomembrane system. Mol. Plant **6**: 1419–1437.

Singh, M.K., Krüger, F., Beckmann, H., Brumm, S., Vermeer, J.E.M., Munnik, T., Mayer, U., Stierhof, Y.-D., Grefen, C., Schumacher, K., and Jürgens, G. (2014). Protein delivery to vacuole requires SAND protein-dependent Rab GTPase conversion for MVB-vacuole fusion. Curr. Biol. **24**: 1383–1389.

Sonawane, N.D., Thiagarajah, J.R., and Verkman, A.S. (2002). Chloride concentration in endosomes measured using a ratioable fluorescent C^{l-} indicator: Evidence for chloride accumulation during acidification. J. Biol. Chem. **277**: 5506–5513.

Staal, M., De Cnodder, T., Simon, D., Vandenbussche, F., Van der Straeten, D., Verbelen, J.-P., Elzenga, T., and Vissenberg, K. (2011). Apoplastic alkalinization is instrumental for the inhibition of cell elongation in the Arabidopsis root by the ethylene precursor 1-aminocyclopropane-1-carboxylic acid. Plant Physiol. **155**: 2049–2055.

Staehelin, L. A., and Moore, I. (1995). The plant Golgi apparatus: Structure, functional organization and trafficking mechanisms. Annu. Rev. Plant Physiol. Plant Mol. Biol. **46**: 261–288.

Stauber, T., and Jentsch, T.J. (2013). Chloride in vesicular trafficking and function. Annu. Rev. Physiol. **75**: 453–477.

Strompen, G., Dettmer, J., Stierhof, Y.-D., Schumacher, K., Jürgens, G., and Mayer, U. (2005). Arabidopsis vacuolar H^+-ATPase subunit E isoform 1 is required for Golgi organization and vacuole function in embryogenesis. Plant J. **41**: 125–132.

Swanson, S., and Jones, R. (1996). Gibberellic acid induces vacuolar acidification in Barley aleurone. Plant Cell **8**: 2211–2221.

Takano, J., Noguchi, K., Yasumori, M., Kobayashi, M., Gajdos, Z., Miwa, K., Hayashi, H., Yoneyama, T., and Fujiwara, T. (2002). Arabidopsis boron transporter for xylem loading. Nature **420**: 337–340.

Teh, O.-K., Shimono, Y., Shirakawa, M., Fukao, Y., Tamura, K., Shimada, T., and Hara-Nishimura, I. (2013). The AP-1 μ adaptin is required for KNOLLE localization at the cell plate to mediate cytokinesis in Arabidopsis. Plant Cell Physiol. **54**: 838–847.

Tse, Y.C., Bo., B., Hillmer, S., Zhao, M., Lo, S.W., Robinson, D.G., Jiang, L. (2004). Identification of multivesicular bodies as prevacuolar compartments in *Nicotiana tabacum* BY-2 Cells. Plant Cell **16**: 672–693.

Uemura, T. (2016). Physiological roles of plant post-Golgi transport pathways in membrane trafficking. Plant Cell Physiol. **57**: 2013–2019.

Viotti, C., Bubek, J., Stierhof, Y.-D., Krebs, M., Langhans, M., van der Berg, W., van Dongen, W., Richter, S., Geldner, N., Takano, J., Jürgens, G., de Vries, S.C., Robinson, D.G., and Karin Schumacher (2010). Endocytic and secretory traffic in Arabidopsis merge in the *trans*-Golgi network/early endosome, an independent and highly dynamic organelle. Plant Cell **22**: 1344–1357.

von der Fecht-Bartenbach, J., Bogner, M., Dynowski, M., and Ludewig, U. (2010). CLC-b-mediated $NO3^-/H^+$ exchange across the tonoplast of Arabidopsis vacuoles. Plant Cell Physiol. **51**: 960–968.

von der Fecht-Bartenbach, J., Bogner, M., Krebs, M., Stierhof, Y.-D., Schumacher, K., and Ludewig, U. (2007). Function of the anion transporter AtCLC-d in the *trans*-Golgi network. Plant J. **50**: 466–474.

Wang, J.-G., Li, S., Zhao, X.-Y., Zhou, L.-Z., Huang, G.-Q., Feng, C., and Zhang, Y. (2013). HAPLESS13, the Arabidopsis μ1 adaptin, is essential for protein sorting at the *trans*-Golgi network/early endosome. Plant Physiol. **162**: 1897–1910.

Wang, X., Cai, Y., Wang, H., Zeng, Y., Zhuang, X., Li, B., and Jiang, L. (2014). *Trans*-Golgi network-located AP1 gamma adaptins mediate dileucine motif-directed vacuolar targeting in Arabidopsis. Plant Cell: **22** 4009-4033.

Wege, S., Jossier, M., Filleur, S., Thomine, S., Barbier-Brygoo, H., Gambale, F., and De Angeli, A. (2010). The proline 160 in the selectivity filter of the Arabidopsis NO_3^-/H^+ exchanger AtCLCa is essential for nitrate accumulation in planta. Plant J. **63**: 861–869.

Weigel, D., Ahn, J.H., Blázquez, M.A., Borewitz, J.O., Christensen, S.K., Fankhauser, C., Ferrándiz, C., Kardailsky, I., Malancharuvil, E.J., Neff, M.M., Nguyen, J.T., Sato, S., Wang, Z.-Y., Xia, Y., Dixon, R.A., Harrison, M.J., Lamb, C.J., Yanofsky, M.F., and Chory, J. (2000). Activation tagging in Arabidopsis. Plant Physiol. **122**: 1003–1013.

Weinert, S., Jabs, S., Supanchart, C., Schweizer, M., Gimber, N., Richter, M., Rademann, J., Stauber, T., Kornak, U., and Jentsch, T.J. (2010). Lysosomal pathology and osteopetrosis upon loss of H^+-driven lysosomal Cl^- accumulation. Science **328**: 1401–1403.

Woeste, K.E., and Kieber, J.J. (2000). A strong loss-of-function mutation in RAN1 results in constitutive activation of the ethylene response pathway as well as a rosette-lethal phenotype. Plant Cell **12**: 443–455.

Wolf, S., and Greiner, S. (2012). Growth control by cell wall pectins. Protoplasma **249 Suppl 2**: S169-175.

Wolfenstetter, S., Wirsching, P., Dotzauer, D., Schneider, S., and Sauer, N. (2012). Routes to the tonoplast: The sorting of tonoplast transporters in Arabidopsis mesophyll protoplasts. Plant Cell **24**: 215–232.

Woollard, A.A.D., and Moore, I. (2008). The functions of Rab GTPases in plant membrane traffic. Curr. Opin. Plant Biol. **11**: 610–619.

Wu, M.M., Grabe, M., Adams, S., Tsien, R.Y., Moore, H.-P.H., and Machen, T.E. (2001). Mechanisms of pH regulation in the regulated secretory pathway. J. Biol. Chem. **276**: 33027–33035.

Yang, X., Xu, P., Xiao, Y., Xiong, X., and Xu, T. (2006). Domain requirement for the membrane trafficking and targeting of Syntaxin 1A. J. Biol. Chem. **281**: 15457–15463.

Yoo, S., Cho, Y., and Sheen, J. (2007). Arabidopsis mesophyll protoplasts: A versatile cell system for transient gene expression analysis. Nat. Protoc. **2**: 1565–1572.

Yoshida, S. (1994). Low temperature-induced cytoplasmic acidosis in cultured mung bean (*Vigna radiata* [L.] Wilczek) cells. Plant Physiol. **104**: 1131–1138.

Zhang, G.F., and Staehelin, L. A. (1992). Functional compartmentation of the Golgi apparatus of plant cells : Immunocytochemical analysis of high-pressure frozen- and freeze-substituted sycamore maple suspension culture cells. Plant Physiol. **99**: 1070–1083.

Zhang, Y., Nikolovski, N., Sorieul, M., Vellosillo, T., McFarlane, H.E., Dupree, R., Kesten, C., Schneider, R., Driemeier, C., Lathe, R., Lampugnani, E., Yu, X., Ivakov, A., Doblin, M.S., Mortimer, J.C., Brown, S.P., Persson, S., and Dupree, P. (2016). Golgi-localized STELLO proteins regulate the assembly and trafficking of cellulose synthase complexes in Arabidopsis. Nat. Commun. **7**: 11656.

Zhao, J., Benlekbir, S., and Rubinstein, J.L. (2015). Electron cryomicroscopy observation of rotational states in a eukaryotic V-ATPase. Nature **521**: 241–245.

Zheng, H., Camacho, L., Wee, E., Batoko, H., Legen, J., Leaver, C.J., Malhó, R., Hussey, P.J., and Moore, I. (2005). A Rab-E GTPase mutant acts downstream of the Rab-D subclass in biosynthetic membrane traffic to the plasma membrane in tobacco leaf epidermis. Plant Cell **17**: 2020–2036.

Zifarelli, G., and Pusch, M. (2010). CLC transport proteins in plants. FEBS Lett. **584**: 2122–2127.

Acknowledgment

In this last section, I want to say 'thank you' to all the people who supported me during the time in the lab. The successful completion of this thesis would not have been possible without the support and promotion on various fields.

First and foremost, I would like to express my gratitude to Prof. Dr. Karin Schumacher for the opportunity to successfully complete my PhD thesis in her workgroup and for all the helpful discussions and ideas to the project. I also appreciated the many opportunities to visit other workgroups and to present on international conferences.

I also want to thank Prof. Dr. Alexis Maizel for agreeing to be the second appraiser of this thesis on very short notice.

I would like to thank Prof. Dr. Jan Lohmann for his guidance and ideas during the TAC -meetings throughout the years.

I thank Prof. Dr. Marius Lemberg and Dr. Sebastian Wolf for taking part in the thesis committee and for helpful advices for my various projects.

I would like to thank my colleagues especially Dr. Melanie Krebs for support, ideas, solutions to a lot of problems and critical reading of this manuscript. Also I want to thank Rachel Röhrich for reading and her helpful comments to this thesis. Thanks to Fabian Fink and Falco Krüger for advice, support and the great time. Of course, I also want to acknowledge Görkem Patir Nebioglu, Jana Askani, Dr. Rainer Waadt, Simon Delang, Dr. Upendo Lupanga and Dr. Zaida Andrès for being terrific colleagues.

I thank Dr. Stefan Hillmer and Stefanie Gold for their assistance with sample preparation, sectioning and help with the electron microscope.

For the technical assistance and for keeping the plant facility and the lab in excellent shape, I want to thank Beate Schöfer and Barbara Jesenowski.

Also I want to thank Ines Steins for the administrative work and taking care of everything.

I want to thank again my parents, brothers and their families for support and encouragement.

Also thanks to Clara, not only for proofreading my thesis.